E. TEKE

ATILIM UNIVERSITY 2021

DESIGN AND ANALYSIS OF THE CHASSIS OF NEW GENERATION ELECTRIC OVEN COOKER IN VIEW OF MANUFACTURING AND FLUID FLOW

THE GRADUATE SCHOOL OF NATURAL APPLIED SCIENCES
OF
ATILIM UNIVERSITY

ETHEM TEKE

A MASTER OF SCIENCES THESIS
IN
THE DEPARTMENT OF MECHANICAL ENGINEERING

MAY 2021

DESIGN AND ANALYSIS OF THE CHASSIS OF NEW GENERATION ELECTRIC OVEN COOKER IN VIEW OF MANUFACTURING AND FLUID FLOW

THE GRADUATE SCHOOL OF NATURAL APPLIED SCIENCES
OF
ATILIM UNIVERSITY

ETHEM TEKE

A MASTER OF SCIENCES THESIS
IN
THE DEPARTMENT OF MECHANICAL ENGINEERING

MAY 2021

Approval of the Graduate School of Natural and Applied Sciences, Atilim University.

_____

Prof. Dr. Ender Keskinkılıç
Director

I certify that this thesis satisfies all the requirements as a thesis for the degree of Master of Science in Mechanical Engineering Department, Atilim University.

_____

Prof. Dr. Sadık Engin Kılıç
Head of Department

This is to certify that we have read the thesis DESIGN AND ANALYSIS OF THE CHASSIS OF NEW GENERATION ELECTRIC OVEN COOKER IN VIEW OF MANUFACTURING AND FLUID FLOW submitted by ETHEM TEKE¸ and that in our opinion it is fully adequate, in scope and quality, as a thesis for the degree of Master of Science.

_____	_____
Prof. Dr. Hasan U. Akay Co- Supervisor	Asst. Prof. Dr. Besim Baranoğlu Supervisor

Examining Committee Members:

Prof. Dr. Hasan U. Akay
Automotive Engineering, Atilim University _____

Assoc. Prof. Dr. Barbaros Çetin
Mechanical Engineering, Bilkent University _____

Assoc. Prof. Dr. Özgür Aslan
Mechanical Engineering, Atilim University _____

Asst. Prof. Dr. Besim Baranoğlu
Manufacturing Engineering, Atilim University _____

Asst. Prof. Dr. Eren Billur
Automotive Engineering, Atilim University _____

Date: May 19, 2021

I declare and guarantee that all date, knowledge and information in this document has been obtained, processed and presented in accordance with academic rules and ethical conduct. Based on these rules and conduct, I have fully cited and referenced all material and results that are not original to this work.

Name, Last Name: ETHEM TEKE

Signature:

ABSTRACT

DESIGN AND ANALYSIS OF THE CHASSIS OF NEW GENERATION ELECTRIC OVEN COOKER IN VIEW OF MANUFACTURING AND FLUID FLOW

TEKE, Ethem
M.Sc., Mechanical Engineering Department
Supervisor: Asst. Prof. Dr. Besim BARANOĞLU
Co-Supervisor: Prof. Dr. Hasan U. AKAY

May 2021, 82 pages

Built-in ovens are cooking devices that are embedded in kitchen furniture. Built-in ovens placed in a standardized furniture size are subject to international safety standards. During the cooking process, the cooking cavity, which can reach up to 250˚C, heats the regions around it. The temperature of the kitchen furniture and the temperature of the areas that the user can contact such as the oven door are very important parameters. There are cooling groups placed on the oven cooking cavity to keep this temperature at a certain level. Cooling group keeps the temperature under control by sucking hot air from the cooking cavity, the space between the oven and the furniture and between the glass doors of the cooking cavity. The industrial competition forces manufacturers to design with larger cooking cavities. The growth of the cooking cavity narrows the place of cooling groups and requires smaller and more efficient cooling group designs. The air leaving the cooling group must be homogeneous in order to cool the glass doors of the cooking cavity uniformly.

In order to optimize the flow and homogeneity of air outlets, the geometry of the sheet metal cover in which the cooling group fan is located should be optimized. In this study the formability of the sheet metal cover containing the impeller is verified with the Finite Element Method (FEM) simulations and then the homogeneity and the volumetric flow rate of the air flows are calculated with Computational Fluid Dynamics (CFD) are applied. The results yielded into a better design for a press-formable sheet metal cover with adequate flow characteristics.

Keywords: Sheet metal forming, Finite Element Method (FEM), Computational Fluid Dynamics (CFD), Simulation, Validation

ÖZ

YENİ NESİL FIRINLARIN ŞASİ VE HAVA AKIŞ AÇISINDAN ANALİZİ

TEKE, Ethem
Yüksek Lisans, Makine Mühendisliği Bölümü
Danışman: Dr. Öğr. Üyesi Besim BARANOĞLU
Eş Danışman: Prof. Dr. Hasan U. AKAY

Mayıs 2021, 82 Sayfa

Ankastre fırınlar bir mutfak mobilyasının içine gömülmüş pişirici cihazlardır. Standartlaşmış bir mobilya ölçüsü içine yerleştirilen ankastre fırınlar uluslararası güvenlik standartlarına tabiidir. Pişirme işlemi sırasında 250 ˚C sıcaklığa kadar ulaşabilen pişirme bölmesi etrafındaki bölgeleri ısıtır. Mutfak mobilyasının sıcaklığı ve kullanıcının temas edebileceği fırın kapağı gibi bölgelerin sıcaklıkları oldukça önemli parametrelerdir. Bu sıcaklığı belli seviyelerde tutmak için fırın pişirme bölmelerinin üzerine yerleştirilen soğutma grupları bulunur. Soğutma grupları pişirme bölmesinden, fırın ile mobilya arasındaki boşluktan ve pişirme bölmesinin cam kapakları arasından sıcak havayı çekerek sıcaklığı kontrol altında tutar. Endüstriyel rekabet ortamı, üreticilerin daha büyük pişirme bölmesi olan ürünler tasarlamaya zorlamaktadır. Pişirme bölmesinin büyümesi soğutma gruplarının yerine daraltmakta ve daha küçük ve verimli soğutma grubu tasarımlarını gerektirmektedir.

Pişirme bölmesinin cam kapaklarını soğutmak için soğutma grubundan çıkan havanın homojen olması gerekir. Debi ve homojen hava çıkışlarını ayarlamak için soğutma grubu fanının içinde bulunduğu metal sacın geometrisinin optimize edilmesi gerekmektedir.

Bu optimizasyonun yapılması için fanın içinde bulunduğu sac metal levhanın şekillendirilebilirliği Sonlu Elemanlar Yöntemi ile doğrulanıp daha sonra Hesaplamalı Akışkanlar Dinamiği (HAD) ile hava akışlarının homojenitesi ve debisi hesaplanmalıdır. Sonuçlar, yeterli ve düzgün bir hava akış özelliklerine sahip ve şekillendirilebilir bir sac metal kapak tasarımına yol açmıştır.

Anahtar Kelimeler: Sac Şekillendirme, Sonlu elemanlar yöntemi, Hesaplamalı Akışkanlar Dinamiği (HAD), Simulasyon, Validasyon

To Münevver TEKE

1939- ∞

ACKNOWLEDGEMENT

Firstly, I would like to express my sincere gratitude to my supervisor Asst. Prof. Dr. Besim BARANOĞLU for his guidance, encouragement, and support throughout my entire postgraduate program.

I would like to thank to my Co-supervisor Prof. Dr. Hasan U. AKAY for his guidance and his referrals throughout the research.

I would like to thank colleagues of Metal Forming Center of Excellence where I performed all of the experiments. Also, a special thanks to Türkay MURATOĞLU for his technical supports.

I would like to express my sincere appreciations to Erdem EROĞLU, Ogün DÜZGÜN, M. Barış GÖÇER, Dr. Musa DEMİRBAŞ, Yahya AKKUŞ and Research & Development Department of Femaş Metal Co. Inc., especially for supporting and giving me a chance of being part of this project.

I would like to thank, Şeyma ÖKMEN who always stood behind me and always supported me.

TABLE OF CONTENTS

ABSTRACT iii
ÖZ v
DEDICATION vii
ACKNOWLEDGEMENT viii
TABLE OF CONTENTS ix
CHAPTER 1 1
INTRODUCTION 1
1.1. General Information About Built- In Ovens 1
1.2. Importance of Ventilation Systems at Built-In Ovens 3
1.3. Design Limitations 4
1.4. Aim and Scope of the Thesis 5
CHAPTER 2 6
LITERATURE REVIEW 6
2.1. General Information About Sheet Metal Forming 6
2.2. Formability Limit Diagram (FLD) 8
2.3. General Information on Centrifugal Pumps 10
2.4. Computational Fluid Dynamics Method 15
2.4.1 The Reynold Averaged Navier- Stokes Equations 16
2.4.2 k-ε Turbulence Model 17
2.4.3. Rotating Frame of Reference 19
CHAPTER 3 20
EXPERIMENTAL PROCEDURE 20
3.1. Material 20
3.2. Tensile Test 20
3.3. Forming Limit Curve Tests 23
3.3.1. Nakajima Test Results 29
CHAPTER 4 31
SIMULATIONS 31
4.1. Description of the First Model 31
4.1.1 Sheet Metal Forming Analysis of the First Model 32

4.1.2. Forming Analysis Results of the First Model 34
4.1.2.1. Effective Plastic Strain 34
4.1.2.2. Forming Limit Parameters 35
4.1.3. CFD Analysis of the First Model 36
4.1.3.1 The Model and the Boundary Conditions 36
4.1.4. CFD Results of the First Model 38
4.2. Description of the Second Model 41
4.2.1. Sheet Forming Analysis of the Second Model 42
4.2.2. Forming Analysis Results of the Second Model 44
4.2.2.1. Effective Plastic Strain 44
4.2.2.2. Forming Limit Parameters 45
4.3. Description of the Third Model 46
4.3.1 Sheet Forming Analysis of The Third Model 47
4.3.2. Forming Analysis Results of the Third Model 50
4.3.2.1. Effective Plastic Strain 50
4.3.2.2. Forming Limit Curve 51
4.3.3. CFD Analysis of the Third Model 53
4.3.3.1. Model Description and Boundary Conditions 53
4.3.4. CFD Results of the Third Model 55
4.4 Design of the Motor Connection Part 58
4.4.1 The First Motor Connection Design CFD Simulation 58
4.4.1.1 Description of the First Motor Part Design 58
4.4.1.2 The First Motor Connection Design CFD Result 59
4.4.2 Description of the Second Motor Connection Part Design 60
4.4.2.1 Second Motor Connection Design CFD Simulation 60
4.4.1.2 The Second Motor Connection Design CFD Result 61
4.5. Chimney Location 62
CHAPTER 5 63
VALIDATIONS 63
5.1. Air Flow Validation 63
5.1.1. Flow Speed Validation by Calibrated Anemometer 66
5.2. Sheet Metal Forming Simulation Validation 67
5.2.1 GOM-ARGUS Optical Forming Analysis 67

5.3. Validation of Simulations 70
5.3.1. CFD Simulation Validation 70
5.3.2 Forming Simulation Validation 72
CHAPTER 6 75
RESULTS AND DISCUSSIONS 75
6.1 Results Obtained From Sheet Metal Forming Simulation 75
6.2 Results Obtained From Computational Fluid Dynamics Simulations 77
REFERENCES 80

LIST OF TABLES

TABLES

Table 3.1 Chemical composition of DX54D-Z (courtesy from Erdemir Metal Inc). 20
Table 3.2 Properties of zwick z300e [16] 20
Table 3.3 FLC results from punched dome tests..... 29
Table 4.1 The forming simulation parameters of first design sheet metal cover……33
Table 4.2 Details of CFD Simulations of the first designed sheet metal cover on Autodesk CFD..... 38
Table 4.3 The forming simulation parameters of the second design sheet metal cover. 44
Table 4.4 The stroke and forming difference at the second design between blank with hole and without hole. 46
Table 4.5 The forming simulation parameters of the third design sheet metal cover 50
Table 4.6 The stroke and forming difference at the third design between blank with hole and without hole 52
Table 4.7 Details of CFD Simulations of the third designed sheet metal cover on Autodesk CFD..... 55
Table 6.1 The radius changing effect on forming……...76
Table 6.2 The radius and hole effect on forming……..……..77

LIST OF FIGURE

FIGURES

Figure 1.1 William Hadaway ‘’Electric Heater’’ Patent US705668A [2] 2

Figure 1.2 Flow orientation can shown around the Built-in oven (courtesy of Femas Metal Inc)…...……...3

Figure 1.3 Design limitations of cooling group at built-in ovens (courtesy of Femas Metal Inc)…….……..……...4

Figure 1.4 Space limitations of the impeller of the cooling group (courtesy of Femas Metal Inc)……...……...5

Figure 2.1 The progressive dies’ step by step forming stages (reprinted from [7])……..…….……..7

Figure 2.2 Schematic illustration of sheet metal forming (reprinted from [3]) 8

Figure 2.3 Failure of the Nakajima test specimen while forming by hydraulic bulge test (reprinted from [9])..... 9

Figure 2.4 In obtaining the graph, the minor strain is plotted on the X axis and the major strain is plotted on the Y axis (reprinted from [9])..... 9

Figure 2.5 A axial flow turbo-machine [12] 10

Figure 2. 6 A mixed-flow turbo-machine [12]..... 11

Figure 2.7 A radial flow turbo-machine [12]..... 12

Figure 2.8 Radial flow turbo-machine blade types 13

Figure 2.9 Comparison of net head and brake horse power performance curves of the three main types of centrifugal pumps [12]……..14

Figure 2.10 Technical drawins of the impeller which is used in this thesis (courtesy of Femaş, Kayseri-Turkey)..... 14

Figure 2.11 The flow behavior at built-in ovens..... 15

Figure 2.12 Rotating frame of reference schematic illustration..... 19

Figure 3.1 The universal tensile test machine Zwick Z300E at the Metal Forming Center of Excellence……...21

Figure 3.2 DX54D-Z Zinc coated (galvanized) deep drawing sheet metal flow curve at r_0 direction tensile test 23

Figure 3.3 Zwick-Roell BUP600 Formability Limit Curve Test Device at Metal Forming Center of Excellence 24
Figure 3.4 The exploded view of 3D Modeled Nakajima specimen forming simulation by Simufact forming 24
Figure 3.5 Step by step Nakajima specimen forming simulation by Simufact Forming software. 25
Figure 3.6 The 2D technical drawing of 7 different Nakajima specimens 26
Figure 3.7 Detailed FLD explanation of experimental FLC for DC04-EK, FLC courtesy from the Metal Forming of Excellence 27
Figure 3.8 Schematic illustration of FLC calculation with Aramis system, (image courtesy of GOM). 28
Figure 3.9 Recorded image by CCD cameras and strain distributions obtained from GOM Aramis image (courtesy Metal Forming Center of Excellence) 29
Figure 3.10 Formability limit curve of DX54D-Z zinc coated (galvanized sheet metal). 30
Figure 4.1 Isometric and exploded view of first designed cooling group……32
Figure 4.2 The top and front view of the die set for forming first design cooling group's sheet metal cover. 32
Figure 4.3 Mesh structure of the first designed cooling group sheet metal cover. 33
Figure 4.4 Top and İsometric view of effective plastic strain distribution visualization from end of the first model sheet metal cover forming. 34
Figure 4.5 Top and isometric forming limit distribution visualization from end of the first design sheet metal cover forming. 35
Figure 4.6 Top view of the first designed cooling group 36
Figure 4.7 Boundary conditions of first designed cooling group 37
Figure 4.8 Mesh structure of the first model cooling group for CFD simulation. 38
Figure 4.9 The cross section of the volume which calculated on Autodesk CFD. 38
Figure 4.10 Top view of velocity path lines of the first designed cooling group 39
Figure 4.11 Isometric view of velocity path lines of the first designed cooling group 39
Figure 4.12 Bottom view of velocity path lines of the first designed cooling group….40
Figure 4.13 Velocity separation on the first model's outlet slots. 41
Figure 4.14 Isometric and exploded view of the second designed cooling group 41

Figure 4.15 The top, front and isometric views of the die set for forming the first design cooling group's sheet metal cover..... 42
Figure 4.16 Mesh structures of the second designed cooling group sheet metal cover without a hole (a) and with a hole (b). 43
Figure 4.17 Top and isometric view of effective plastic strain distributions visualization from the end of the second model sheet metal cover forming. 44
Figure 4.18 Top and isometric forming limit distributions visualization from end of the second model sheet metal cover forming. 46
Figure 4.19 The expanded radius from 16 mm to 28 mm. 47
Figure 4.20 İsometric and exploded view of third designed cooling group 47
Figure 4.21 The top, front and isometric views of the die set for forming of the third design cooling group's sheet metal cover. 48
Figure 4.22 Mesh structures of the third designed cooling group sheet metal cover without hole (a) and with hole (b). 49
Figure 4.23 Top and isometric view of effective plastic strain distributions visualization from end of the third model sheet metal cover forming. 50
Figure 4.24 Top and isometric forming limit distributions visualization from end of the second model sheet metal cover forming. 51
Figure 4.25 The 70 mm diameter hole expansion and material flow lines on the third design sheet metal cover. 52
Figure 4.26 The location of the expanded hole and motor connection cut out locations 52
Figure 4.27 Top view of the third designed cooling group 53
Figure 4.28 Boundary conditions of the third designed cooling group 54
Figure 4.29 Mesh structure of the third model cooling group to CFD simulation 55
Figure 4.30 The cross section of the volume which calculated on Autodesk CFD. .. 55
Figure 4.31 Top view of velocity path lines of the third designed cooling group 56
Figure 4.32 İsometric view of velocity path lines of third designed cooling group .. 56
Figure 4.33 Bottom view of velocity path lines of third designed cooling group 57
Figure 4.34 Velocity separation on third model's outlet slots. 57
Figure 4.35 The first type of motor connection part. 58
Figure 4.36 The cross section of the first type of motor connection part. 59
Figure 4.37 The flow lines around the first design impeller inlet area. 59

Figure 4.38 The side view of the flow lines around the cooling group 60
Figure 4.39 The second type of motor connection part. 60
Figure 4.40 The cross section of second type of motor connection part..... 61
Figure 4.41 The flow lines around the second design impeller inlet area..... 61
Figure 4.42 İllustration of horizontal air flow bending to the inlet area. 62
Figure 4.43 The static pressure map under the impeller 62
Figure 5.1 The impeller and motor connection PA12 prototype……64
Figure 5.2 The sheet metal cover which produced by real molds..... 64
Figure 5.3 The cooling group bottom flat sheet metal cut by computer aided laser.. 65
Figure 5.4 The completed the third designed prototype 65
Figure 5.5 Testo 405i hot wire anemometer 66
Figure 5.6 The sheet metal cover which is located on scale bars and some coded markers..... 67
Figure 5.7 Using photogrammetry methods, the images are imaginally assembled to produce the object. 68
Figure 5.8 Erased corner grids because of die friction..... 69
Figure 5.9 The section location of the holes where the measurements were made ... 70
Figure 5.10 Holes on the sheet metal impeller cover to immerse the anemometer probe. 71
Figure 5.11 Measured and simulated flow velocity comparison of Section A-B 71
Figure 5.12 The comparison between Gom-Argus digital image correlation system and simulation Plastic Strain results. 72
Figure 5.13 The comparison between Gom-Argus digital image correlation system and simulation thickness reduction results. 73
Figure 5.14 The comparison between Gom-Argus digital image correlation system and simulation FLD results..... 74
Figure 6.1 The forming limit parameters of 16 mm corner radius cooling group sheet metal cover (a) and 28 mm radius cooling group sheet metal cover (b)……76
Figure 6.2 The forming limit parameters of 16 mm corner radius cooling group sheet metal cover with 70 mm hole (a) and 28 mm corner radius cooling group sheet metal cover with 70 mm hole (b). 77
Figure 6.3 The location of the enlarged hole and motor connection cut out locations. 77

Figure 6.4 The bottom view of the first designed cooling group CFD results..... 78
Figure 6.5 The bottom view of the third designed cooling group CFD results 78

CHAPTER 1

INTRODUCTION

1.1. General Information About Built- In Ovens

Humankind has been living on the Earth for 300.000 years. In the early period they were consuming their foods without cooking. After the discovery of fire, humankind realized that cooked foods are more delicious and easier to eat. With the agricultural revolution, humanity has built cities and they have continued cooking by wood fire. While open fires have been used for thousands of years, this cooking method was a challenge. This case has changed with the development of the oven. The first official oven in recorded history was built in 1490. It was in France and made using brick and tile. Although there may have been other ovens before this date, the French oven is the first one recorded [1].

The modern electric powered oven was patented in 1896 by William Hadaway as it can be seen in Figure 1.1 [2]. Although electric ovens were invented in 1896, they were not widely used in houses until the practical application of electricity improved in the late 1920s. At the present time, electrical ovens work with the same principles, like the early electrical ovens, except the built-in ovens.

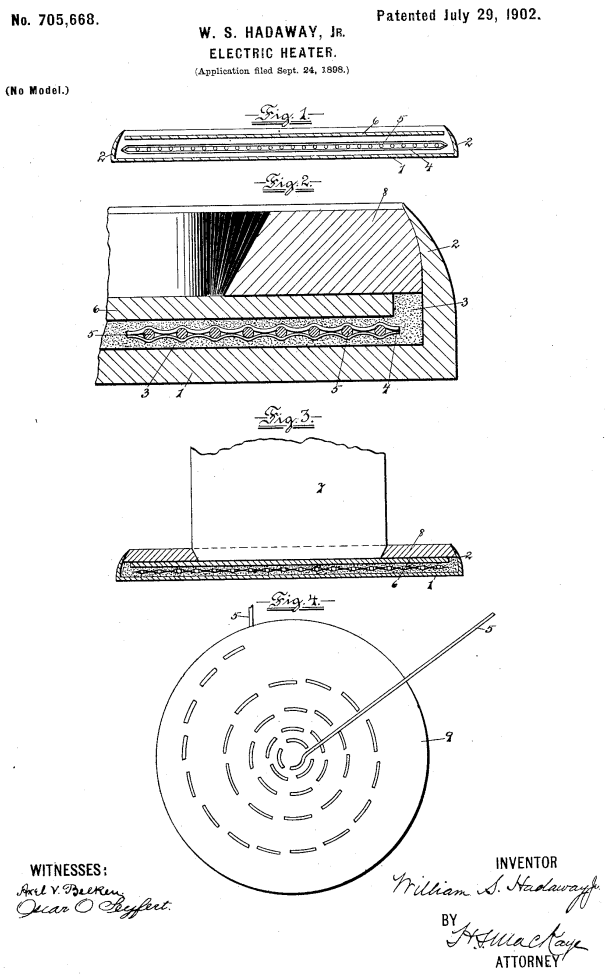

Figure 1.1 William Hadaway "Electric Heater'' Patent US705668A [2]

Space constraints and aesthetic concerns in public housing have led people to use built-in ovens. Built-in ovens are placed in a furniture space. For this reason, the furniture temperature is important for safety. To prevent any dangerous temperature increase, built-in ovens use insulation materials like glass fiber around the cooking cavity. Nevertheless, only insulation is not enough to prevent temperature increases on the furniture cavity. For this reason, a good and properly oriented ventilation is necessary.

1.2. Importance of the Ventilation Systems at Built-In Ovens

While built-in oven cooking cavities reach 400 °C, the furniture surface should be less than a maximum 60 °C to prevent furniture damage. Another important issue is front glass temperature since if the door glasses are not well cooled, they can do harm to the users. The requirement for the door glasses is not only the cooling of the glass, but also the homogeneity of temperature is very important. This requires the flow which passes through the upper side of the glasses to be homogeneous. This way the Venturi effect on the top side of door glass layers also helps for cooling of the glass door, leading to a better homogeneity of the temperature.

With developed technology, built-in ovens get smarter day by day. In order to produce smarter and efficient built-in ovens, producers have been using complex electronic circuits so that ventilation and cooling of electronics becomes another important case at built-in ovens.

In the course of the baking process, steam and other gases are generated in the cooking chamber. Evaporated water can be beneficial for cooking, but harmful gases are carcinogenic and must be removed from the cooking chamber. Therefore, steam and other harmful gas levels inside the baking chamber should be controlled by a chimney which is located at the top of the baking chamber. The cooking cavity chimney should be directly connected to the ventilation system because of the sucked air, which can contain high-level carcinogenic gases and moistened air should exhaust outside to prevent electronic corrosion or oxidation. Figure 1.2 shows path lines of flows.

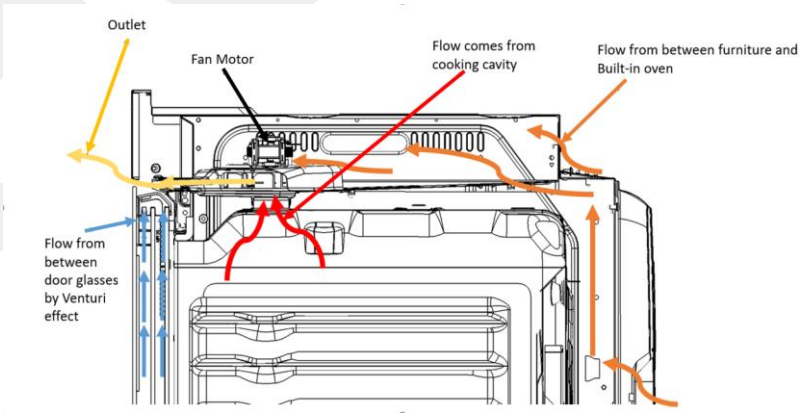

Figure 1.2 Flow orientation can shown around the Built-in oven (courtesy of Femas Metal Inc.)

1.3. Design Limitations

The real challenge of cooling at built-in ovens is limited sizes to accommodate cooling groups due to the standard sizes available in kitchen furniture. As seen in Figure 1.3 the furniture cut out sizes are generally 593x560x593mm. Cooling groups are generally placed on top of the cooking cavity and for this reason height is the major design parameter, so that height limitation of 593 mm is significantly important.

Competition in the market forces manufacturers to design bigger cooking cavities therefore the space to accommodate the cooling group is narrowing. The cooling group sizes depend on space so the designed cooling group's outlet should be a maximum of 11 mm x 433 mm as it is seen in Figure 1.3. It is seen in Figure 1.4; the impellers cannot be bigger than Ø96 mm and cannot be higher than 16 mm.

Another important parameter is the rotational speed of the impeller, which is generally measured in revolutions per minute (rpm). In this study, the distance between the top wall and the top of the motor has to be a minimum of 10 mm to avoid any touch of the motor shaft, for this reason, motor sizes are limited. The motor torque output depends on the stator lamination height of the motor, for this reason, the motor can reach a maximum of 1200 rpm with the designed impeller. The space limitations of the cooling group can be seen in Figure 1.4.

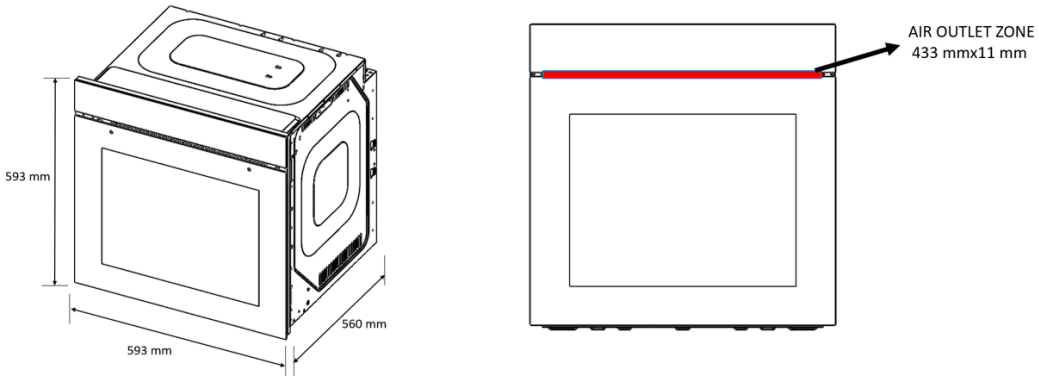

Figure 1.3 Design limitations of cooling group at built-in ovens (courtesy of Femas Metal Inc.)

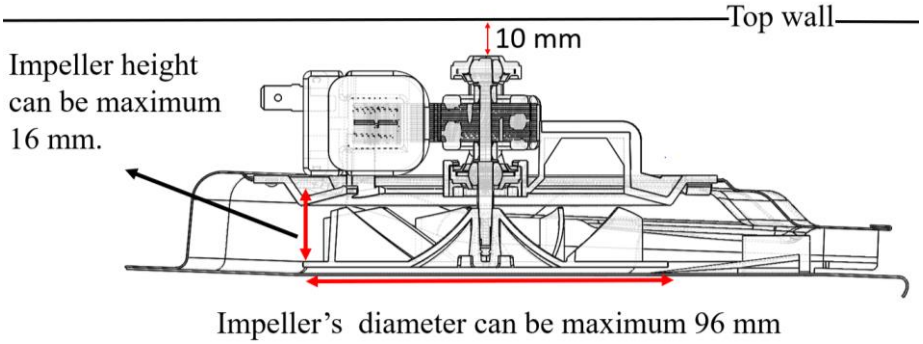

Figure 1.4 Space limitations of the impeller of the cooling group (courtesy of Femas Metal Inc.)

The determination of the form of the ventilation system is one of the most critical design points. Since sheet metal is used in the design, it greatly limits the design because of the formability limits of the sheet metal.

1.4. Aim and Scope of the Thesis

In this study, to determine the shape of the impeller coverage, which is called sheet metal cover, finite element simulations were performed to find an improved geometry to obtain homogeneous airflow outlet with SIMUFACT FORMING 15.0 that is licensed to the Atılım University. The sheet metal forming simulations performed 3D with Hexahedral mesh structure type. To validate the simulation which has done by SIMUFACT FORMING, AUTOFORM R8 has been used by an external company (Halil TUTU) which is licensed to that company. Alongside with the sheet metal forming analyses, Computational Fluid Dynamics (CFD) simulations are performed with the licensed student edition of AUTODESK CFD 2020 software, to obtain the flow characteristic of the design geometry. In the CFD analyses, The Reynolds Averaged Navier Stokes mathematical model is used. The simulation yielded better flow characteristics with a press-formable sheet cover geometry.

CHAPTER 2

LITERATURE REVIEW

2.1. General Information About Sheet Metal Forming

Sheet metal forming is a process that is widely used for producing high-volume components in the automotive, aircraft, and home appliance industries. In the process of sheet metal forming, the pieces of sheet metal are formed to its geometry rather than wasting any materials. The applied method causes a force that stresses the material to reshape. This in turn gives the possibility to bend or stretch the sheet metal to a variety of different forms [3].

The sheet metal forming includes basic processes, like bending (DIN 8586), stretching (DIN 8586) and more complex process like spinning, roll forming and deep drawing (DIN 8584). All of these processes are classified under the DIN standards with DIN 8582: manufacturing processes [4],[5] forming classification, subdivision, terms and definitions. The noted standards above refer to subsections of this standard. Every type of process has its properties and limitations, including the tools geometry. The design process becomes even more complex when the geometry of the product is complex and/or it is needed to combine various processes or steps to produce the part. The complex parts can be produced by progressive process steps as it is demonstrated in Figure 2.1. The main driving force for the development of numerical tools like sheet metal forming simulations, enabling the virtual tryout of sheet metal forming components, is the industry, in particular the automotive, aerospace, and home appliances industries, due to the enormous number of components involved in built-in ovens, and complex production [6].

Figure 2.1 The progressive dies' step by step forming stages. (Reprinted from [7])

The outer sheet metals are generally the parts with the largest surface area, and their production includes the most complex operations which includes at least one deep drawing process. In the deep drawing process the sheet metal is plastically deformed into the desired form by the action of forming tools, which generally consist of a punch, a die and a blank holder. The blank is located between the dies, and it forces the flow into the die surface by the displacement of the punch. The flow of the sheet metal is generally controlled with a blank holder that imposes a constant force on the flange region of the sheet metal [8]. A schematic illustration of sheet metal forming is given in Figure 2.2.

Therefore, even for a simple forming process and supposing that the mechanical attitude of the sheet metal is known, there are different design variables to consider, that are connected to the blank and punch geometry and with the process control, like the blank holder force. The finite element method (FEM) based conjectural simulation of sheet metal forming components permits a feasible process design to material behaviors that are mutually defined using physics-based constitutive models.

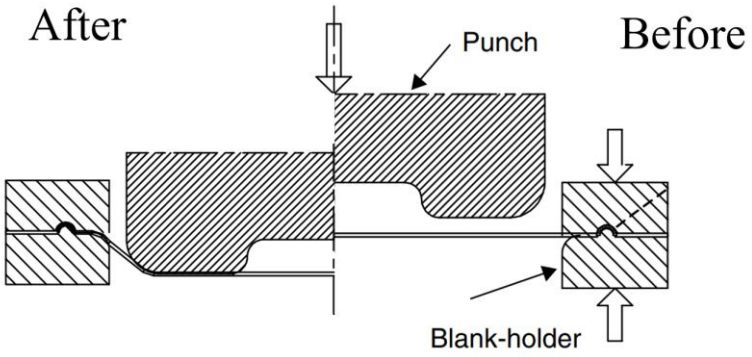

Figure 2.2 Schematic illustration of sheet metal forming (reprinted from [3])

2.2. Forming Limit Curve (FLC)

A forming limit curve is used in sheet metal forming for predicting forming behavior of sheet metals [9]. The diagram attempts to provide a graphical description of material failure under the application of different strain paths. Among other methods proposed for the evaluation of the FLC, the Nakajima tests is one of the most widely used and is practically a punched dome test. A press with a dome punch deforms seven different Nakajima test geometries until failure (Figure 2.3). While this process is happening, the strains are recorded and/or evaluated. This can be done by measuring the punch height or the dome height and evaluating the strain assuming a perfect spherical dome. But a more modern approach is to use stereoscopic cameras to measure the displacements which are then converted a major and minor strains. In obtaining the graph, the minor strain is plotted on the horizontal axis and the major strain is plotted on the vertical axis (Figure 2.4). In Nakajima test, seven different geometries give seven different minor and major strain paths on the graph [3][10]. Along with the bi-axial test specimen, these contribute to 8 points on the graph.

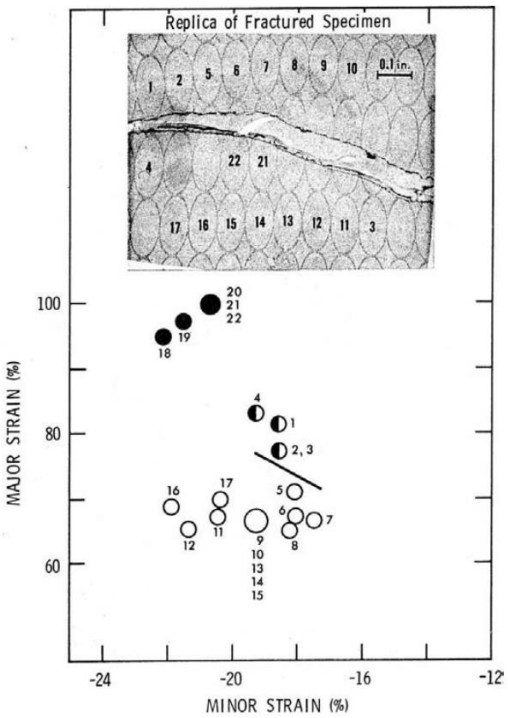

Figure 2.3 Failure of the Nakajima test specimen while forming by hydraulic bulge test (reprinted from [9])

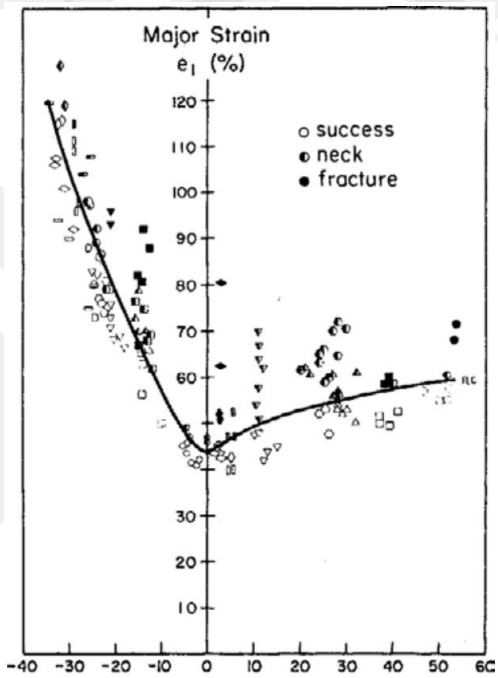

Figure 2.4 In obtaining the graph, the minor strain is plotted on the X axis and the major strain is plotted on the Y axis (reprinted from [9])

Using the FLC, the material's forming limit can be predicted. The upper side of the graph represents possible sheet metal failure, the lower side represents a safe zone. In this way, designers can compare the results of sheet metal simulations and the formability curve then can optimize design parameters. The details of FLD method of measurement can be seen in Chapter 3.

2.3. General Information on Centrifugal Pumps

Centrifugal pumps are members of the turbo-machinery family. The systems that transfer the torque of a rotating blade to the fluid are called turbo-machines. The most accepted classification of turbo-machines is the choice according to the flow line or through-flow. There are three types of turbo-machines classified depending on the flow line are the axial flow, radial flow and mixed flow turbo machines [11],[12].

The first type of turbo-machine is the axial flow turbo-machine in Figure 2.5. In which, the working fluid essentially moves horizontally to the axis of the rotation of the shaft. Axial flow turbo-machines have a wide range of usage areas which are ventilation systems, jet-powered aircrafts, ventilation, etc [13].

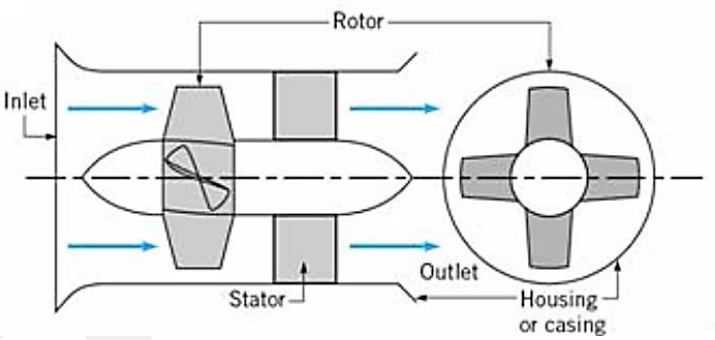

Figure 2.5 Axial flow turbo-machine [12]

The second type is the mixed-flow turbo-machines shown in Figure 2.6 where the impeller geometry is in between the design concepts of radial and the axial turbo-machines.

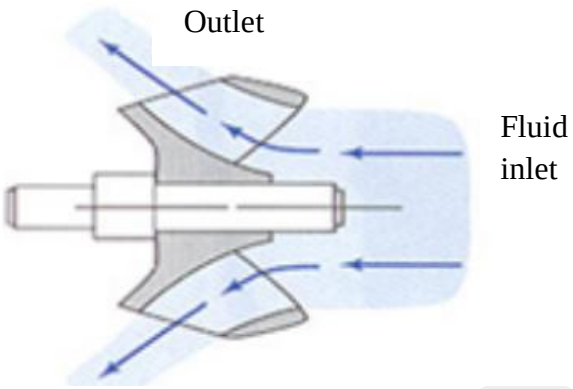

Figure 2.6 A mixed-flow turbo-machine [12]

The last type of turbo-machines is the radial flow turbo-machines can be seen in Figure 2.7. In which, the working fluid moves essentially in a direction vertical to the axis of rotation of the blades. Radial turbo-machines are mainly used in pumping, ventilation, or cooling systems. The essential preferred position of the radial turbo-machines is their high capacity and their ability to provide high-pressure differences in small dimensions [12].

Their disadvantage is that, for a given pressure difference, they cannot supply as high volumetric flow rates as an axial turbo-machine can. The radial turbo-machines have radial fans, that are encased flow turbo-machines, that transfer the flow in a radial direction and are widely used because they reach high pressure ratios in a short axial distance compared to the axial fans [12].

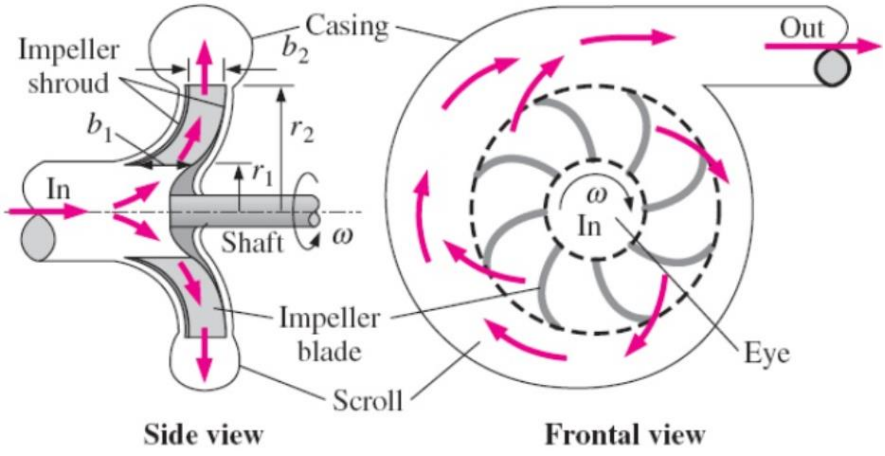

Figure 2.7 A radial flow turbo-machine [12]

The rotor is one of the most important parts of the radial fans. Because of flow rate, pressure, and other parameters depend on the rotor's geometry and rpm. There are three types of pumps that warrant discussion, based on impeller blade geometry as shown in Figure 2.8.

Centrifugal pumps with forward-inclined blades shown in Figure 2.8.a produce a pressure rise that is nearly constant, albeit lower than that of radial or backward-inclined blades generally have more blades, but the blades are smaller. Forward-inclined centrifugal pumps generally have a lower maximum efficiency than do straight-bladed pumps. Radial and backward-inclined centrifugal pumps are preferred for applications where one needs to provide volume flow rate and pressure rise within a narrow range of values [14],[15].

Centrifugal pumps with radial blades shown in Figure 2.8.b have the simplest geometry and produce the largest pressure rise of the three for a wide range of volume flow rates, but the pressure rise decreases rapidly after the point of maximum efficiency.

Centrifugal pumps with backward-inclined blades shown in Figure 2.8.c are the most widely recognized. These yield the highest efficiency of the three because fluid flows into and out of the blade passages with a minimal measure of turning [12].

In this thesis, backward inclined blade shape is preferred because centrifugal pumps with backward-inclined blades are the most widely recognized. The three main types of centrifugal pumps are those with a comparison of net head and brake horsepower performance curves in Figure 2.9. As it can be seen from the figure, the backward inclined pumps have the highest net head when compared with the brake horsepower.

In this thesis, backward inclined blade shape impeller is preferred, seen in Figure 2.10 because the centrifugal pumps with backward-inclined blades are much more energy efficient than the radial blade fans and so, for high power applications may be a suitable alternative to the lower cost radial bladed fan [16]. These yield the highest efficiency of the three, because fluid flows into and out of the blade passages with minimal measure of turning [17].

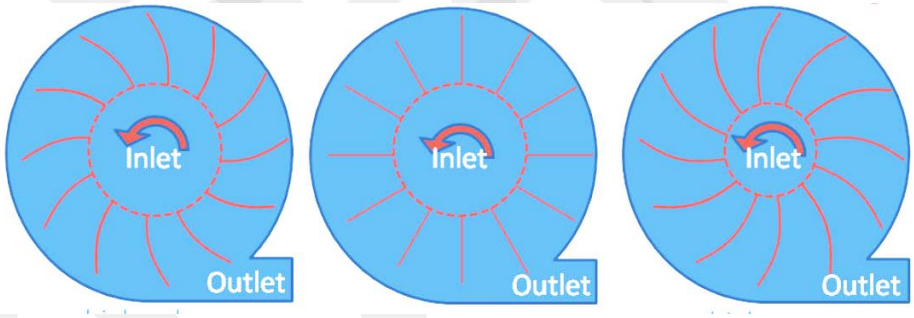

(a) Forward inclined blades (b) Radial inclined blades (c) Backward inclined blades

Figure 2.8 Radial flow turbo-machine blade types [12]

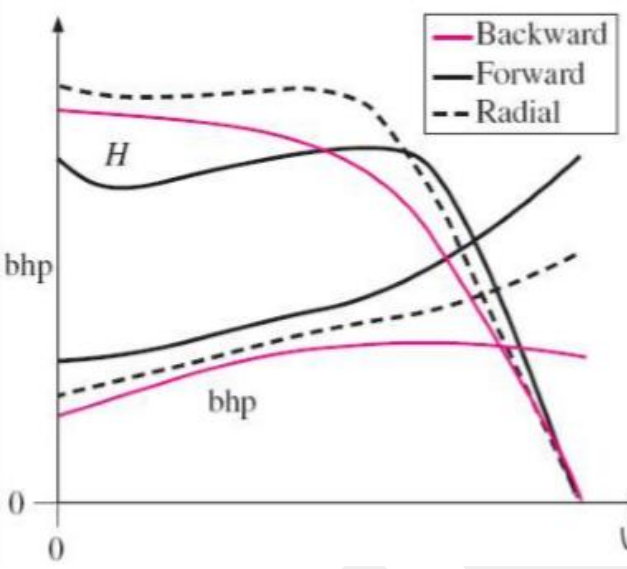

Figure 2.9 Comparison of net head and brake horse power performance curves of the three main types of centrifugal pumps [12]

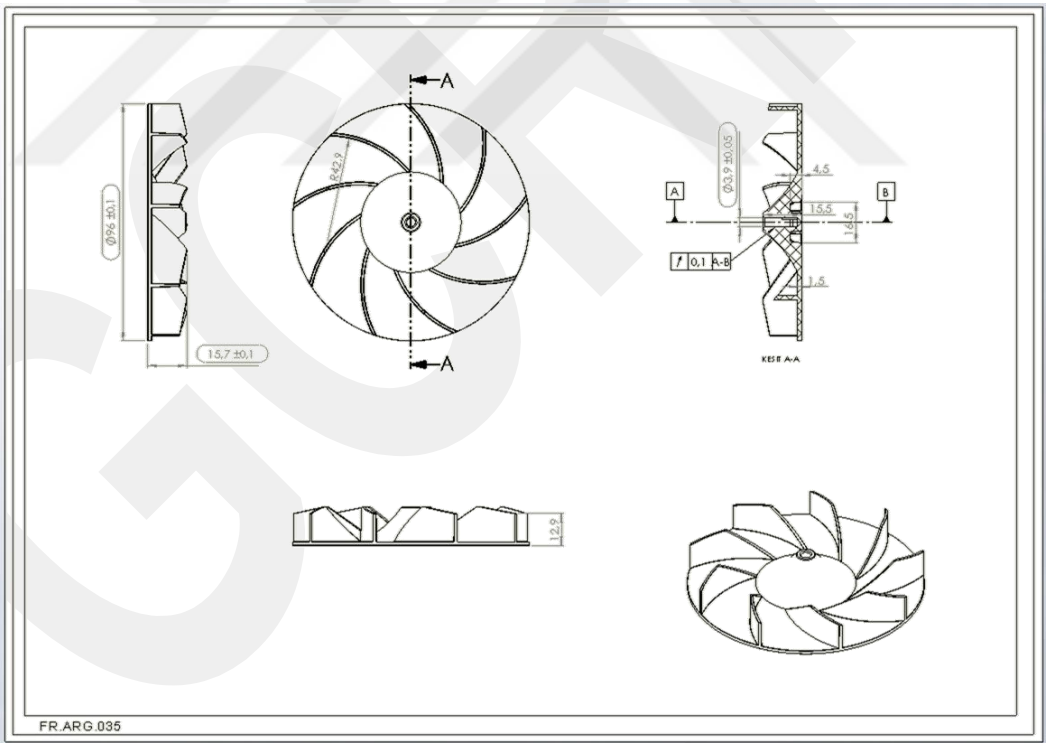

Figure 2.10 Technical drawings of the impeller, which is used in this thesis (courtesy of Femaş, Kayseri-Turkey)

According to the benchmark products that have been studied, 300 L/min flow rate is sufficient for cooling. The most important parameters are the homogeneity of air and the volumetric flow rate, because as it is shown in Figure 2.9, the blown air to the outside also helps to go out the heated air between the door glass layers.

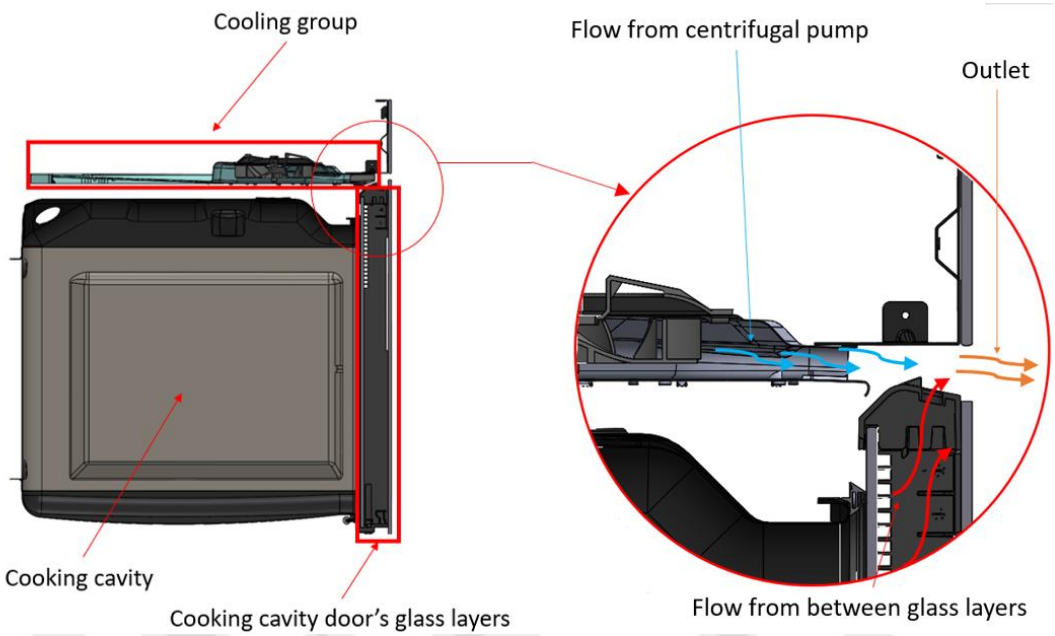

Figure 2.11 The flow behavior in built-in oven

2.4. Computational Fluid Dynamics Method

To model and simulate air the flow behavior, CFD simulations have been performed by Autodesk CFD. Simulations are modeled by The Reynold Averaged Navier Stokes (RANS) equations with k-epsilon turbulence model. The rotating frame of reference model used between the fluid domain and impeller.

.

2.4.1 The Reynold Averaged Navier- Stokes Equations

The Reynolds-averaged Navier–Stokes equations (RANS) are time-averaged equations of motion for fluid flow. The concept behind the equations is the Reynolds decomposition, by an instantaneous quantity is decomposed into its time-averaged and fluctuating quantities, an idea first proposed by Osborne Reynolds [15]. The RANS equations are mainly used to describe turbulent flows. These equations can be used with approximations that depend on the knowledge of the specification of flow turbulence to give approximate time-averaged solutions to the Navier–Stokes equations [19]. For the velocity components (2.1);

$$u_i = \bar{u}_i + u_i' \tag{2.1}$$

Where $\bar{u}_i$ and u_i' are the mean and fluctuating components (i=1,2,3). Additionally, for pressure and other scalar quantities (2.2):

$$\emptyset = \overline{\emptyset} + \emptyset' \tag{2.2}$$

Where Ø denotes a scalar such as pressure, energy, or species concentration.

Substituting expressions of this form for the flow variables in the instantaneous continuity and momentum equations and taking a time average (and dropping the overbar on the mean velocity $\bar{u}$) yields the ensemble-averaged momentum equations [20]. They can be written in Cartesian tensor form as in Eqs. 2.3 and 2.4.

$$\frac{\partial \rho}{\partial t} + \frac{\partial}{\partial x_i}(\rho u_i) = 0 \tag{2.3}$$

$$\frac{\partial}{\partial t}(\rho u_i) + \frac{\partial}{\partial x_i}\left(\rho u_i u_j\right) = -\frac{\partial p}{\partial x_i} + \frac{\partial}{\partial x_j}\left[\mu\left(\frac{\partial u_i}{\partial x_j} + \frac{\partial u_j}{\partial x_i} - \frac{2}{3}\,\delta_{ij}\frac{\partial u_l}{\partial x_l}\right)\right] +$$

$$\frac{\partial}{\partial x_j}\left(-\rho\,\overline{u_i' u_j'}\right) \tag{2.4}$$

Equation 2.3 and Equation 2.4 are called Reynolds-averaged Navier-Stokes (RANS) equations. They have the same general form as the instantaneous Navier-Stokes's equations, with the velocities and other solution variables now representing ensemble-averaged (or time-averaged) values. Additional terms now appear that represent the effects of turbulence [20]. These Reynolds stresses, $-\rho \underline{u_i' u_j'}$, must be modeled in order to close Equation 2.4.

For variable-density flows, Equation 2.3 and Equation 2.4 can be interpreted as Favre-averaged Navier-Stokes's equations [21], with the velocities representing mass-averaged values. As such, Equation 2.3 and Equation 2.4 can be applied to variable-density flows [20].

2.4.2 k-ε Turbulence Model

The k-ε model is one of the most accepted turbulence models, although it doesn't perform well in cases of large adverse pressure gradients [22]. It is a two-equation model, that includes two extra transport equations to represent the turbulent features of the flow. This allows a two-equation model to account for time effects like convection and diffusion of turbulent energy.

The first transported variant is turbulent kinetic energy, k. The second transported variant in this situation is the turbulent dissipation, ε. It is the variable that determines the scale of the turbulence, although the first variable, k, determines the energy in the turbulence.

The exact k-ε equations contain many unknown and unmeasurable terms. For a much more practical approach, the standard k-ε turbulence model is used which is based on our best understanding of the relevant processes, in this way minimizing unknowns and presenting a set of equations which can be applied to a large number of turbulent applications [23].

For turbulent kinetic energy k;

$$\frac{\partial(\rho k)}{\partial t}+\frac{\partial(\rho k u_i)}{\partial x_i}=\frac{\partial}{\partial x_j}\left[\frac{\mu_t}{\sigma_k}\frac{\partial k}{\partial x_j}\right]+2\mu_t E_{ij}E_{ij}-\rho\varepsilon \tag{2.5}$$

For dissipation ε;

$$\frac{\partial(\rho\varepsilon)}{\partial t}+\frac{\partial(\rho\varepsilon u_i)}{\partial x_i}=\frac{\partial}{\partial x_i}\left[\frac{\mu_t}{\sigma_\varepsilon}\frac{\partial\varepsilon}{\partial x_j}\right]+C_{1\varepsilon}\frac{\varepsilon}{k}2\mu_t E_{ij}E_{ij}-C_{2\varepsilon}\rho\frac{\varepsilon^2}{k} \tag{2.6}$$

Where;

u_i, symbolizes velocity component in the corresponding direction, E_{ij}, symbolizes component of the rate of deformation, μ_t, symbolizes eddy viscosity:

$$\mu_t=\rho C_\mu\frac{k^2}{\varepsilon} \tag{2.7}$$

The equations also consist of some adjustable constants σ_k, σ_ε, $C_{1\varepsilon}$ and $C_{2\varepsilon}$. The values of these constants have been obtained by numerous iterations of data fitting of experiments for a wide range of turbulent flows. These are as follows [23],[24]:

$C_\mu = 0.09$ $\sigma_k = 1.00$ $\sigma_\varepsilon = 1.30$ $C_{1\varepsilon} = 1.44$ $C_{2\varepsilon} = 1.92$

2.4.3. Rotating Frame of Reference

The Autodesk CFD rotating machinery capability simulates rotating devices using a locally rotating frame of reference. This zone completely surrounds a rotating object, and is called the rotating region.

Areas in the model that are not rotating are analyzed in a static frame of reference. These zones are called static regions. Fluid in a static zone can move, but the volume itself does not (Figure 2.12).

To use of rotating frame of reference;

- Each rotating part must be completely immersed in a rotating zone. Rotating zones rotate using their own relative rotating frame of reference.
- The mesh that is generated in a rotating zone will physically rotate with the parts that are immersed.
- Immersed parts can be modeled as voids or as solid within the rotating zone. Solid parts in a rotating zone rotate at the same speed as the rotating zone.
- The interface between a rotating and a static zone is called the periphery zone. Within the periphery zone, the outer element faces of the rotating zone slide along with the neighboring element faces of the static zone [25].

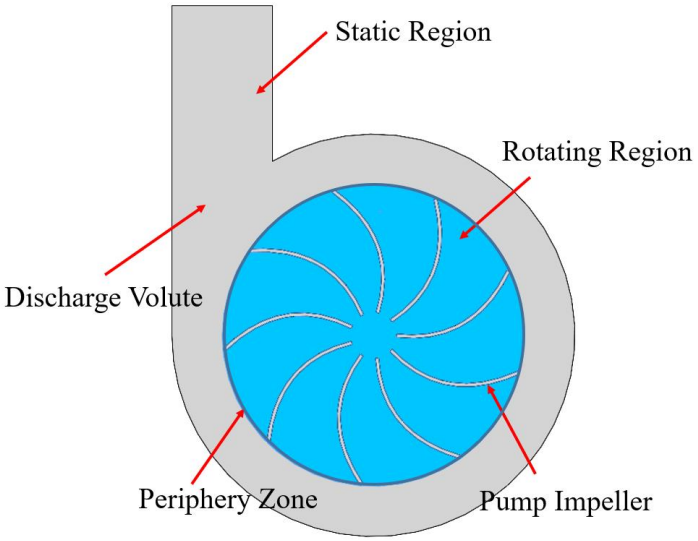

Figure 2.12 Rotating frame of reference schematic illustration

CHAPTER 3

EXPERIMENTAL PROCEDURE

3.1. Material

In this study, cold-rolled DX-54D-Z zinc-coated (galvanized) deep drawing quality steel was used. It corresponds to DIN EN 10346 in Europe. This metal is classified as low carbon steel that is suitable for deep drawing and resistant to oxidation. Chemical composition of DX54 is given in Table 3.1.

Table 3.1 Chemical composition of DX54D-Z (courtesy of Erdemir Metal Inc.)

Element	**C**	**Si**	**Mn**	**P**	**S**	**Ti**
Weight %	0,12	0,50	0,60	0,10	0,045	0,30

3.2. Tensile Test

The tensile test is well-known and the most common method for understanding material characteristics [26]. Zwick z300e is a universal tensile test device is shown in Figure 3.1. Also, the properties of the Zwick tensile test device are given in Table 3.2.

Table 3.2 Properties of Zwick Roell Z300e [25]

Fmax (kN)	300
Motor	AC Servo motor with concentrated windings
Force Measurement	Class 0.5 from 1% of Fmax / Class 1 from 0.2 % of Fmax, as per EN ISO 7500-1, ASTM E4, JIS B 7721
Electrical Supply	400 V +/- 10 %
Power Consumption	6.5 kVA

Figure 3.1 The universal tensile test machine Zwick Z300E at the Metal Forming Center of Excellence

In this thesis, tensile tests were performed to find a stress- strain diagram for use in simulations. Also, the anisotropic behavior of the 0.4 mm thickness DX54D-Z was measured by testing with specimens produced in 0˚, 45˚and 90˚ with respect to the rolling direction.

O.4 mm thickness of the DX54D-Z galvanized deep drawing quality sheet metal was shaped by a laser cut. 3 sets of samples produced in 3 different rolling directions. Zwick/Roell Z300E test machine has constant crosshead speed. Displacement of the crossheads per time v_c is found as [27];

$$v_c = L_c \dot{e}_{L_C} \tag{3.1}$$

L_c symbolizes parallel length of tensile test specimens (120 mm);

$\dot{e}_{L_C}$ symbolizes estimated strain rate over the parallel length.

Tests were performed by Zwick/Roell Z300E Universal Testing Machine with constant strain rate of 0.00025 1/s before yielding and 0.0067 1/s after yielding at room temperature (in accordance with ISO 6892-1) [28] at Atılım University Metal Forming Center of Excellence.

Using equation 3.1:

The displacement of the crossheads per time v_c before yielding is

v_c =0.00025.120 =0,03 mm/s

The displacement of the crossheads per time v_c after yielding;

v_c =0.0067.120 = 0.804 mm/s.

Samples of the DX 54D-Z galvanized deep drawing quality sheet metal are repeated 3 times for 3 directions, adhering to rolling directions. Test outputs are analyzed by Zwick testXpert software. The results interpolated by Hollomon equation. The r_0 direction tensile test result can be seen in Figure 3.2.

The extrapolation is with Hollomon equation,

$$\sigma = C\varepsilon^n \tag{3.2}$$

where, from the experiments $C \cong 197.40$ and $\varepsilon \cong 1.97$. In the three experiments performed, average value of the strain at failure is 21% (engineering strain) and the ultimate tensile (engineering) stress is $R_m \cong 303.32MPa$.

The anisotropy is modeled through the parameters r_0 , r_{45} and r_{90} are given as:

r_0 =2.00, r_{45} =1.97 and r_{90} =2.62.

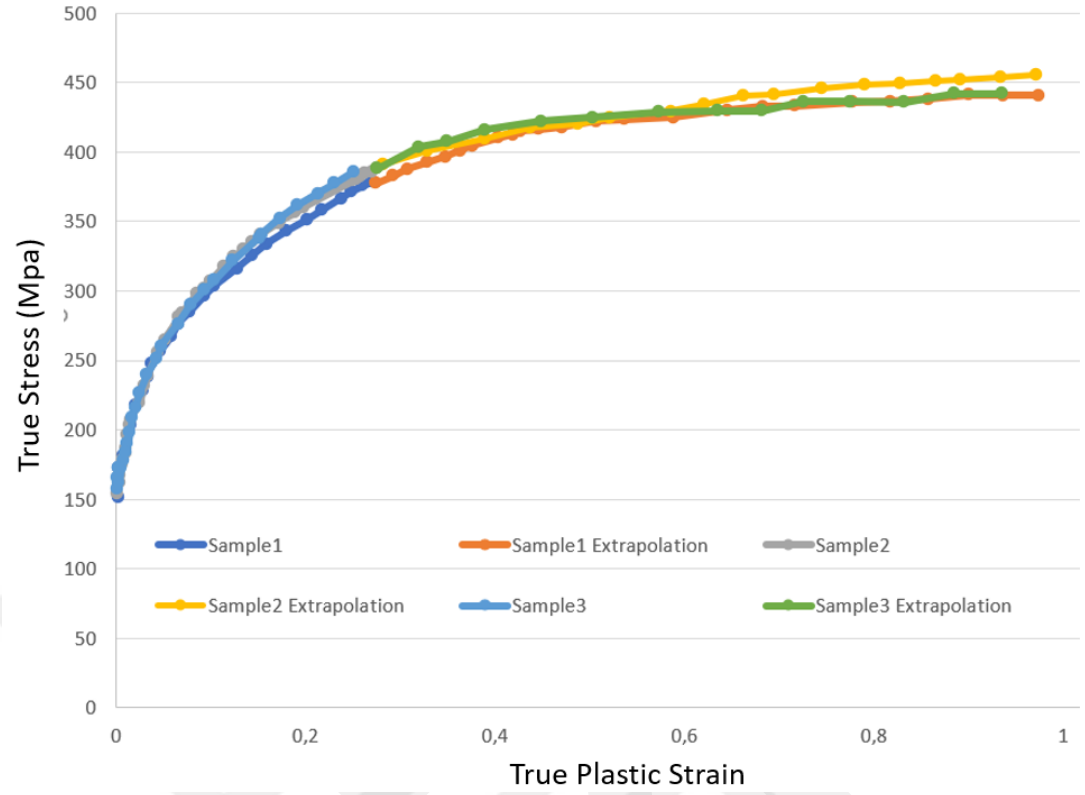

Figure 3.2 DX54D-Z Zinc coated (galvanized) deep drawing sheet metal flow curve at r_0 direction tensile test

3.3. Forming Limit Curve Tests

The forming limit curve (FLC) is used in sheet metal forming for predicting forming behavior of sheet metal. To foresee a safe and healthy deep drawing process, forming limit curve is a very important guide. The curve attempts to provide a graphical description of material failure tests, such as a punched dome test. A press with dome punch as it seems at Figure 3.3 deform eight different test geometries until tears occur. Detailed die sets can be seen in Figure 3.4. The forming limit curve gives a failure table of the material as to major and minor strains.

Figure 3.3 Zwick-Roell BUP600 Forming Limit Curve Test Device at Metal Forming Center of Excellence

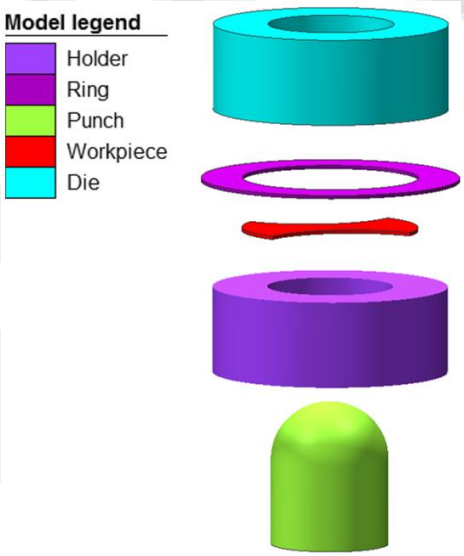

Figure 3.4 The exploded view of 3D Modeled Nakajima specimen forming simulation by Simufact forming

The FLC indicates the connection between these principal strain paths diffusion or localized necking during a plane-stress condition for various strain paths. FLC of sheet metal is sometimes obtained based on localized necking. For a sheet metal underneath stretching load, diffuse necking may be ascertained initially, so localized necking is seen. Among the localized necking method, the sheet thickness decreases sharply as illustrated in Figure 3.5, then the sheet failure happens. Hence, the major and minor strains once localized necking initiates are represented as forming limit strains of the sheet metal [29].

The Nakajima test is a well-known technique to see the forming limit of sheet metal materials. The method relies on the principle of deforming sheet metal blanks of various geometries using a hemispherical punch till fracture happens. Step by step Nakajima specimen forming simulation is shown in Figure 3.5.

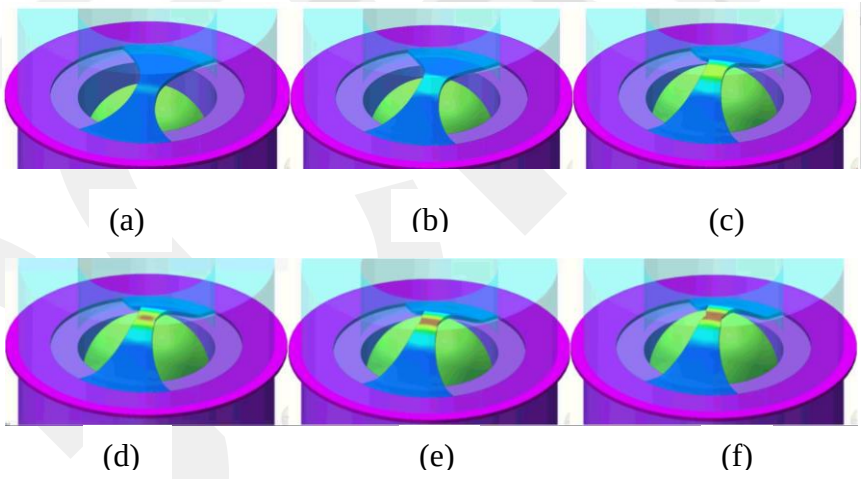

Figure 3.5 Step by step Nakajima specimen forming simulation by Simufact Forming software

In this thesis, eight different geometries were used. Every specimen has different radiuses, between 35 to 85 mm as seem in Figure 3.6. Specimen radiuses change according to various deep drawing cases occurring on the sheet metal. In this way, various strains were collected [30].

The first specimen which has an 85 mm radius simulates the simple tensile test. The last specimen which has no radius simulates biaxial strain rates. Other specimens gave different major and minor strain rates then a formability limit curve can be drawn. A detailed forming limit diagram explanation can be seen in Figure 3.7.

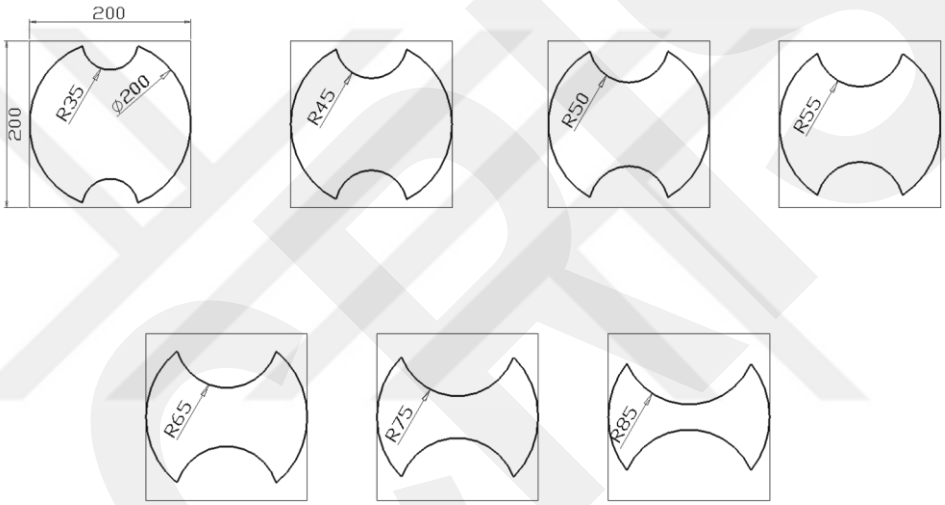

Figure 3.6 The 2D technical drawing of 7 different Nakajima specimens

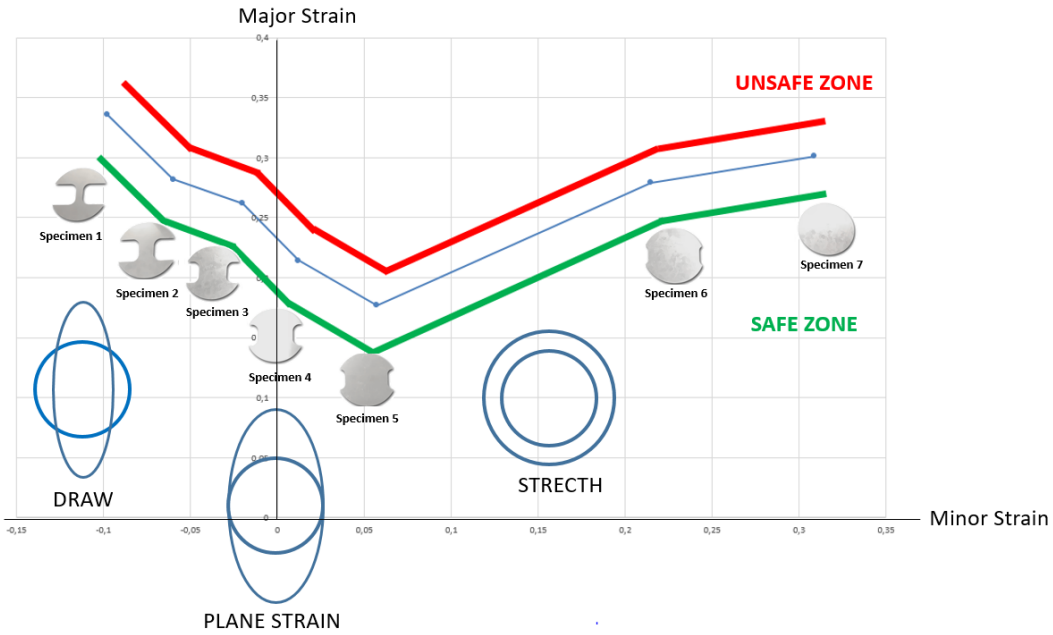

Figure 3.7 Detailed FLC explanation of experimental FLC for 0.5 mm thickness DC04-EK (FLC courtesy from the Metal Forming of Excellence)

Nakajima test results were collected with the GOM-ARAMIS image correlation system integrated into the BUP 600 device as seen in Figure 3.8. ARAMIS compares the pictures with the initial digital image and calculates the displacement and also the deformation of the item characteristics. ARAMIS automatically divides the etched sample's image into little overlapping spaces and defines the corresponding area in the stereo image. The unique calculation method gives high precision results.

By distribution of all image details to the stereo image, the form of the sheet metal in its reference state is measured to support the calibration knowledge of the system. Nevertheless, the image details of the reference image may be allocated to the photographs of the recorded resultant stereo image pairs. Thus, the form and the deformation rate of the sheet metal were exactly recorded and measured for every recording moment once the automated analysis.

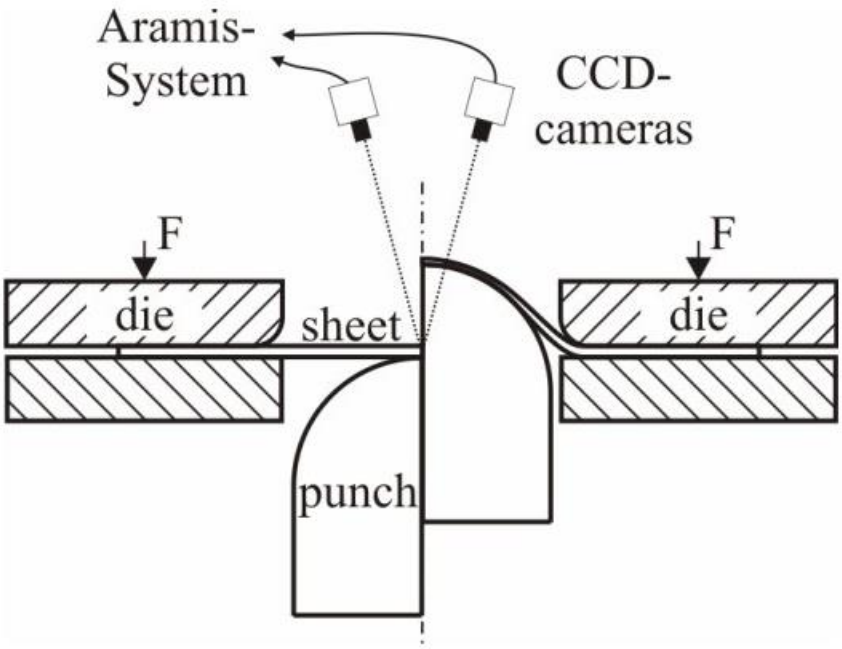

Figure 3.8 Schematic illustration of FLC calculation with Aramis system, (image courtesy of GOM)

The all-deformation behavior of the sample material throughout forming and fracture style are obtained and reportable as final information by recording and evaluating numerous pictures with the corresponding load parameters (force and deviation) throughout the forming process as seen in Figure 3.9.

ARAMIS calculates the characteristic values which are the maximum of major and minor principal strains by the computation of a perfect form of the curve from the captured measuring values [30]. Each specimen's forming behaviors at material failure were repeated three times.

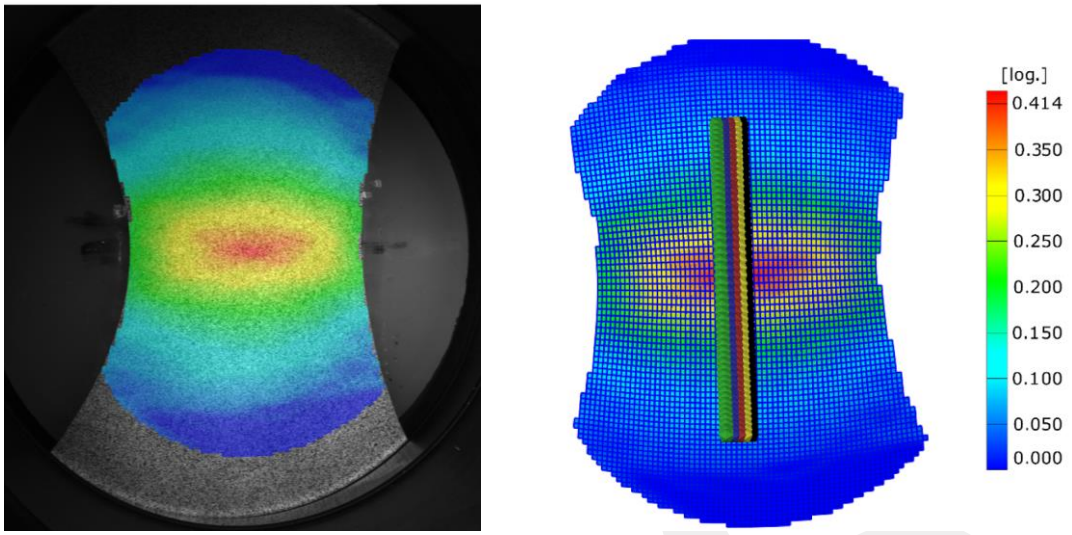

Figure 3.9 Recorded image by CCD cameras and strain distributions obtained from GOM Aramis image (courtesy The Metal Forming Center of Excellence)

3.3.1. Nakajima Test Results

As a result of the punched dome tests, FLC was determined as shown in Table 3.3 and plotted in Excel as seen in Figure 3.10. The error bars on the graph have been obtained by 3 repetitions at each strain point. These results were read as input to the Simufact software with a 10% safety margin and the critical regions were determined from the simulation results.

.

Table 3.3 FLC results from punched dome tests

Minor Strain	Major Strain
-0.322	0.670
-0.253	0.633
-0.181	0.560
-0.096	0.450
0.001	0.382
0.049	0.331
0.252	0.402
0.395	0.459

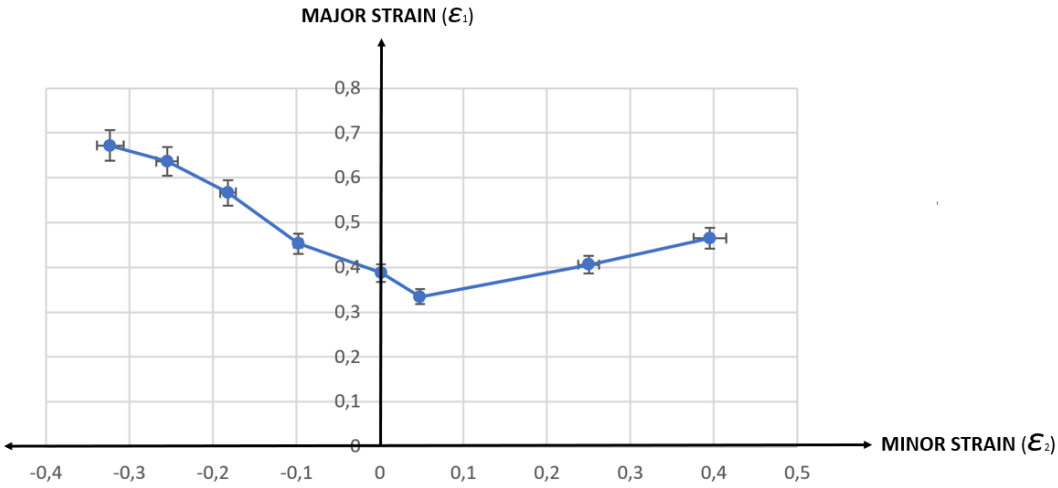

Figure 3.10 Forming limit curve of 0.4 mm thickness DX54D-Z zinc coated (galvanized sheet metal)

CHAPTER 4

SIMULATIONS

In this chapter, manufacturing formability of the sheet metal cover of the cooling group and the CFD flow simulations of the inlet and outlet of the centrifugal pump for three different design alternatives are investigated. The Simufact Forming software has been used for forming simulations and the Autodesk CFD software has been used for CFD simulations.

A 0.4 mm thick DX-54D-Z zinc-coated (galvanized) deep drawing quality sheet metal's FLC results and tensile test results are defined in the Simufact Forming Software. In the sheet metal forming simulation, deep drawing process 3D simulated which is the most critical stage of production because of the thickness of the sheet metal. The press defined on Simufact Forming with 25 mm stroke which is the depth of the deep drawing and punch speed has been set 20 mm/s.

In all forming simulations, dies made rigid without heat conduction, so only blank which is the formed sheet metal has a mesh structure. Sheet-mesh structure applied as a hexahedral type on blanks with three-layer. Remeshing option activated when strain reached 0.4 strain change. CFD simulations have been performed to test uniformity and volumetric flow capacity. In all CFD simulations Reynold Averaged Navier Stokes (RANS) model has been used. For turbulence k-e model has been used.

4.1. Description of the First Model

The first cooling group was designed by adhering to design limits. Motor, impeller, and motor connection part located on the formed sheet metal cover. Due to the design limitations impeller can reach a maximum of 1200 rpms. For this reason, the motor was specially selected for the impeller to reach 1200 rpms. The first designed cooling group can be seen in Figure 4.1.

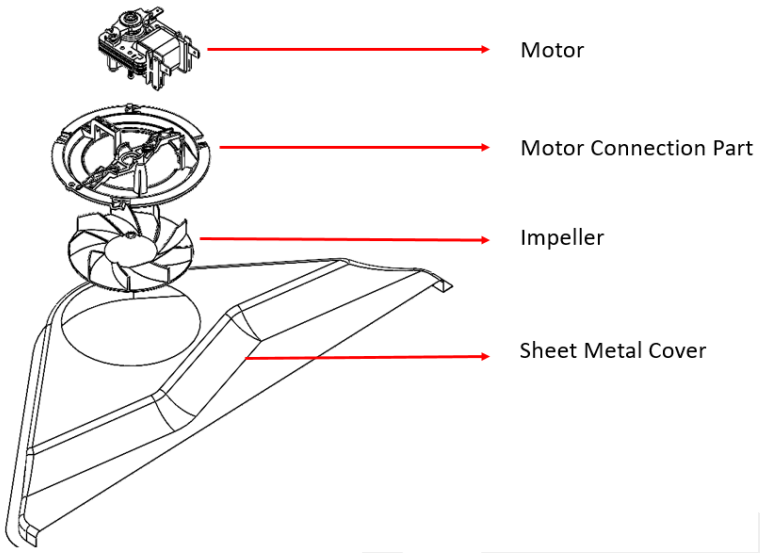

Figure 4.1 Isometric and exploded view of first designed cooling group

4.1.1 Sheet Metal Forming Analysis of the First Model

The model is that standard die set for basic forming. Sheet metal as shown in Figure 4.2 formed between punch, blank holder, and die. 15 kN gas spring has been defined on blank holder.

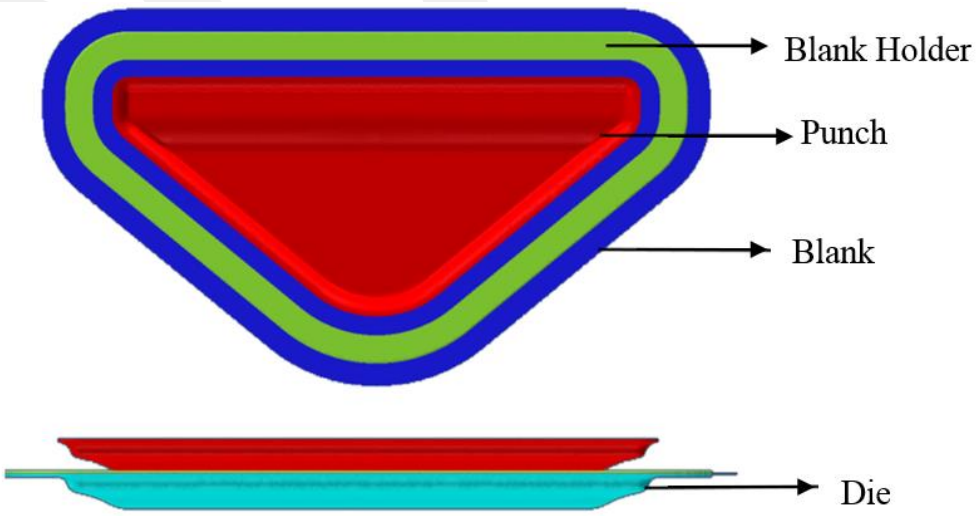

Figure 4.2 The top and front view of the die set for forming first design cooling group's sheet metal cover

In this simulation, dies were rigid without heat conduction so die and punch deformation haven't calculated. Therefore, only a blank has mesh structure with 156966 elements can be seen in Table 4.1. There are 3 layers of sheet-mesh between thicknesses which is 0.4 mm. Also, mesh structure of the blank can be seen in Figure 4.3.

Table 4.1 The forming simulation parameters of first design sheet metal cover

Type	Deep Drawing
Temperature Range	Cold (20°C -50°C)
Simulation	3D
Solver	FE
Matrix Solver	Pardiso Direct Sparse
Ambient Temperature	20.0 °C
Mesher Type	Sheetmesh
Element Type	Hexahedral
Element Size	1.808 mm
Number of Mesh Layer	3
Elements	156966

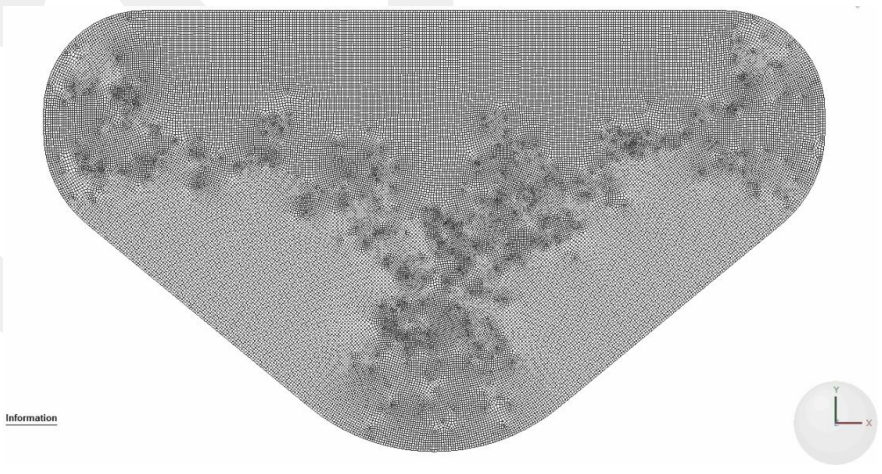

Figure 4.3 Mesh structure of the first designed cooling group sheet metal cover for forming simulation by Simufact

4.1.2. Forming Analysis Results of the First Model

4.1.2.1. Effective Plastic Strain

It is not possible to show the minor and major strain at the same time on the geometry. Therefore, the equivalent plastic strain, which is a scalar value, is shown so that we can see in which regions the deformation is concentrated [30]. As shown in Figure 4.4 bottoms of the radius has more deformations than other regions.

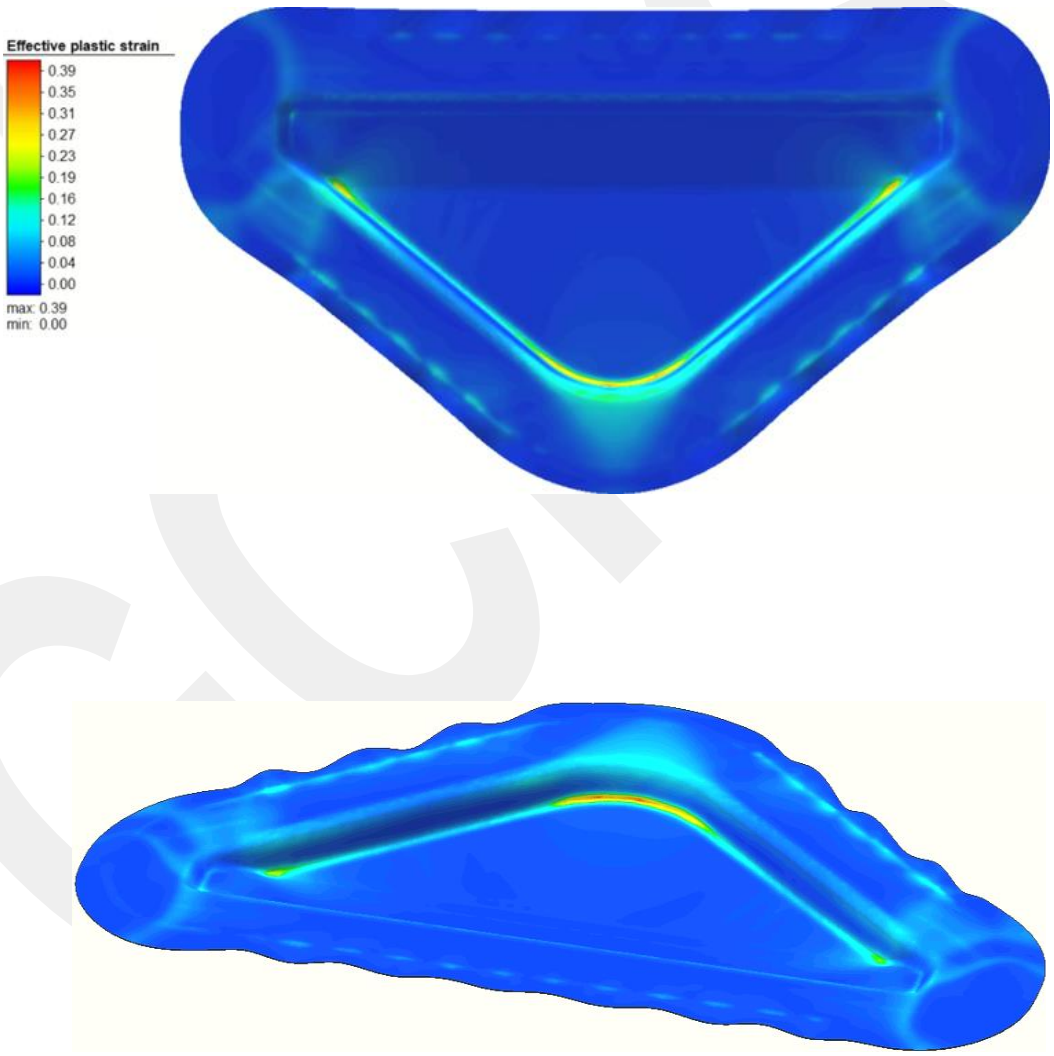

Figure 4.4 Top and isometric view of effective plastic strain distribution visualization from end of the first model sheet metal cover forming simulation

4.1.2.2. Forming Limit Parameters

Forming Limit Curve was read as input to the software. The output images can be seen in Figure 4.5 based on the inputted FLC. Analysis results show that the designed part which is designed by adhering to design limits can be formed without any crack.

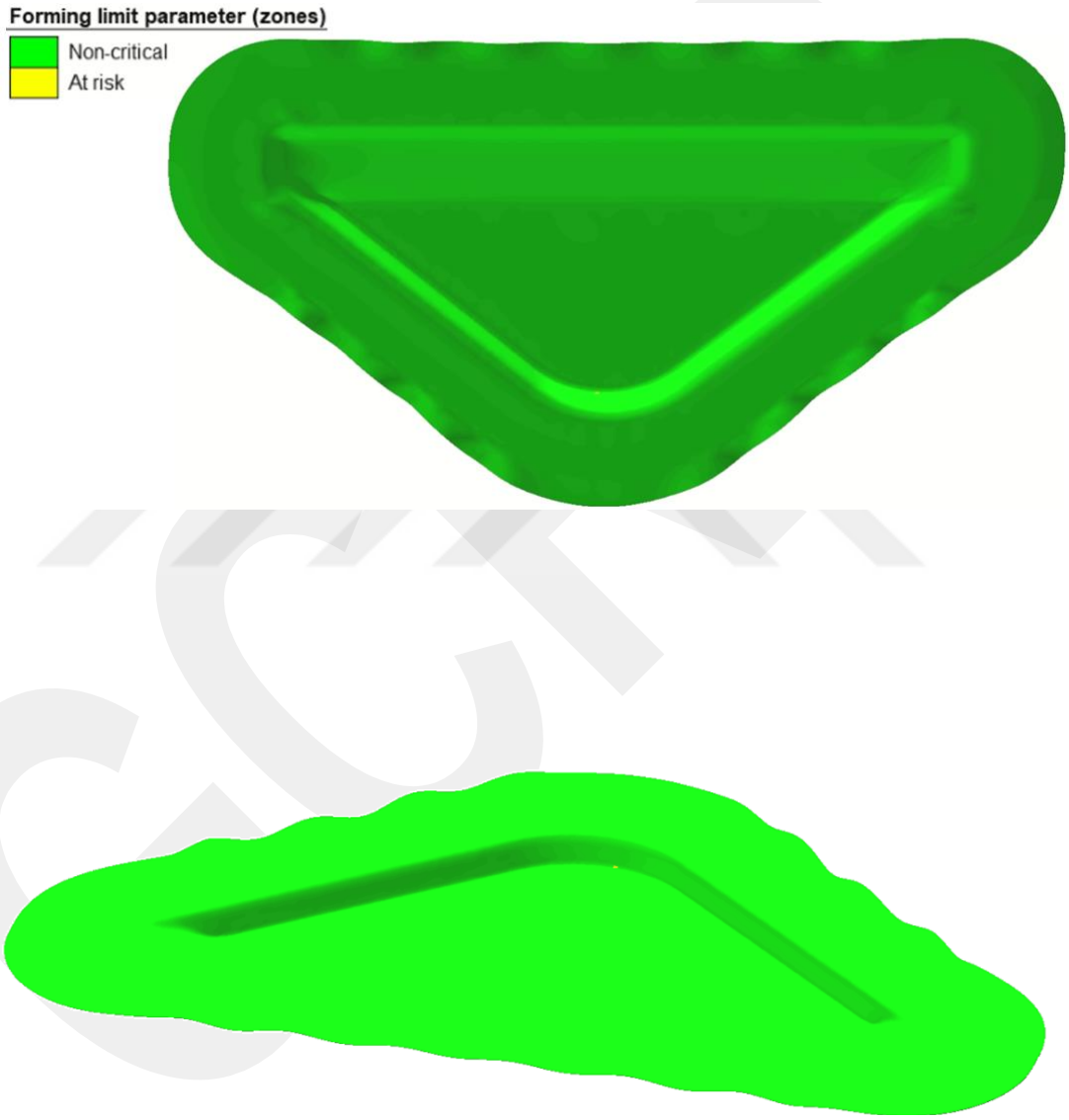

Figure 4.5 Top and isometric forming limit distribution visualization from end of the first design sheet metal cover forming

4.1.3. CFD Analysis of the First Model

4.1.3.1 The Model and the Boundary Conditions

The real challenge at cooling groups is high volumetric flowrate and outlet flow homogeneity. Separation of the air outlet velocity should be less than 25% along the outlet slots. Designed cooling should have a minimum of 300 L/min volumetric flow rate due to the experiences on the industry. 3D modeled cooling group can be seen in Figure 4.6**.** The boundary conditions of the air inlet and outlet were specified as atmospheric pressure as shown in Figure 4.7. Mesh structure can be seen in Figure 4.8.

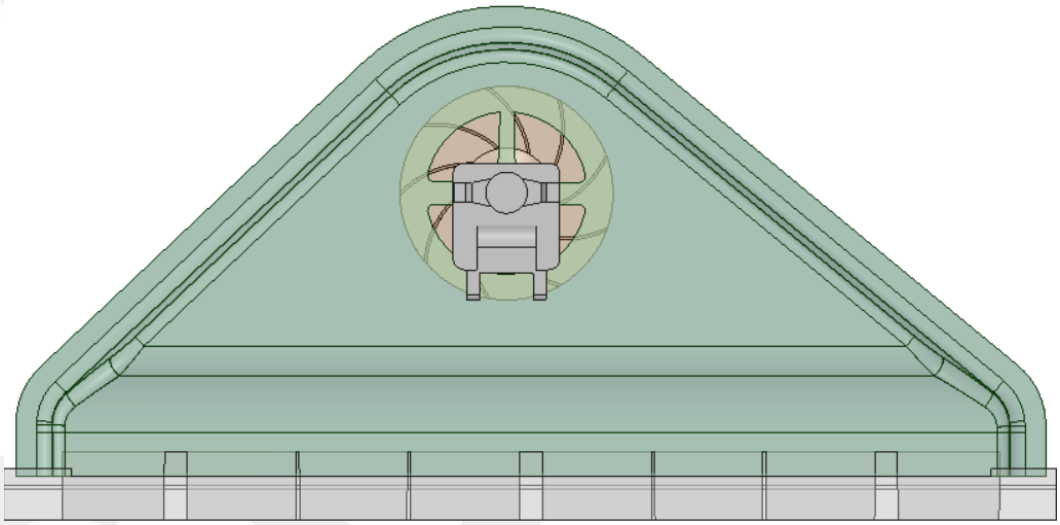

Figure 4. 6 Top view of the first designed cooling group

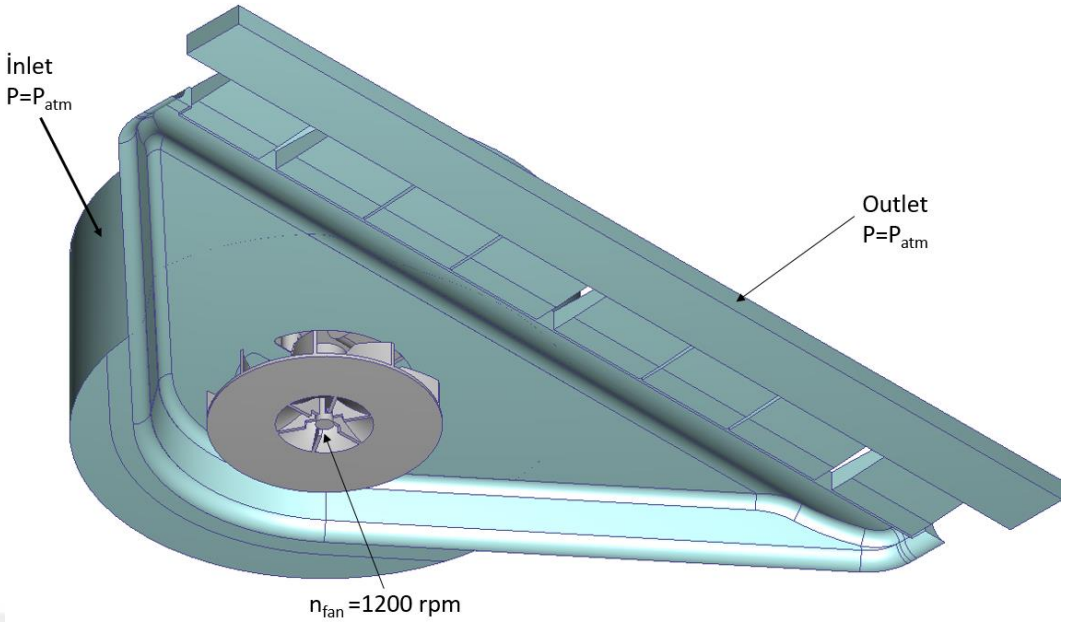

Figure 4. 7 Boundary conditions of first designed cooling group

Table 4.2 Details of CFD Simulations of first designed sheet metal cover on Autodesk CFD

Dimension	3D
Symmetry	No
Time	Steady- State
Flow	Turbulence
Heat Transfer	No
Equation	Reynold Averaged Navier Stokes (RANS) Time averaged equation of fluid motion
Turbulence Model	k-epsilon
Number of Elements	4,948,968

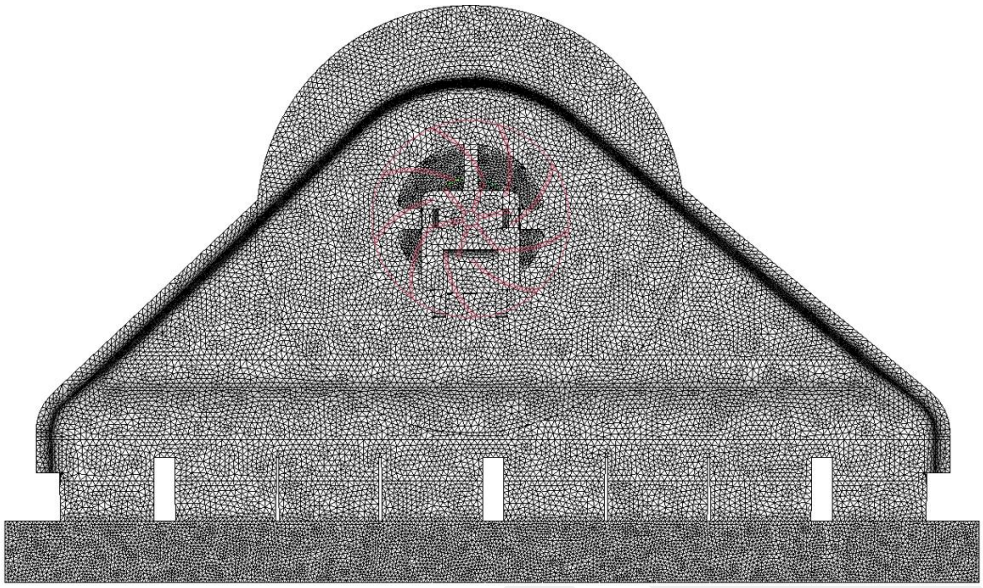

Figure 4.8 Mesh structure of the first model cooling group for CFD simulation with Autodesk CFD

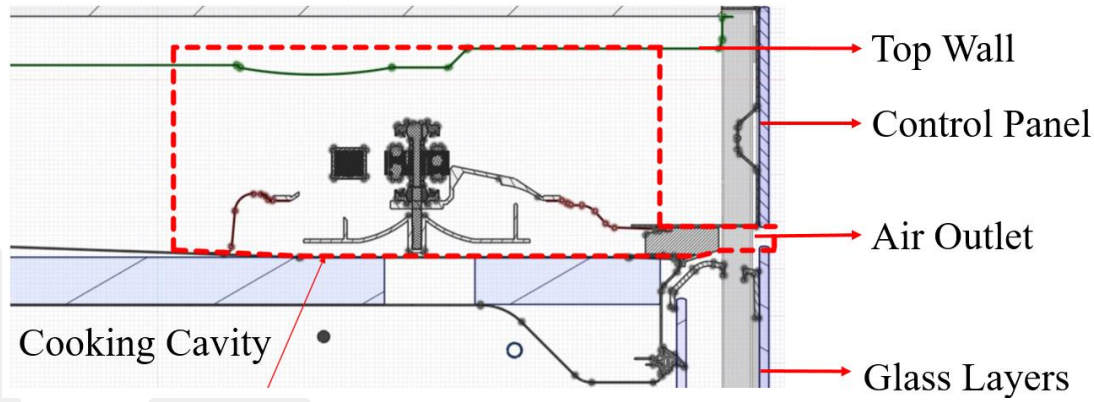

Figure 4.9 The cross section of volume which is modeled in Autodesk CFD

4.1.4. CFD Results of the First Model

The main aim of the cooling group is the cooling glass front door and electronic components. The most important parameters are volumetric flowrate and homogeneity of outlet airflow. As it seems in Figure 4.10, Figure 4.11 and Figure 4.13 the homogeneity of outlet velocity on the slots is less than 25%.

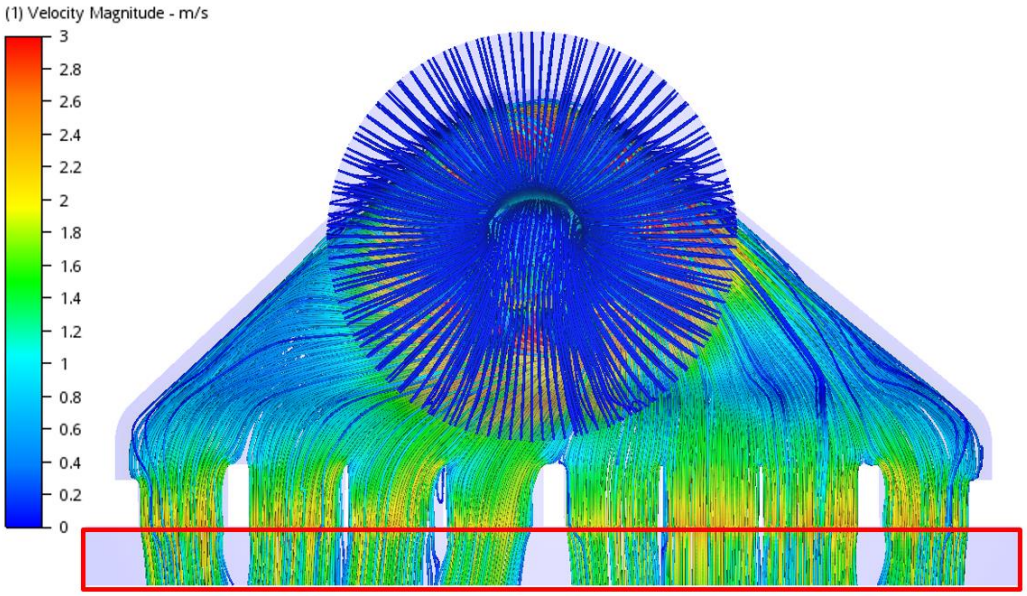

Figure 4.10 Top view of velocity path lines of the first designed cooling group

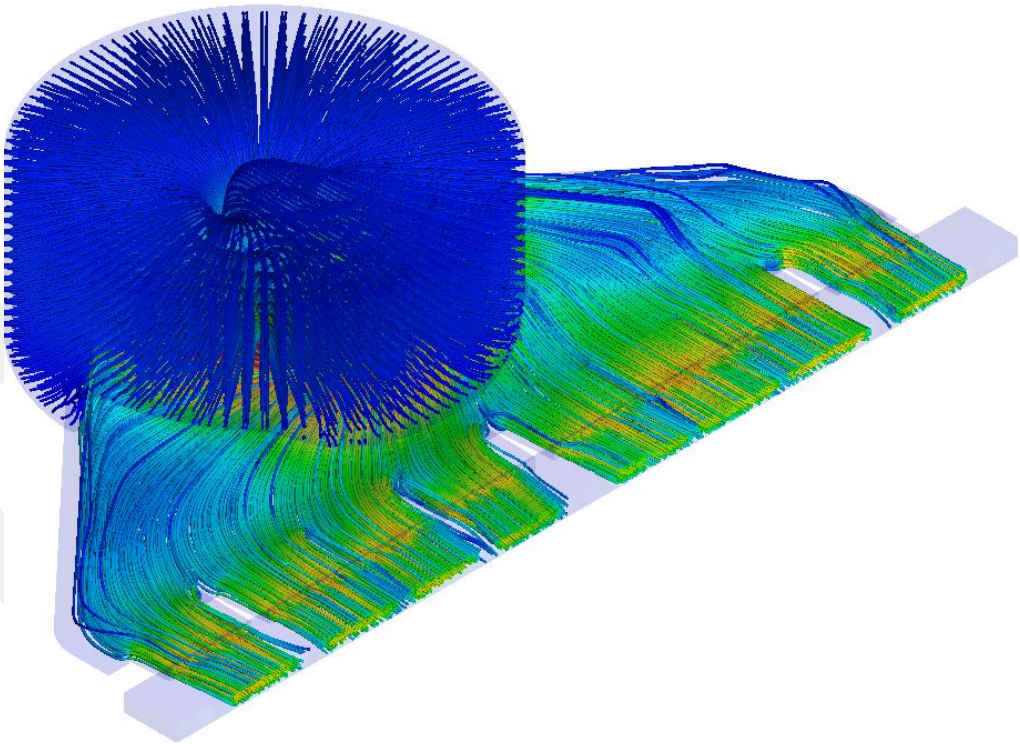

Figure 4.11 Isometric view of velocity path lines of the first designed cooling group

It has been determined that the air from the fan is sucked back because of the geometry design of the sheet metal cover. For this reason, volumetric flow decreases. The sucked air behavior can be seen in Figure 4.12.

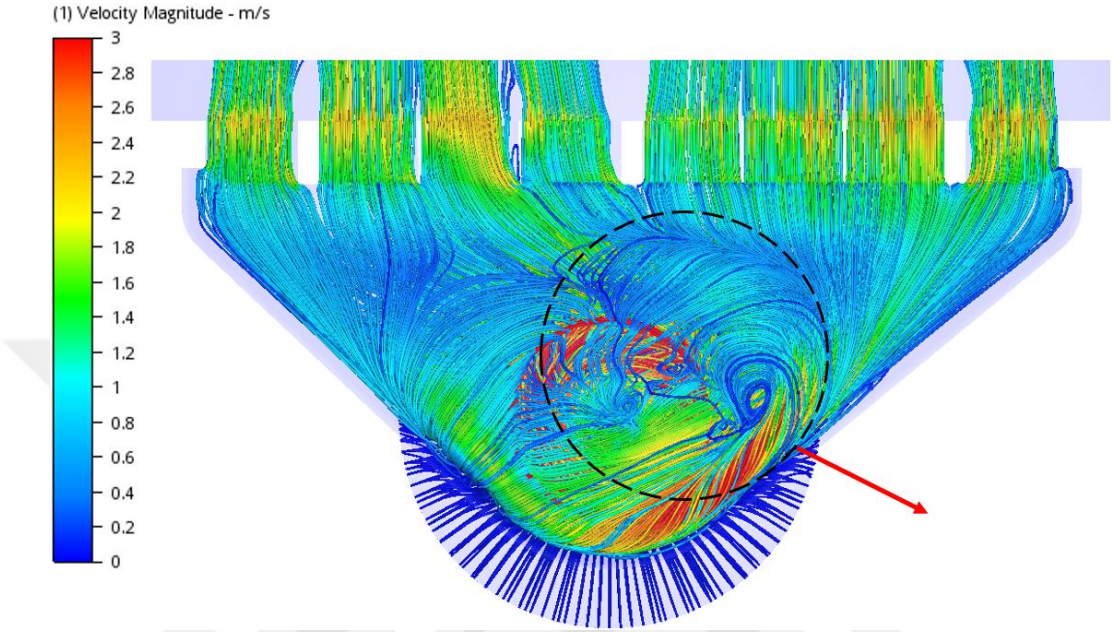

Figure 4.12 Bottom view of velocity path lines of first designed cooling group

Although homogeneity of outlet flow velocity is less than 25% (max 2.1 m/s min 1.82 m/s), the volumetric flow rate which is 232.5 L/min is not enough for cooling glass and electronic components. As seen in Figure 4.13, the air velocity from the outlet slots is around 2 m/s. As a result, although the homogeneity of airflow is less than 25% at the outlet region, volumetric flow rate is not enough for cooling. The problem of first designed geometry is not preventing reversed flows. The design limitations do not allow the increasing of impeller diameter and rpm so the only solution is changing the sheet metal cover geometry.

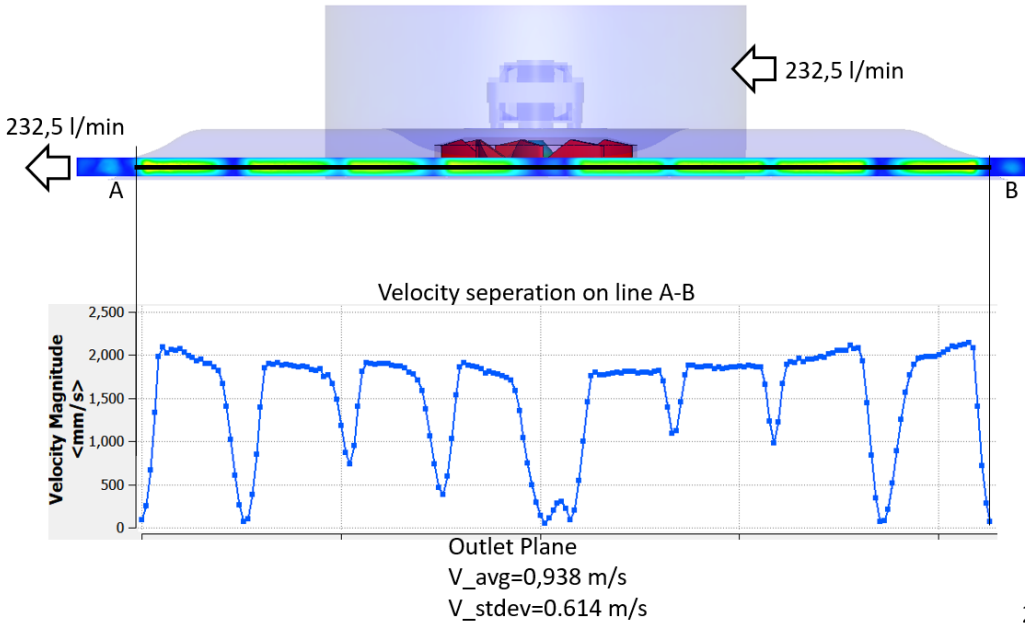

Figure 4.13 Velocity separation on the first model's outlet slots

4.2. Description of the Second Model

The second model cooling group has been re-designed because of the sheet metal cover geometry of the first design. CFD simulations of the first design showed that turbulent regions decrease volumetric flowrate. For this reason, the first designed sheet metal cover changed to a well-known turbo-machinery shape which is snail-shaped design as seen in Figure 4.14.

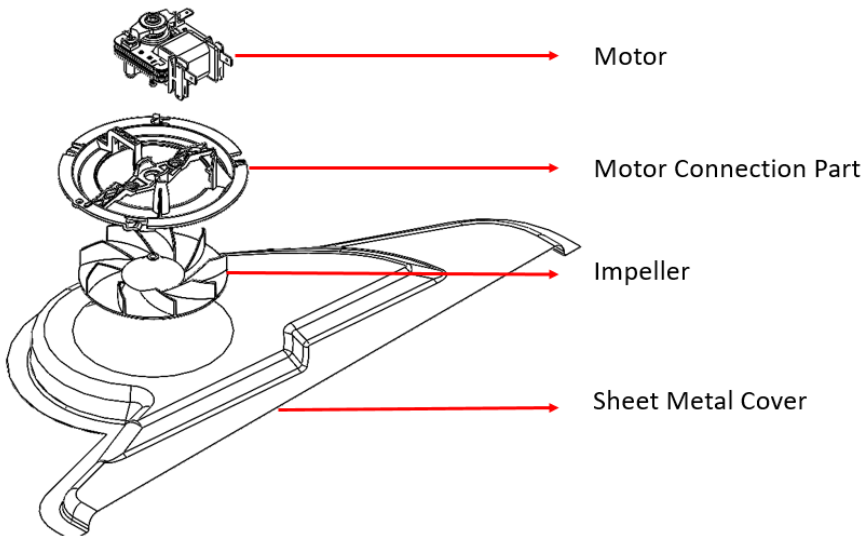

Figure 4.14 Isometric and exploded view of the second designed cooling group

4.2.1. Sheet Forming Analysis of the Second Model

The second model is the standard die set for basic forming. Sheet metal as shown in Figure 4.15 is formed between punch, blank holder with 15 kN gas spring and die. Two simulations are made on the second model. Tears occurred in the first blank design and a 70 mm diameter hole was added to the second die design to prevent this. The location and size of the hole was located according to the connection detail of the motor connection part.

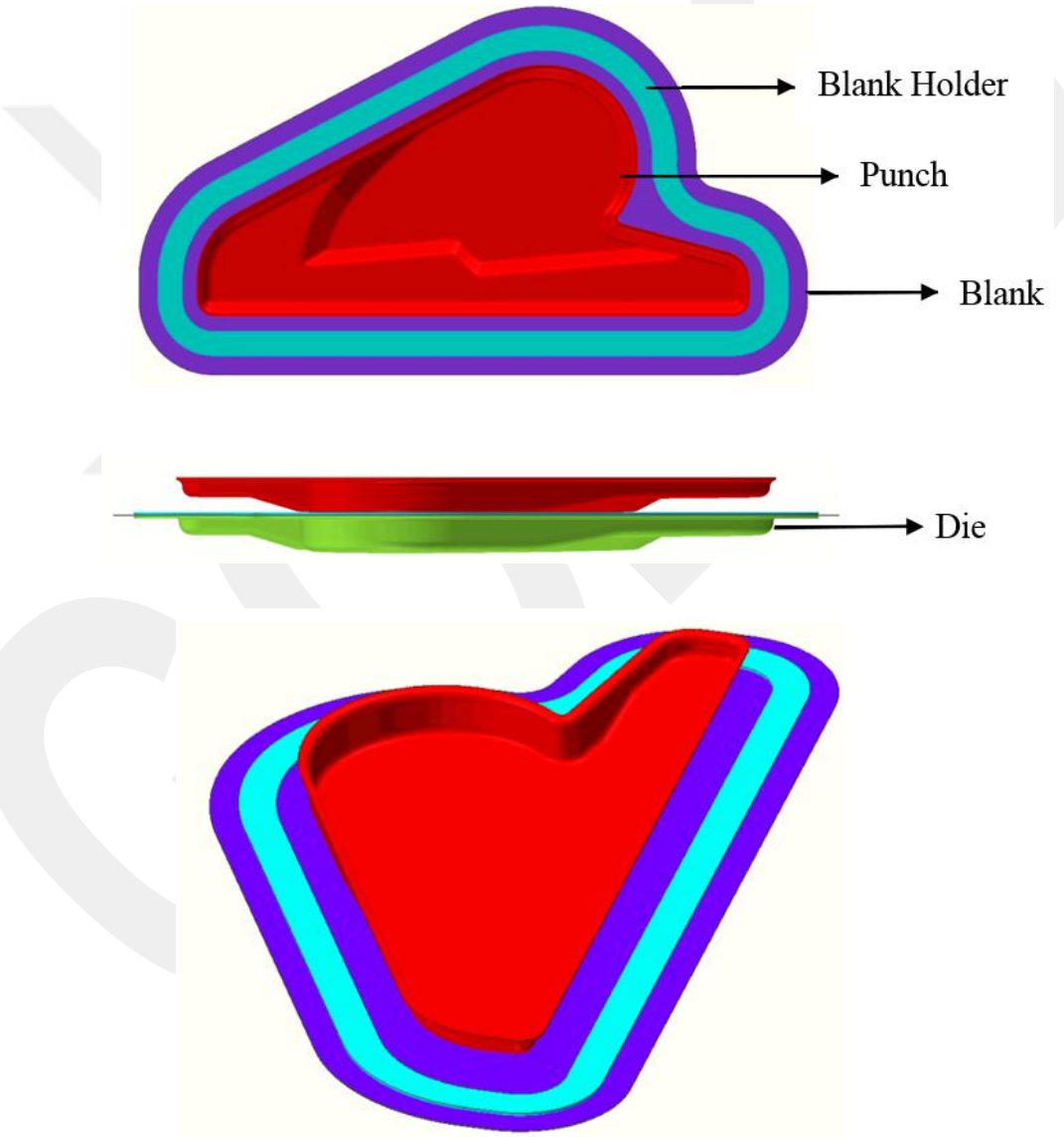

Figure 4.15 The top, front and isometric views of the die set for forming the first design cooling group's sheet metal cover

In this simulation, dies were rigid without heat conduction, so die and punch deformation were not calculated. Therefore, only blanks have a mesh structure with 133,268 and 128,569 elements can be seen in Table 4.2. There are 3 layers of sheet-mesh between thicknesses, which is 0.4 mm. Also, the mesh structure of blanks can be seen in Figure 4.16.

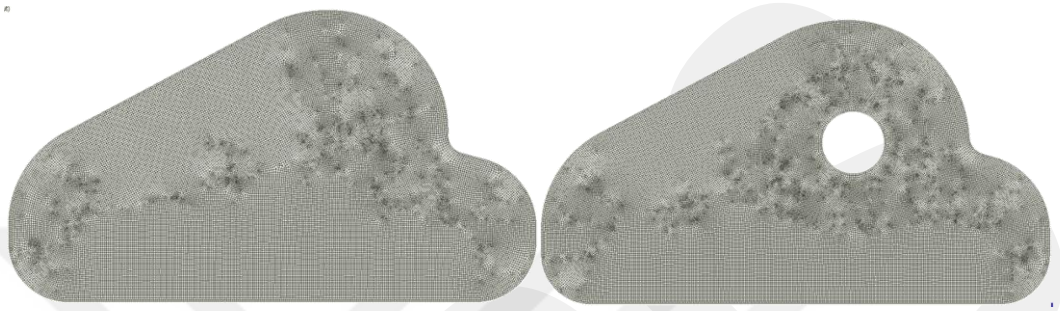

(a) (b)

Figure 4.16 Mesh structures of second designed cooling group sheet metal cover without a hole (a) and with a hole (b)

Table 4.3 The forming simulation parameters of second design sheet metal cover

Type	Deep Drawing
Temperature Range	Cold (20°C -50°C)
Simulation	3D
Solver	FE
Matrix Solver	Pardiso Direct Sparse
Ambient Temperature	20.0 °C
Mesher Type	Sheetmesh
Element Type	Hexahedral
Element Size	2 mm
Number of Mesh Layer	3
Elements (Figure 4.15-a)	133,268
Elements (Figure 4.15-b)	128,569

4.2.2. Forming Analysis Results of the Second Model

4.2.2.1. Effective Plastic Strain

It is not possible to show the minor and major strain at the same time on geometry. Therefore, the equivalent plastic strain, which is a scalar value, is shown so that we can see in which regions the deformation is concentrated [30]. As shown in Figure 4.17 the corner radiuses have more deformations than other regions.

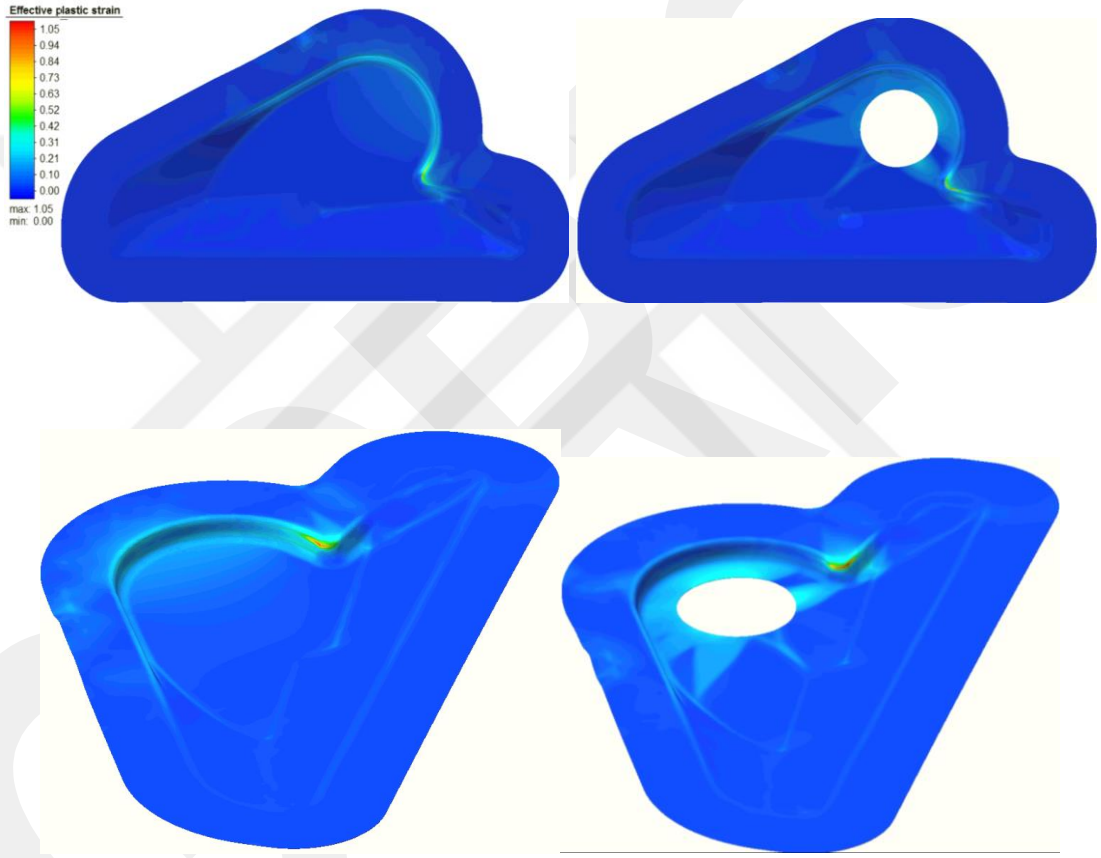

(a) (b)

Figure 4.17 Top and isometric view of effective plastic strain distributions visualization from the end of the second model sheet metal cover forming. (all results have a common legend)

4.2.2.2. Forming Limit Parameters

The forming limit curve was input to the software. The output images that can be seen in Figure 4.18 are based on the inputted FLC. Analysis results show that the designed part which is designed by adhering to design limits has cracks. Tears occurred when the press stroke at 15 mm at the corner. The corner radius of snail shape is too little to form. So that, tears occurred in that area during the deep drawing process.

To prevent tears without any radius change, the hole has opened which is diameter of 70 mm for improved material flow and to prevent tears. In this way, tears again occurred but press stroke has increased from 15.2 to 16.5 mm which is 5,6%. The difference can be seen in Table 4.4 The hole location specially selected. The second step of forming is hole drilling for the motor connection part and the first hole's deformed shape will be a waste of sheet metal.

Table 4.4 The stroke and forming difference for the second design between blank with hole and without hole

Type of design	Press stroke when tear occurred	Forming%
Blank without hole	15.2 mm	64.6
Blank with hole Ø70 mm	16.5 mm	70.2

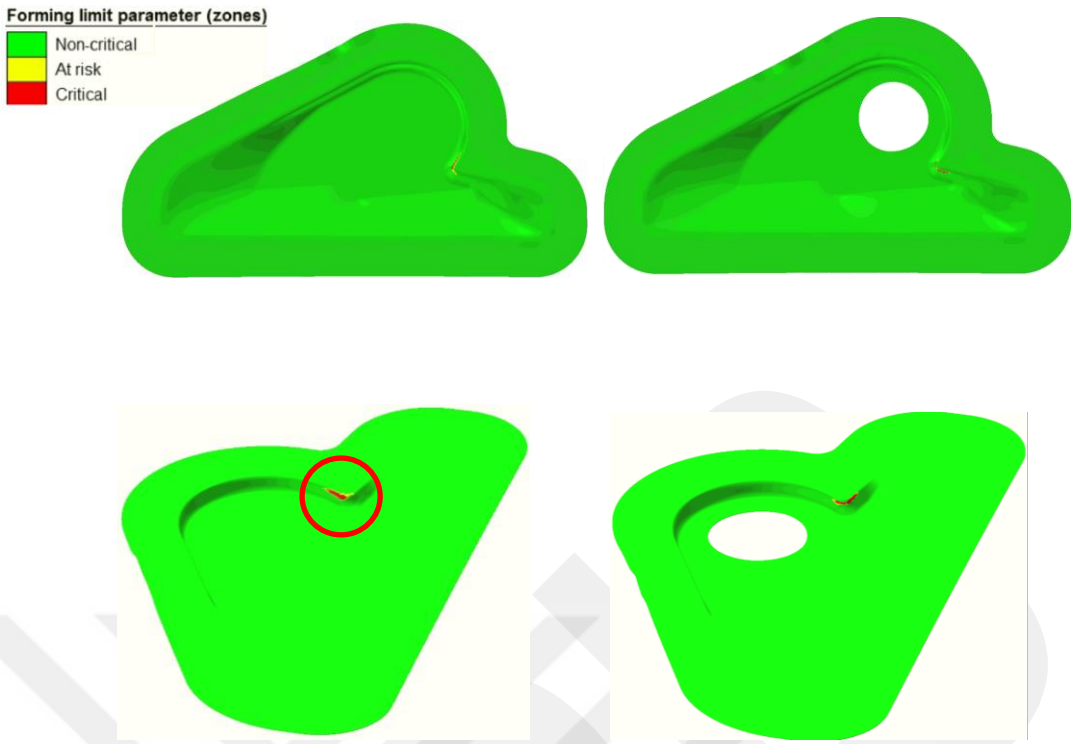

Figure 4.18 Top and isometric forming limit distributions visualization from end of the second model sheet metal cover forming

4.3. Description of the Third Model

The third model cooling group re-designed because of formability problems at sheet metal cover geometry. For this reason, the sheet metal cover's corner radii are increased because tears occurred at the bottom of the radius at the second model as it seems in Figure 4.19. In this way, it was expected that tearing would be prevented by expended the radius from 16 mm to 28 mm. Isometric and exploded view of the third cooling group designed can be seen in Figure 4.20.

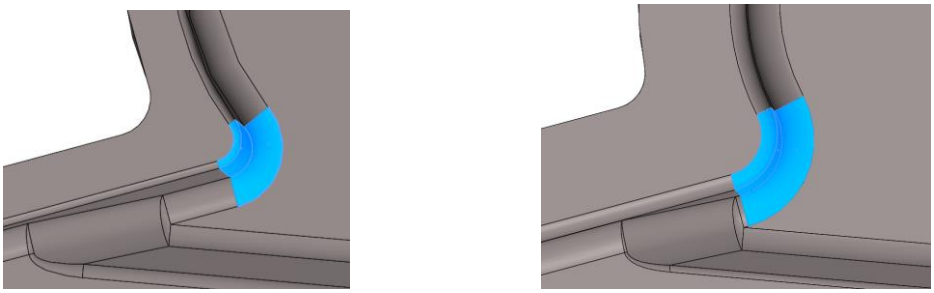

The Second Designed Model The Third Designed Model

Figure 4.19 The expanded radius from 16 mm to 28 mm

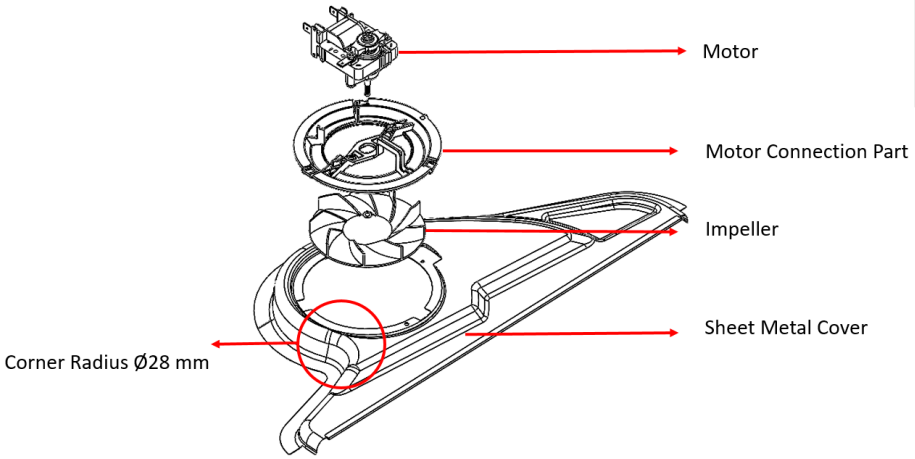

Figure 4.20 Isometric and exploded views of the third designed cooling group

4.3.1 Sheet Forming Analysis of The Third Model

The third model is the standard die set for basic forming. Sheet metal as shown in Figure 4.21 formed between punch, blank holder with 15 kN gas spring and die. Two simulations are made on the third model. Tears occurred in the first blank design and a 70 mm diameter hole was added to the second die design to prevent this. The location and size of the hole were chosen according to the connection detail of the motor connection part.

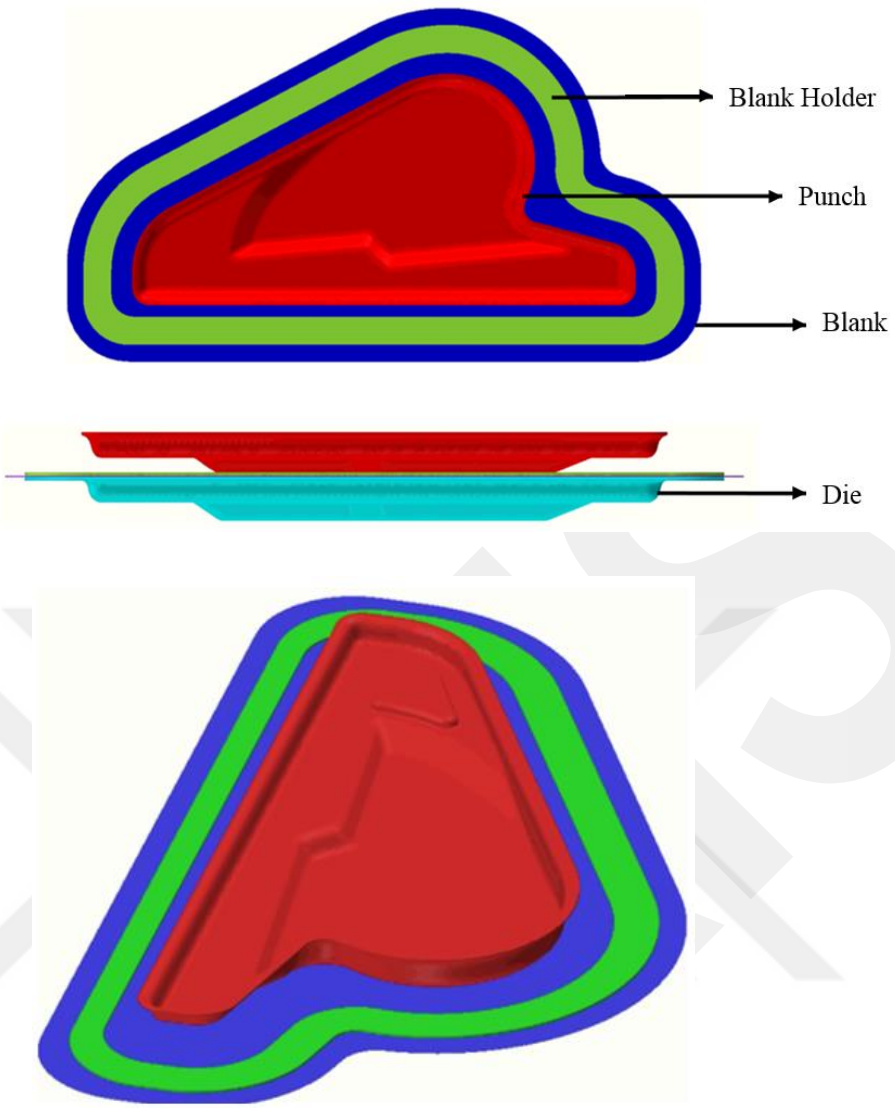

Figure 4.21 The top, front and isometric views of the die set for forming third design cooling group's sheet metal cover

In these simulations, dies were rigid without heat conduction so the die and punch deformation were not calculated. Therefore, only blanks have a mesh structure with 114,966 and 109,562 elements can be seen in Table 4.4. There are 3 layers of sheet-mesh between thicknesses, which is 0.4 mm. Also, mesh structures of blanks can be seen in Figure 4.22.

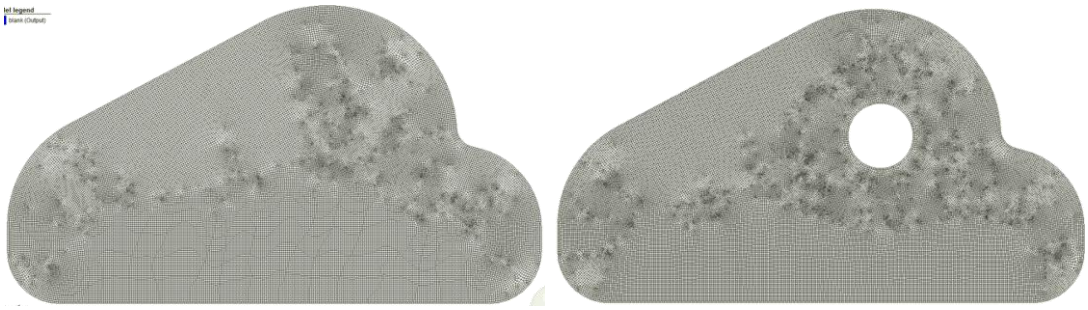

a b

Figure 4.22 Mesh structures of the third designed cooling group sheet metal cover without hole (a) and with hole (b)

Table 4.5 The forming simulation parameters of the third design sheet metal cover

Type:	Deep Drawing
Temperature Range:	Cold (20°C -50°C)
Simulation:	3D
Solver:	FE
Matrix Solver:	Pardiso Direct Sparse
Ambient Temperature:	20.0 °C
Mesher Type:	Sheetmesh
Element Type:	Hexahedral
Element Size:	2 mm
Number of Mesh Layer:	3
Elements (Figure 4.21-a)	114,966
Elements (Figure 4.21-b)	109,562

4.3.2. Forming Analysis Results of the Third Model

4.3.2.1. Effective Plastic Strain

As shown in Figure 4.23 the corner radii have more deformations than other regions. The blank with a 70 mm diameter hole has less deformation because of the hole. The 70 mm diameter hole expanding and preventing the tears at bottom of the radiuses.

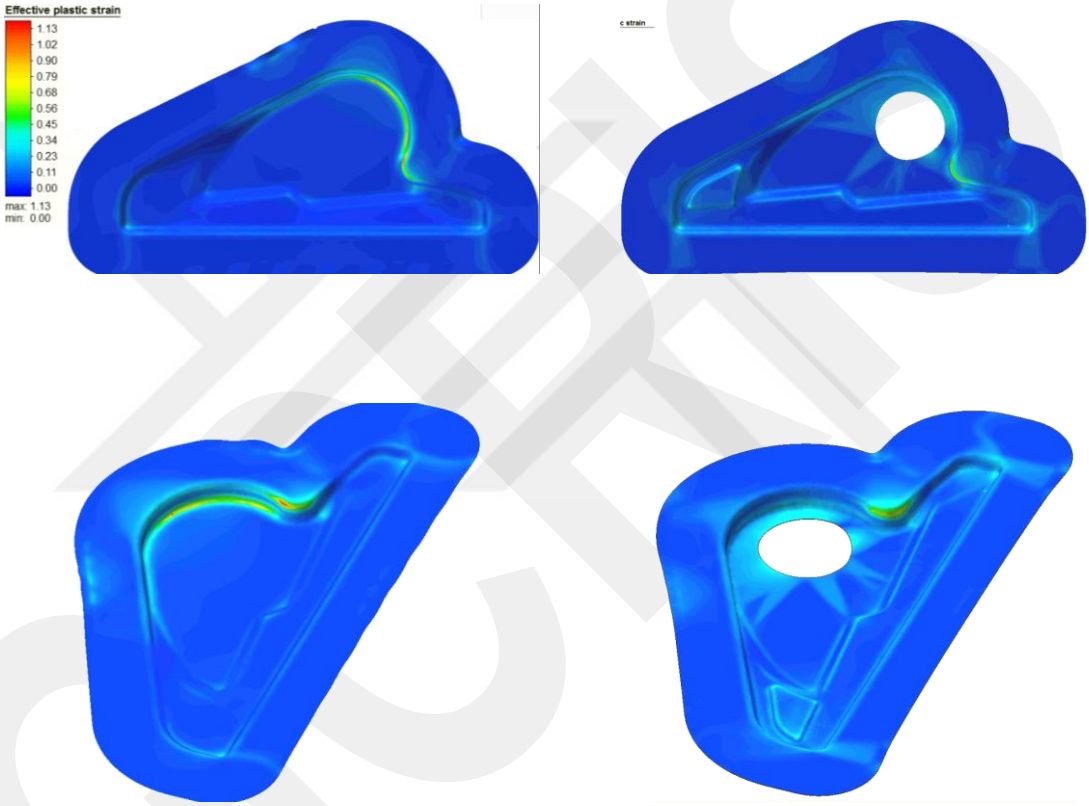

Figure 4.23 Top and isometric view of effective plastic strain distributions visualization from end of third model sheet metal cover forming (all results have a common legend)

4.3.2.2. Forming Limit Curve

Forming Limit Curve was read as input to the software. The output images can be seen in Figure 4.24 based on the inputted FLC. Analysis results show that the designed part which is designed by adhering to design limits has cracks while forming. Tears occurred when press stroke at 20,5 mm at the corner.

To prevent tears without any change of geometry, the hole has opened which is diameter 70 mm to material flow and prevent tears. In this way, forming has completed without any tears. The difference can be seen in Table 4.6.

Table 4.6 The stroke and forming difference at third design between blank with hole and without hole

Type of design	Press stroke when tear occurred	forming %
Blank without hole	20,5	87.2
Blank with hole Ø70 mm	23,5	100

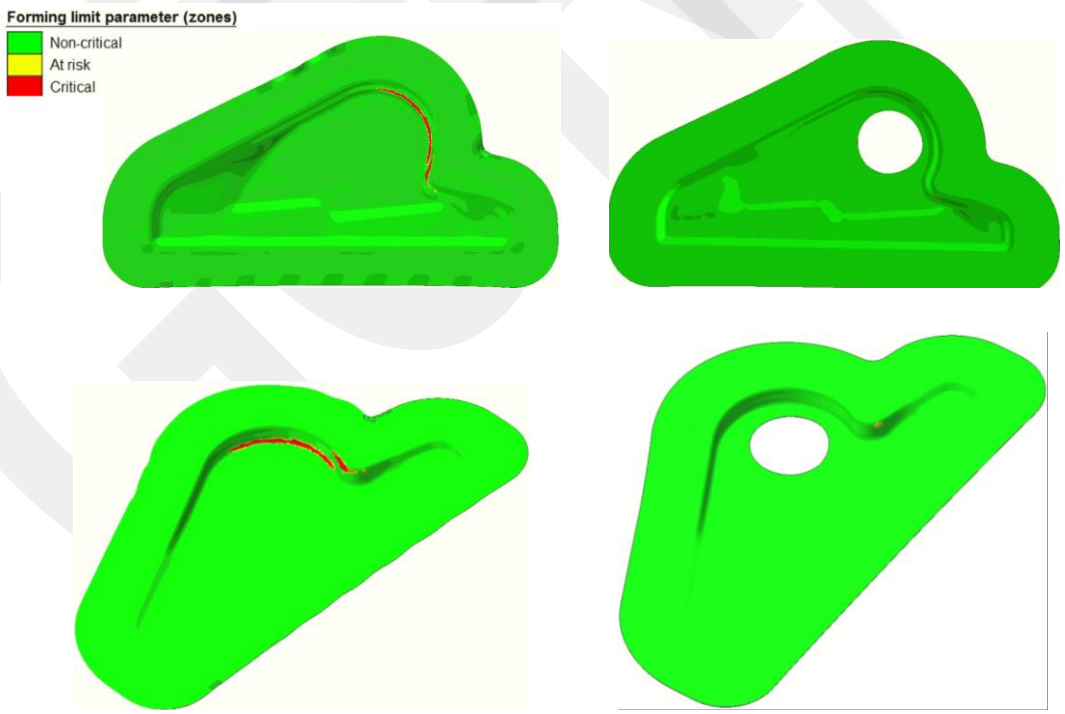

Figure 4.24 Top and isometric forming limit distributions visualization from end of the second model sheet metal cover forming

The 70 mm diameter hole expanded and prevented tears in critical regions of forming. As it seems in Figure 4.25-a material flows critical radius bottoms. The maximum radius expansion measured 12.49 mm can be seen in Figure 4.25-b.

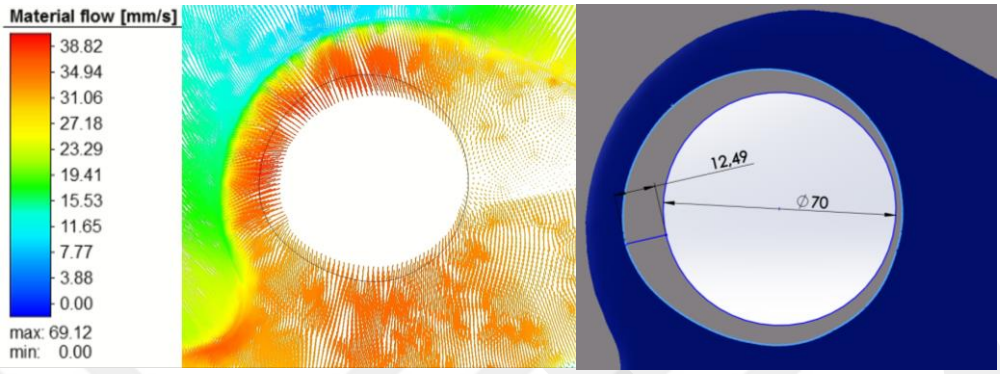

(a) (b)

Figure 4.25 The 70 mm diameter hole expansion and material flow lines on third design sheet metal cover

The hole diameter and location are a very important parameter not to affect other operations of forming processes. The hole was positioned close to critical forming areas and its diameter was adjusted so that it did not affect the cutting for the motor connection part. As seen in Figure 4.26 the expanded hole is very close to the motor connection cut-out.

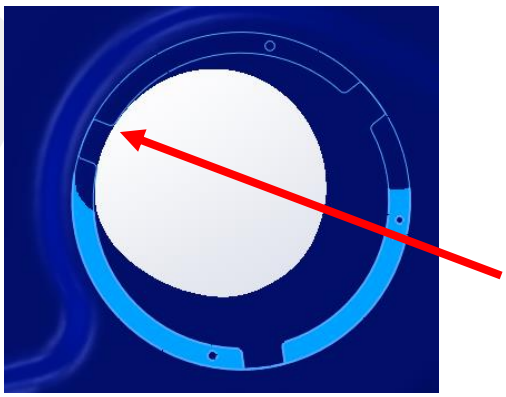

Figure 4.26 The location of the expanded hole and motor connection cut out locations

4.3.3. CFD Analysis of the Third Model

4.3.3.1. Model Description and Boundary Conditions

To control volumetric flowrate and outlet flow homogeneity parameters at the third designed cooling group, CFD simulations were made by Autodesk CFD Software with RANS modeled. 3D modeled cooling group and chimney which are directly connected to the cooking cavity can be seen in Figure 4.27**.** The boundary conditions of the air inlet and outlet were determined as atmospheric pressure as shown in Figure 4.27. Mesh structure can be seen in Figure 4.28.

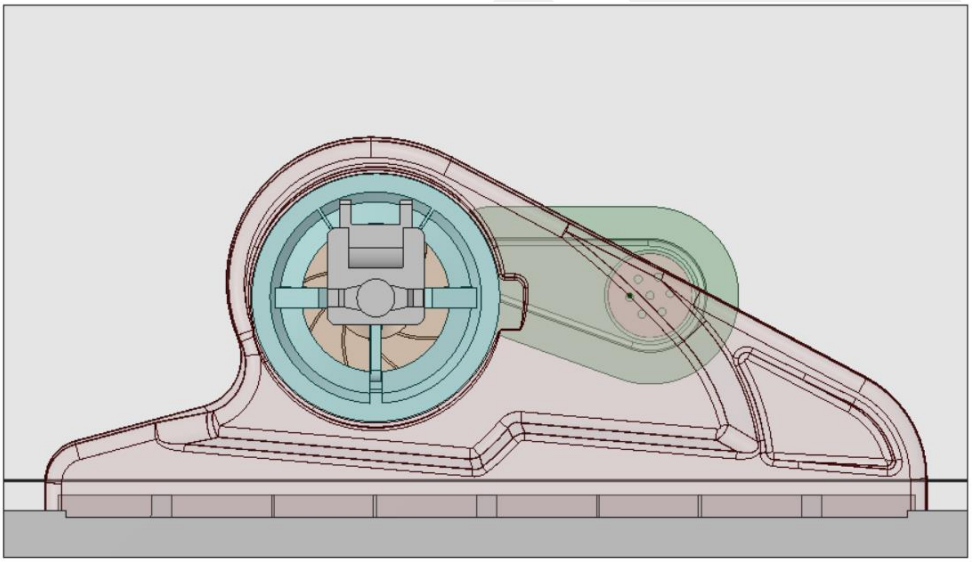

Figure 4.27 Top view of the third designed cooling group

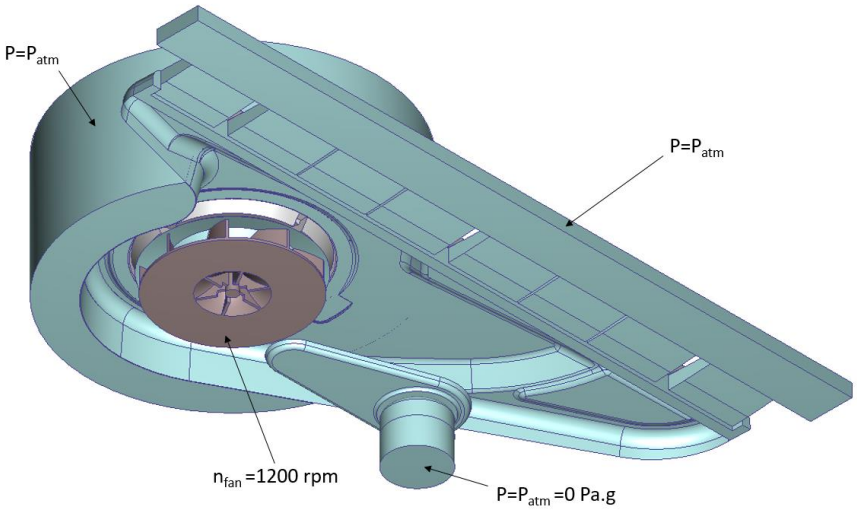

Figure 4.28 Boundary conditions of third designed cooling group

Mesh structure can be seen in Figure 4.29. Because of computational insufficiency, all model volume and details weren't calculated. The calculated volume can be seen in Figure 4.30. The detailed information can be seen in Table 4.7.

Table 4.7 Details of CFD Simulations of third designed sheet metal cover on Autodesk CFD

Dimension	3D
Symmetry	No
Time	Steady- State
Flow	Turbulence
Heat Transfer	No
Equation	Reynold Averaged Navier Stokes (RANS) Time averaged equation of fluid motion
Turbulence Model	k-epsilon
Number of Elements	5,202,702

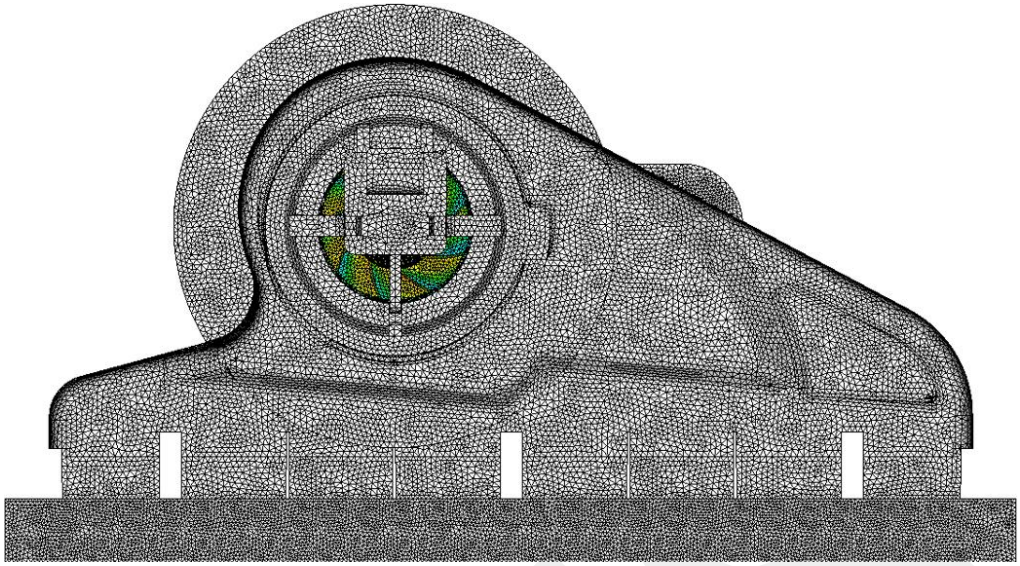

Figure 4.29 Mesh structure of the third model cooling group to CFD simulation

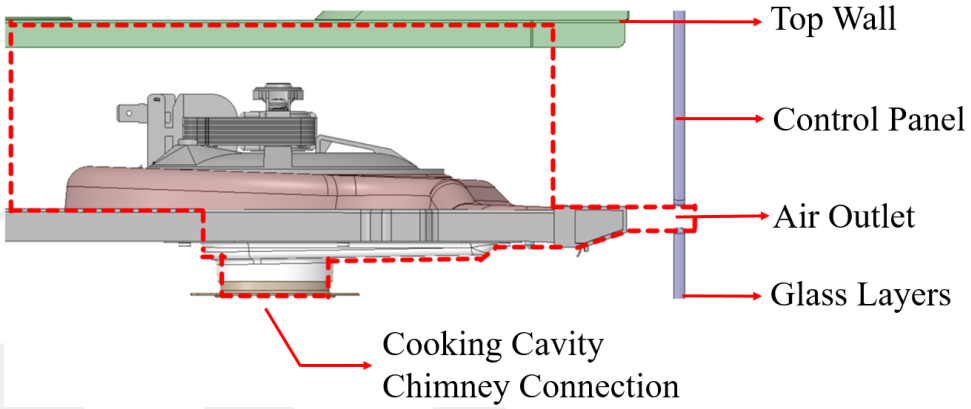

Figure 4.30 The cross section of the volume calculated on Autodesk CFD

4.3.4. CFD Results of the Third Model

The aim of the cooling group is the cooling glass front door and electronic components. The most important parameters are volumetric flowrate and homogeneity of outlet airflow. As it is seen in Figure 4.31, Figure 4.32 and Figure 4.34 the uniformity of the outlet flow velocity is less than 25% (max 2.6 m/s, min 2.12 m/s). Also, there is a flow from the cooking cavity that can be seen in Figure 4.33.

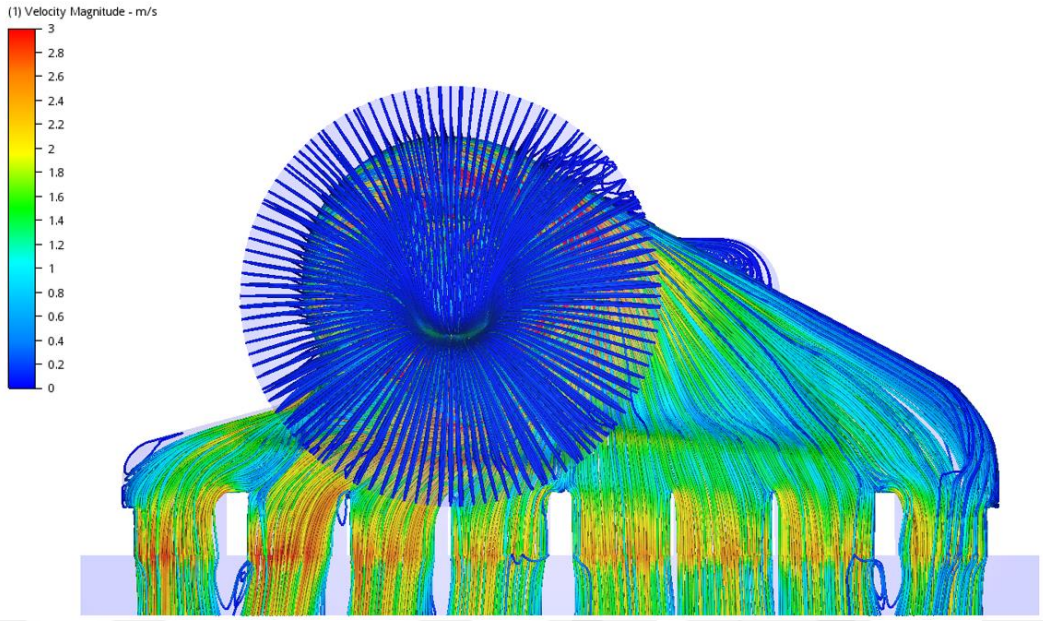

Figure 4.31 Top view of velocity path lines of the third designed cooling group

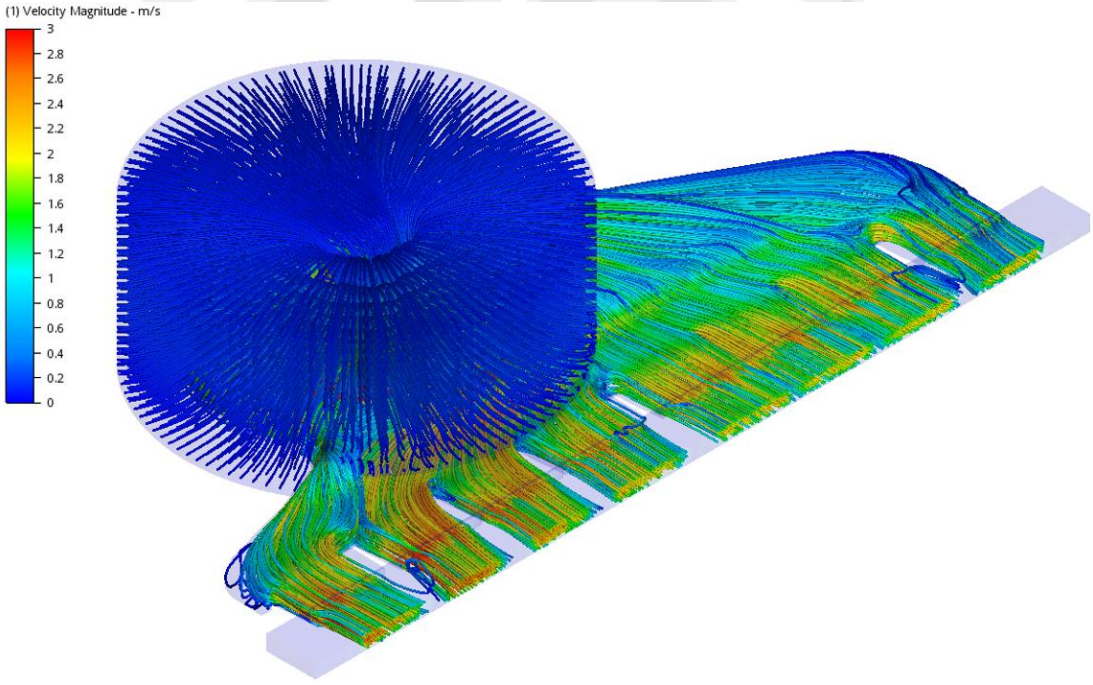

Figure 4.32 Isometric view of velocity path lines of the third designed cooling group

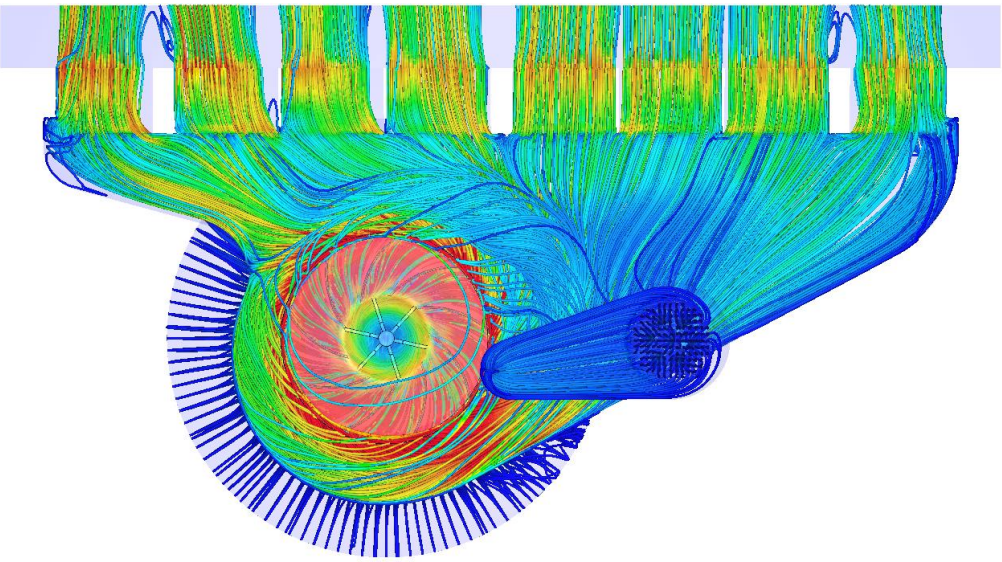

Figure 4.33 Bottom view of velocity path lines of third designed cooling group

The uniformity of outlet flow and volumetric flow rate which is 305.5 L/min is adequate for cooling glass and electronic components when compared to the benchmark products. As seen in Figure 4.34 the air velocity from the outlet slots is around 2,5 m/s. The volume of the cooking cavity is 90 liters and the sucked air from the cooking cavity which is 2.5 L/min is enough because increasing volumetric flow rate suction from the cooking cavity can cause efficiency decrease.

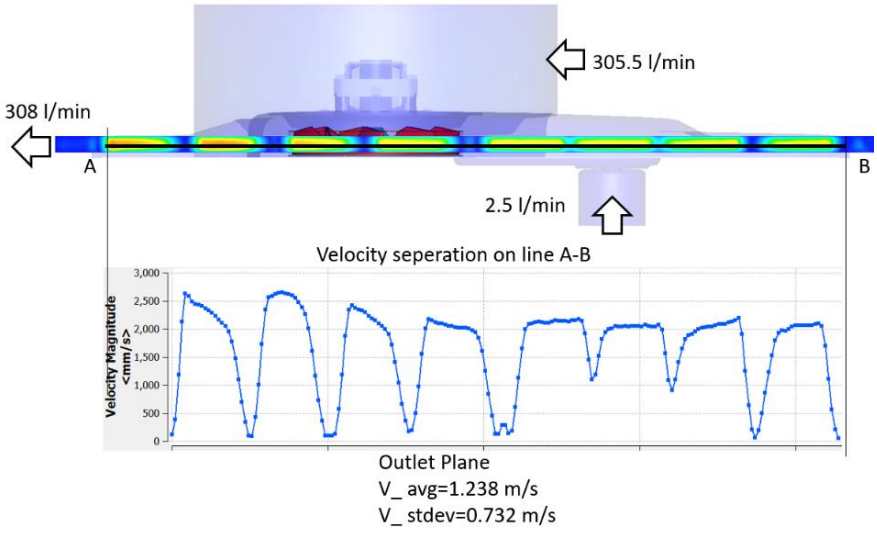

Figure 4.34 Velocity separation on the third model's outlet slots

4.4 Design of the Motor Connection Part

The motor connection part geometry is a very important parameter to volumetric flow rate. This part is very close to the inlet of the impeller so that this parameter directly affects the flow rate and homogeneity.

Another important issue is cooling of the motor. The flowrate on the motor should be smooth and regular to the cooling of the electrical motor. So, the inlet area and cross section optimization should be fine. To optimize the shape of the motor connection part, CFD simulations were performed by RANS (Reynolds Averaged Navier Stokes) model.

4.4.1 The First Motor Connection Design CFD Simulation

4.4.1.1 Description of the First Motor Part Design

The main purpose of the first model was to connect the motor and sheet metal cover together. A gap has been added to the rear of the motor to cool the motor as it seems in Figure 4.35. The motor connection part cross section has a dome shape as it seems in Figure 4.36 because of the impeller geometry.

.

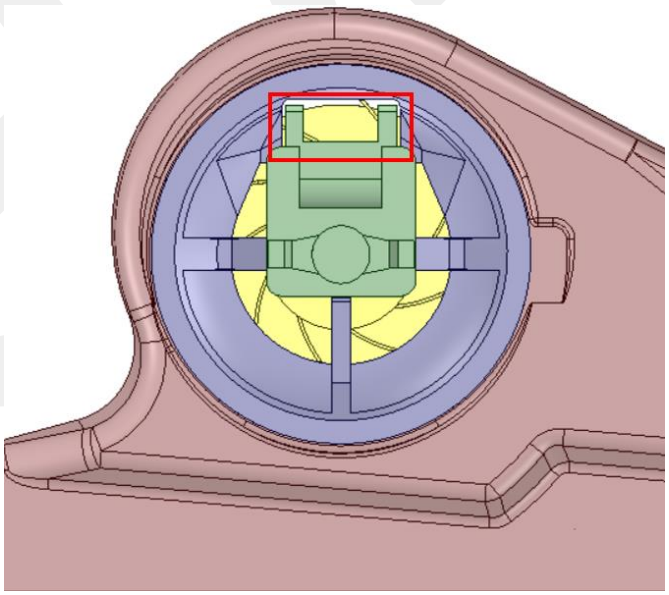

Figure 4.35 The first type of motor connection part

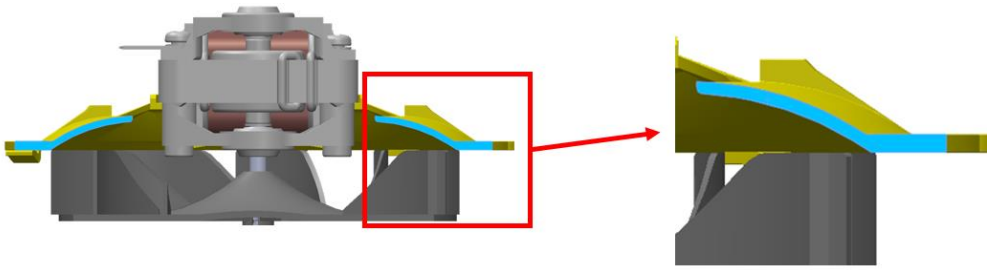

Figure 4.36 The cross section of the first type of motor connection part

4.4.1.2 The First Motor Connection Design CFD Result

CFD simulations showed that the cross section of the first designed motor connection part is not effective in cooling electric motor and not suitable for horizontal air flows entering the inlet area as seen in Figure 4.37. Also, this geometry caused a decrease in the volumetric flow rate.

Another important problem is air leakage to outside at the rear side of motor connection parts. The gap at the rear was produced to cool the coil part of the motor, but as seen in Figure 4.38, this solution was not adequate.

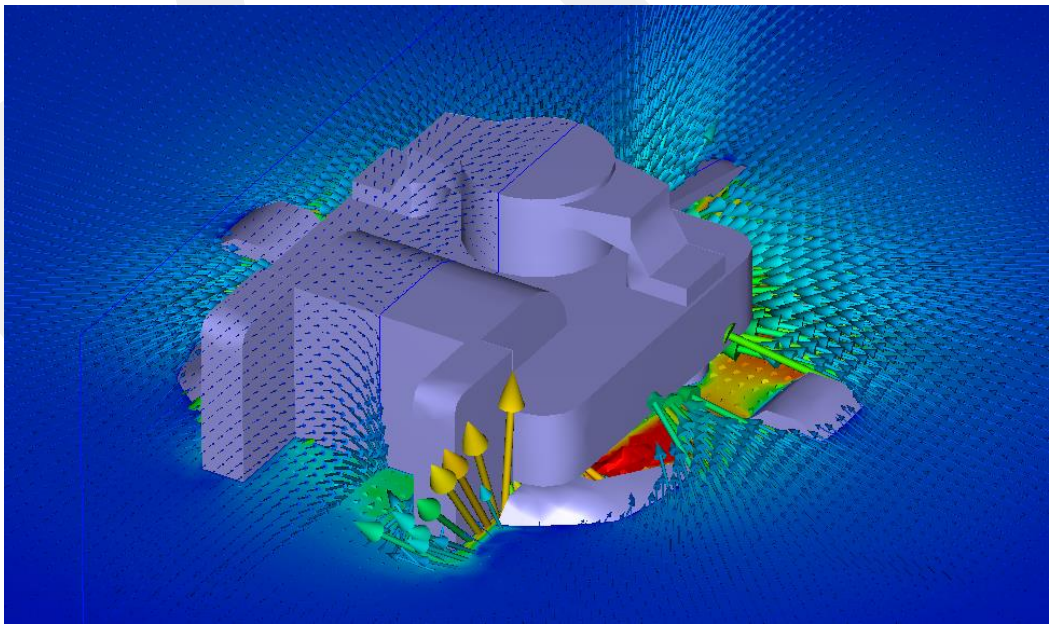

Figure 4.37 The flow lines around the first design impeller inlet area

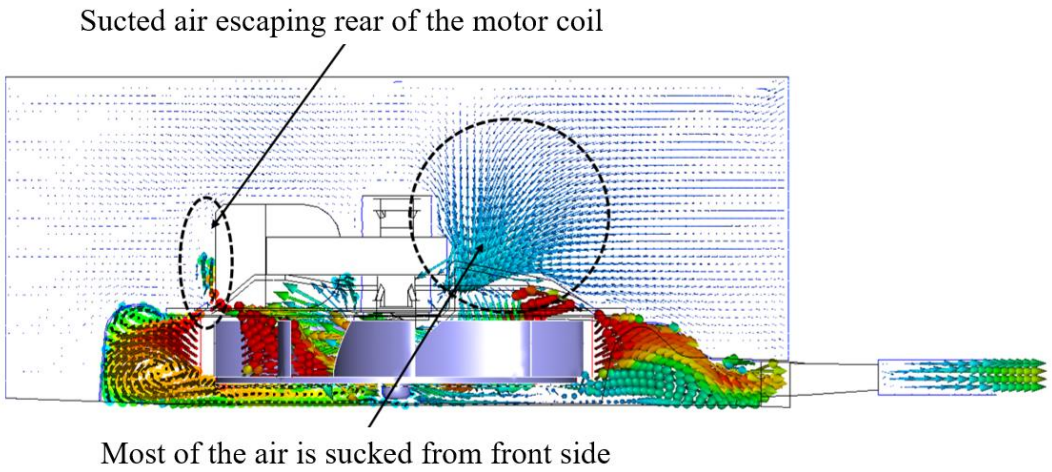

Figure 4.38 The side view of the flow lines around cooling group.

4.4.2 Description of the Second Motor Connection Part Design

4.4.2.1 Second Motor Connection Design CFD Simulation

Second designed motor connection part designed with an experience that is from the first designed motor connection part can be seen in Figure 4.39. To prevent air leakages and to increase volumetric flow rate cross section of the motor connection part design has been changed as seen in Figure 4.40.

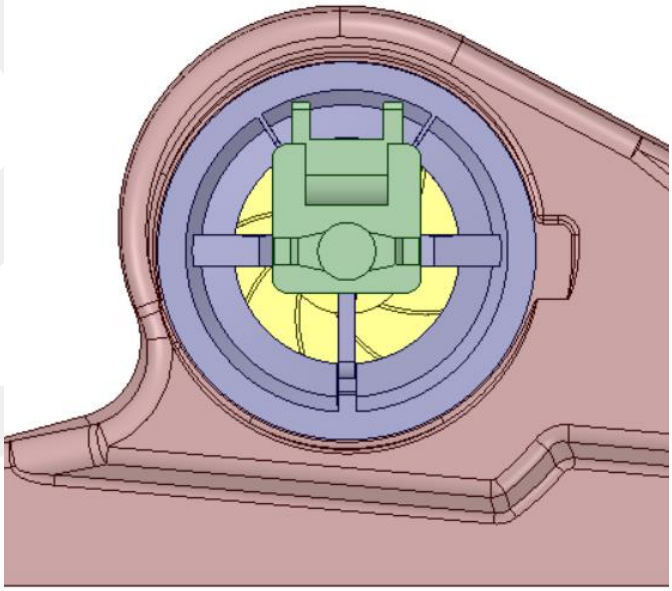

Figure 4.39 The second type of motor connection part.

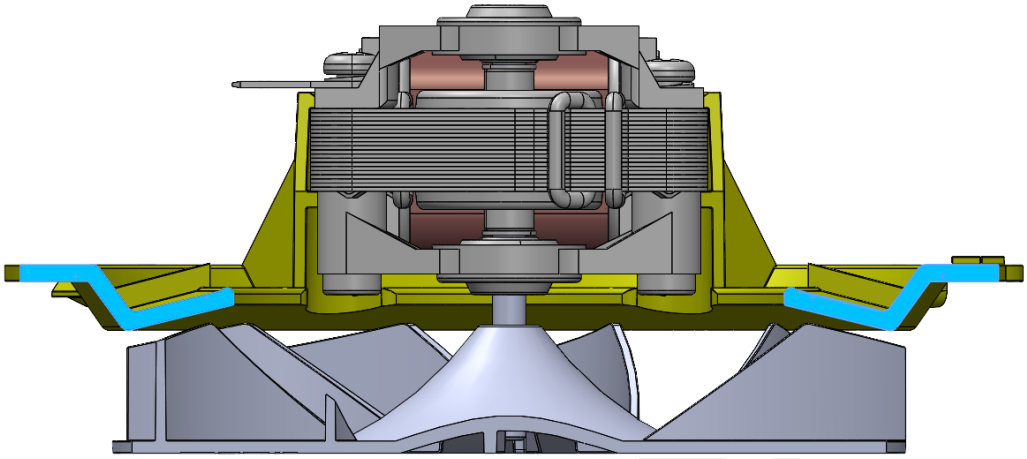

Figure 4.40 The cross section of second type of motor connection part

4.4.1.2 The Second Motor Connection Design CFD Result

CFD simulations showed that the cross section of the second designed motor connection part is more suitable than the first design. As seen in Figure 4.41 horizontal airflow enters easily to the inlet area. The geometry of the second designed motor connection part causes low-pressure territories and bends the horizontal airflow to the inlet area as seen in Figure 4.42. In addition, the second motor connection part did not have any leakage.

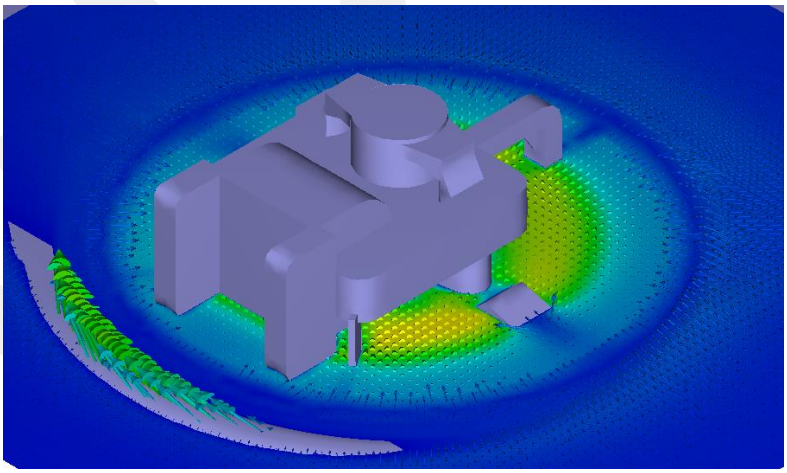

Figure 4.41 The flow lines around the second design impeller inlet area

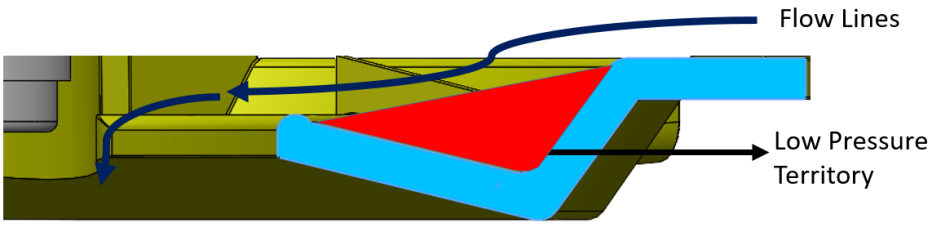

Figure 4.42 Illustration of horizontal air flow bending to the inlet area

4.5. Chimney Location

During the baking process, steam, and other gases are generated in the cooking chamber. Evaporated water can be beneficial for cooking, but harmful gases are carcinogenic and must be removed from the cooking chamber.

Therefore, the cooling group must suck an amount of air from the cooking cavity. The sucked air flow rate should be kept under control because of energy efficiency. Since the sucked air is at a high temperature, it can cool the inside of the cooking cavity and it can decrease the energy efficiency. For this reason, to determine the location of the suction region, the static pressure map has been used. The static pressure map under the impeller can be seen in Figure 4.43.

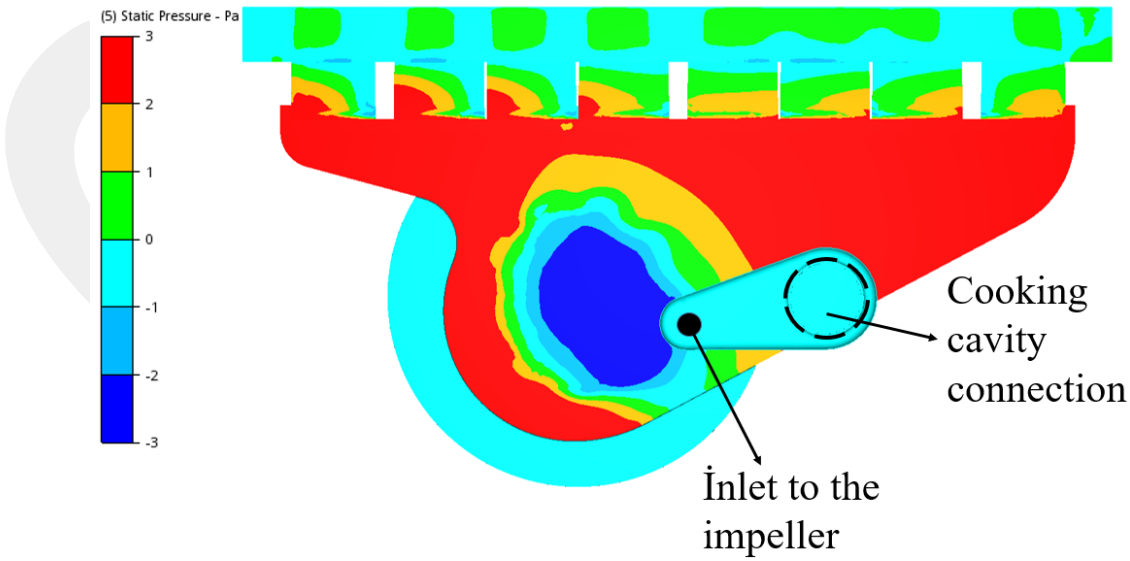

Figure 4.43 The static pressure map under the impeller

CHAPTER 5

VALIDATIONS

Simulation models are approximate imitations of real-world systems, and they never fully imitate the real-world system. Therefore, a physical model (prototype) must be verified and validated to the degree required for the intended purpose or application of the model. The validation checks the accuracy of the model's actual system representation. Model validation is defined to mean “proof that a computerized model in the field of feasibility has a satisfactory range of accuracy consistent with the intended application of the model. A model for a specific goal or set of goals should be established and its validity be determined for this purpose” [31][32].

5.1. Air Flow Validation

To validate the CFD simulations, the model has been created by the 3D MJF method by PA12 Polyamide. In practice, the steps that begin with the melting of PA12 powder from the reservoir with additives in 30 million droplets per second and the fusion of the layer continue with the additives catching the temperature. This cycle is repeated until the model appears. The motor connection part and impeller have been produced like a single part as seen in Figure 5.1. The sheet metal cover produced by real molds can be seen in Figure 5.2.

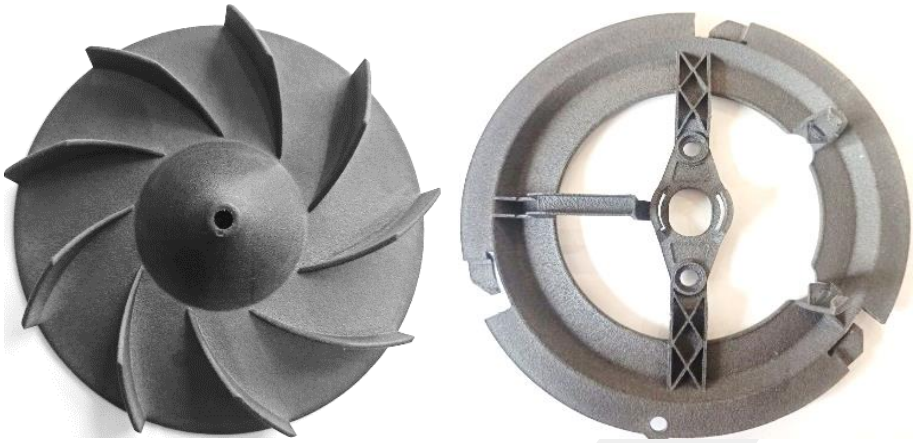

Figure 5.1 The impeller and motor connection PA12 prototype

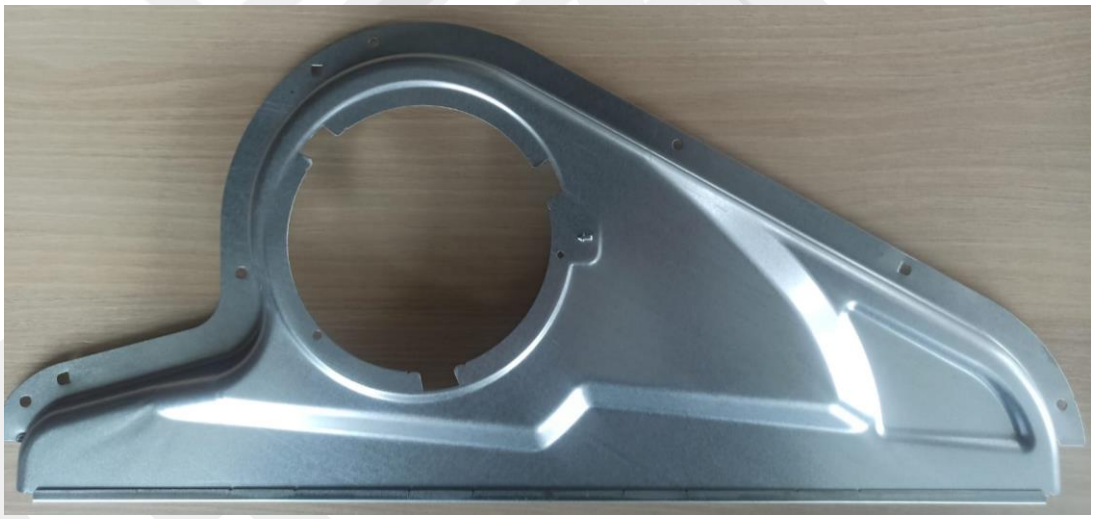

Figure 5.2 The sheet metal cover which produced by physical dies

The sheet metal part which is the bottom of the cooling group has been cut by computer-aided laser cutter. In this way, the hole position has been precisely placed as seen in Figure 5.3. As a result, the prototype of the cooling group was completed to test and validate as seen in Figure 5.4.

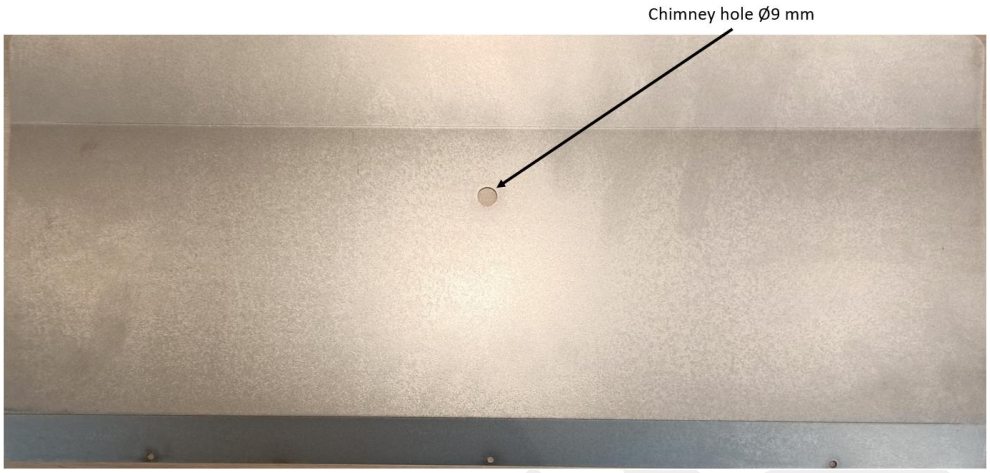

Figure 5.3 The cooling group bottom flat sheet metal cut by computer aided laser

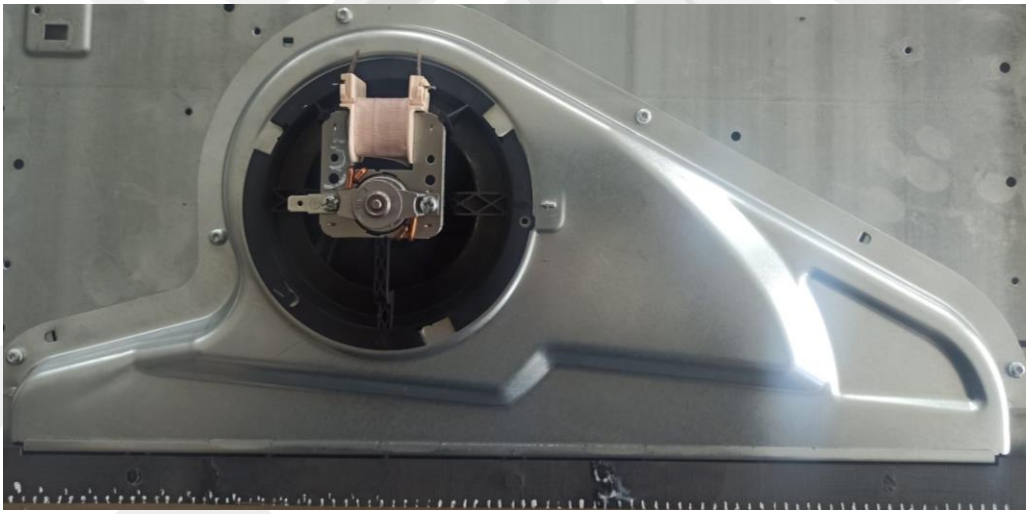

Figure 5.4 The completed third designed prototype

5.1.1. Flow Speed Validation by Calibrated Anemometer

The Hot Wire Anemometer is a device used to measure the velocity and direction of the fluid. This can be done by measuring the heat loss of the wire that is placed in the fluid stream. The wire is heated by an electrical current. When the hot wire placed in the fluid stream then the heat is transferred from the wire to the fluid, and hence the temperature of the wire decreases. The resistance of wire measures the velocity of the fluid.

In this study, calibrated Testo 405i hot wire anemometer was used to measure velocity deviation at the outlet of the cooling system. The device that used to measure can be seen in Figure 5.5. The measuring range of this device is between 0-30 m/s and the sensitivity is 0.03 m/s. Although there is high sensitivity, the anemometer direction and depth conditions can cause errors. In order to show these error, error bars added on the Figure 5.11. The operational temperature range is -20˚C to 60˚C.

Figure 5.5 Testo 405i hot wire anemometer

5.2. Sheet Metal Forming Simulation Validation

To validate sheet metal forming simulation, the dies were produced and a deep drawing process is done. To validate the simulation, Gom-Argus digital image correlation system was used at the Metal Forming Center of Excellence.

5.2.1 GOM-ARGUS Optical Forming Analysis

ARGUS measures and shows the quality and degree of the stamping process on sheet metal. For the calculation, the sheet metal is marked with a regular grid of dots, using chemical etching, laser marking or other marking techniques before forming. After stamp operation for the measurement, scale bars and some coded markers are located directly on the part or near around as it can be seen in Figure 5.6. Later, a digital CCD camera is used, with real time viewing of the actual view on the computer, to take shots from different locations.

Figure 5.6 The sheet metal cover which is located on scale bars and some coded markers

Then the addition of the images, ARGUS will detach in every image the exact center point of marked dots. Then, using photogrammetry methods, the images are imaginally assembled to produce the object as can be seen in Figure 5.7. From this imaginal assembly, the center of each dot on the part is defined in actual 3D coordinates. These calculated 3D points describe the actual form of the stamped part.

From the local distortion of the regular grids that was applied on the sheet metal before forming, the local strain introduced by the forming process is calculated in thousands of local data points. These strains which usually are the major and minor strains as well as the thickness changes define the degree of the forming. The strain values are mostly graphically displayed and validated in relation to the Forming Limit Diagram of the selected material or in relation to the maximum allowed reduction of the sheet thickness by the forming process. The certainty of the calculated strain values is better than +/- 0.5%, while displaying a good optical quality of the dots after the forming process.

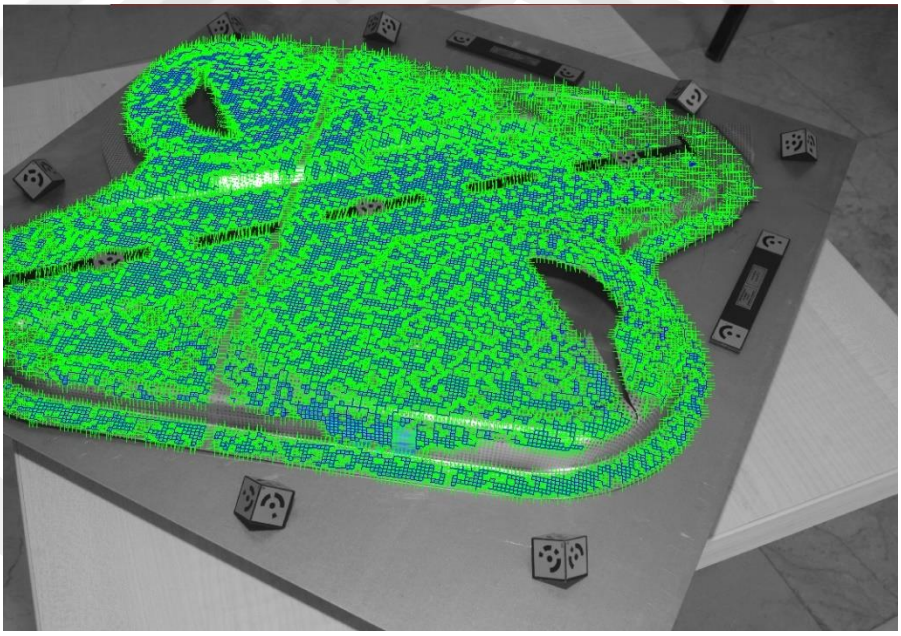

Figure 5.7 Using photogrammetry methods, the images are imaginally assembled to produce the object

One of the other advantages of optical correlation techniques is the correction of simulations which are performed before forming processes. Difference between the optical correlations and simulations gives error coefficients. Also, optical correlations are important for reverse engineering. With this technique, a forming process that has not been simulated before forming and failed can be repaired by ARGUS displayed strain and thickness reduction values with minor die changes.

As it is seen in Figure 5.8, during the deep drawing process , corners' grids have been erased because of friction between die and blank. For this reason, camera didn't realize these grids and didn't calculate strains at these regions.

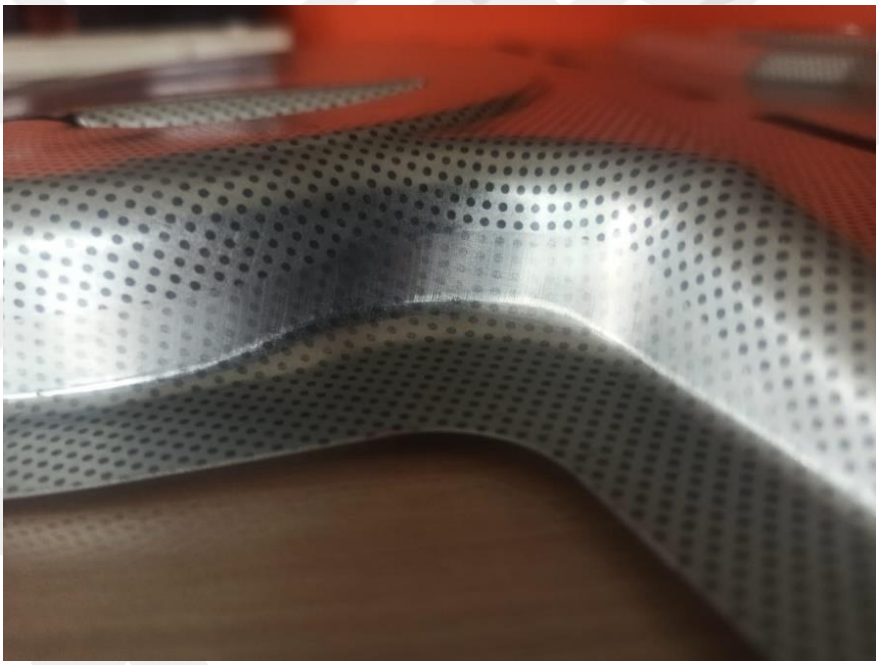

Figure 5.8 Erased corner grids because of die friction

5.3. Validation of Simulations

5.3.1. CFD Simulation Validation

Measurements made with a calibrated anemometer were compared with simulation results. To obtain consistent results, measurements were performed on 28 different holes at the same section (Figure 5.9), which are in the fluid domain. Holes were added on sheet metal impeller cover (Figure 5.10) to immerse the anemometer probe. Other holes were covered by aluminum tape during velocity measuring. The probe of the anemometer has been immersed parallel to flow lines according to the simulation results. In this way, the probe of the anemometer has faced directly the flow velocity and measurement precision has increased.

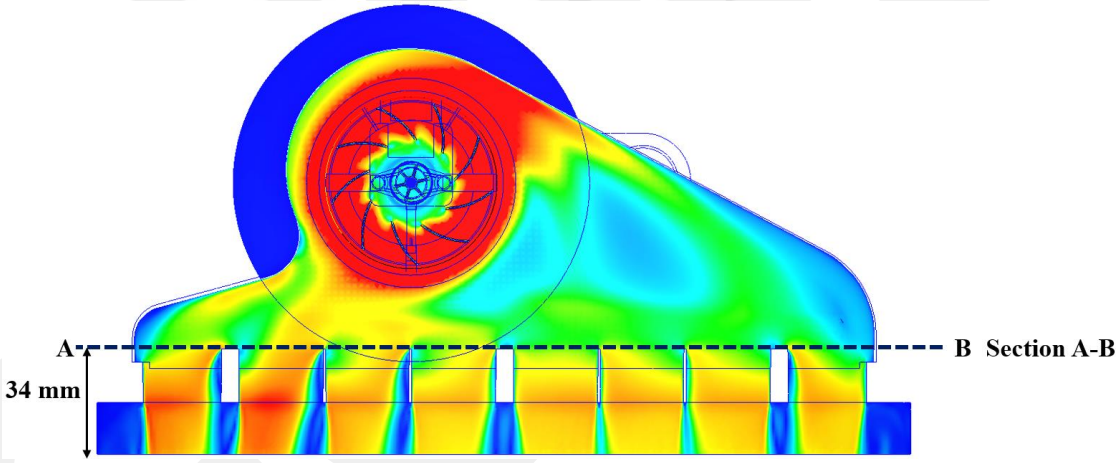

Figure 5.9 The section location of the holes where the measurements were made

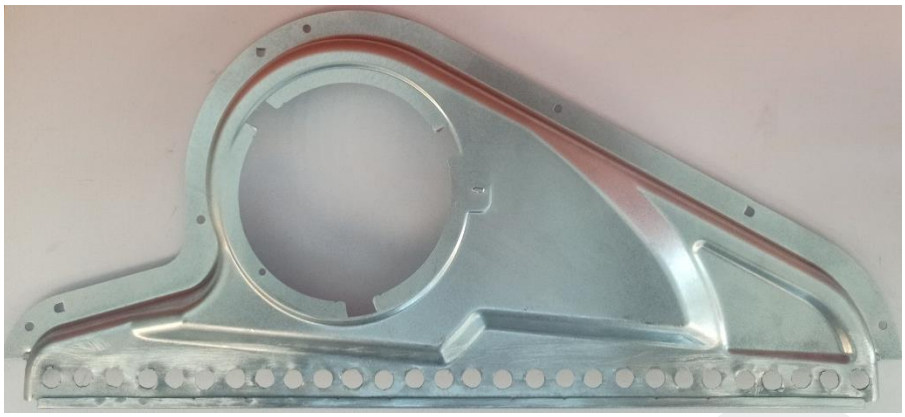

Figure 5.10 Holes on the sheet metal impeller cover to immerse the anemometer probe.

As seen in Figure 5.11 distribution and orientation between measured and simulated flow velocity has average 9.06% error. Maximum error was 22.9% at 22nd probe location and the minimum error was 0.7% at 11th probe location. The percentage errors of all 28 probe locations are given in Figure 5.11. The percentage errors were computed using: 100 x (Measured-Simulated)/Measured. Dimensional differences of the produced prototypes by PA 12 with 3D MJF method may have caused these differences in the results.

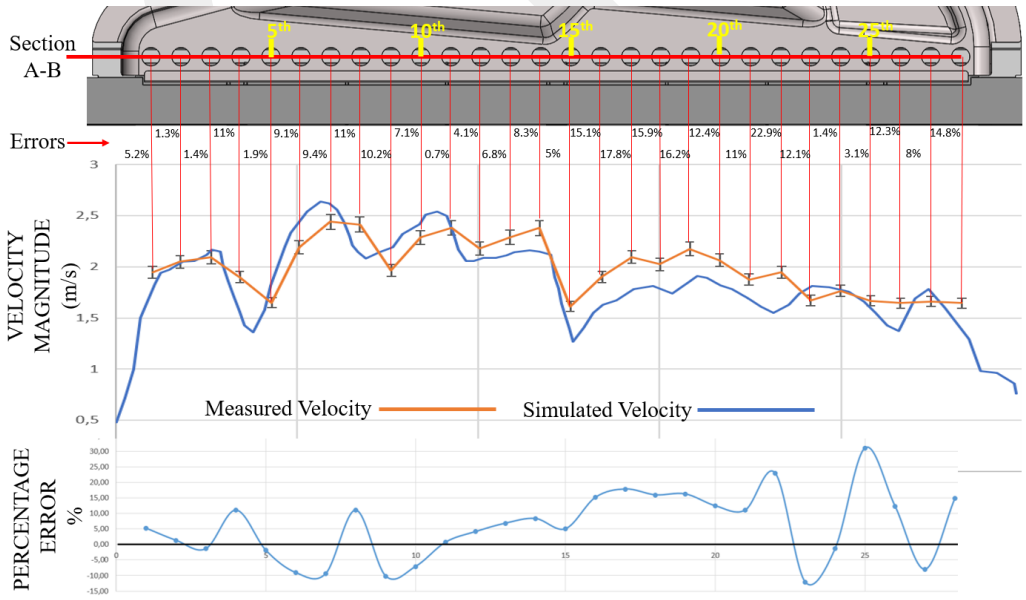

Figure 5.11. Measured and simulated flow velocity comparison of Section A-B and percentages errors

5.3.2 Forming Simulation Validation

After foreseeing the formability of sheet metal cover on Simufact Forming software, AutoForm software which licenced by external company (Halil TUTU) has been used to design efficient and precise die. Sheet metal's FLC and tensile test results defined in the Autoform Forming Software.

Although the part include erased grids because of die friction (Figure 5.8) and Gom-Argus' CCD camera didn't realize these grids that located critical corners, separation of plastic strains are close. These separation can be seen in Figure 5.12.

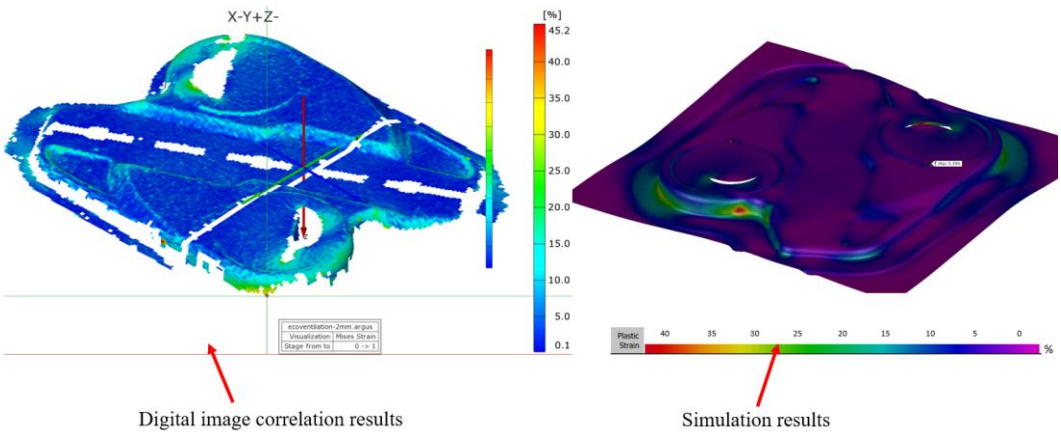

Figure 5.12 The comparison between Gom-Argus digital image correlation system and simulation Plastic Strain results

The thickness reduction change can be seen in Figure 5.13. Argus' CCD camera didn't realize erased grids so that critical corners didn't visualize which have high rate of thickness reduction. Neverthless, distribution of thickness reduction are very close.

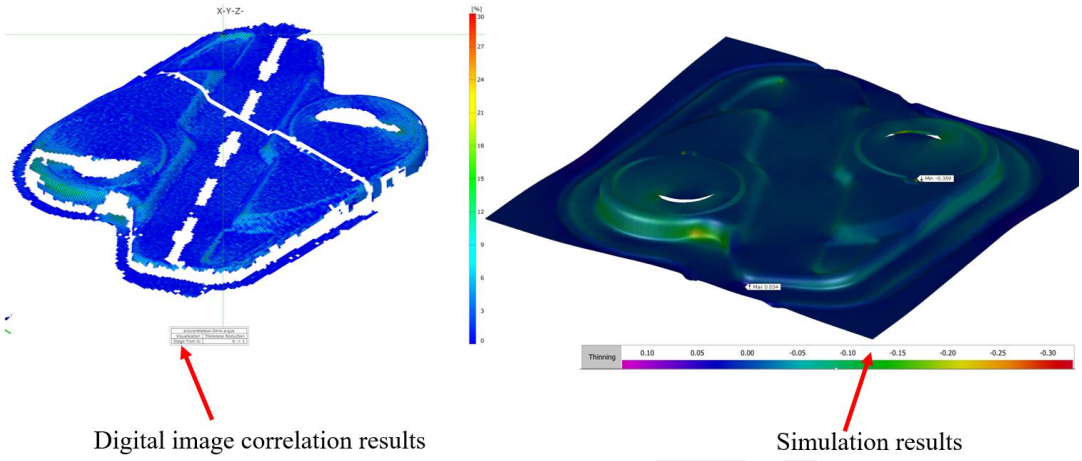

Figure 5.13 The comparison between Gom-Argus digital image correlation system and simulation thickness reduction results

The formability limit diagrams (FLD) of simulation and Gom-Argus results can be seen in Figure 5.14. Sheet metal's FLC test results (Table 3.3) defined in the Gom-Argus software. So that, we can compare the FLD results. The corners of the sheet metal part have more deformation than other flat surfaces. Unfortunately, corners' grids were erased because of the die friction and Argus' CCD camera didn't realize these grids. For this reason, there is a difference between simulated and measured formability limit diagrams. As seen from measured FLD results, there is no excess thinning region.

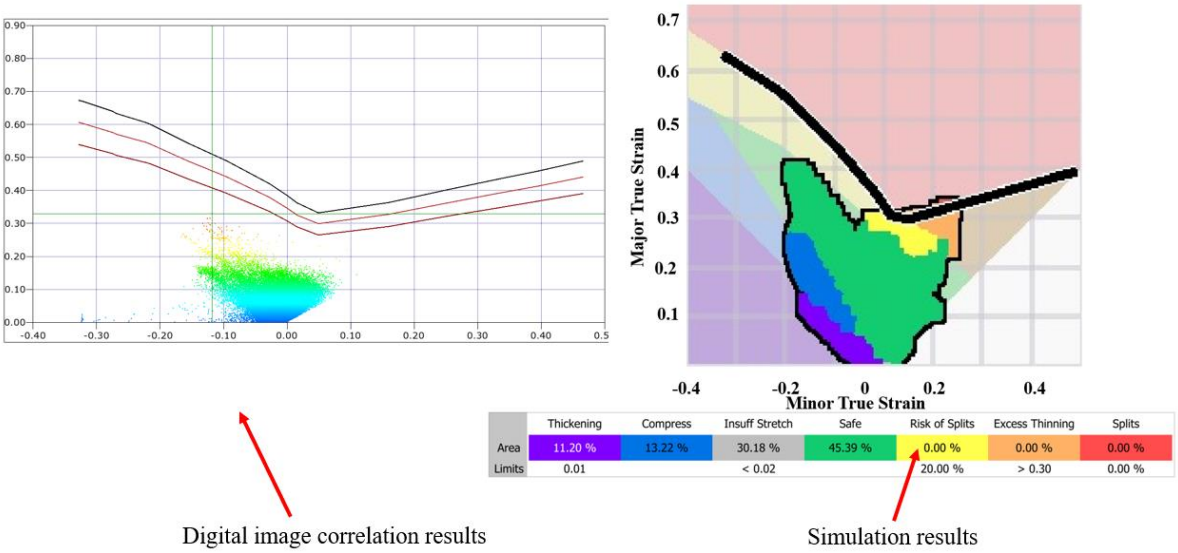

Figure 5.14 The comparison between Gom-Argus digital image correlation system and simulation FLD results

CHAPTER 6

RESULTS AND DISCUSSIONS

6.1 Results Obtained From Sheet Metal Forming Simulation

To find the best geometry of sheet metal cover of the cooling group for airflow parameters, forming simulations have been performed. After unsuccessful attempts, some parameters have been changed and retried. The parameters and differences which changed are critical radiuses and added hole. Simulation results show as seen in Table 6.1, only radius changes can make big difference. Radius difference from 16 mm to 28 mm helps 23.2% to forming. The critical zones can be seen in Figure 6.1.

Table 6.1 The radius changing effect on forming

Types of blank design	Press Stoke (mm)	Forming%
Corner radius 16 mm Second Designed Cooling Group	15.2	64
Corner radius 28 mm Third Designed Cooling Group	20.5	87.2

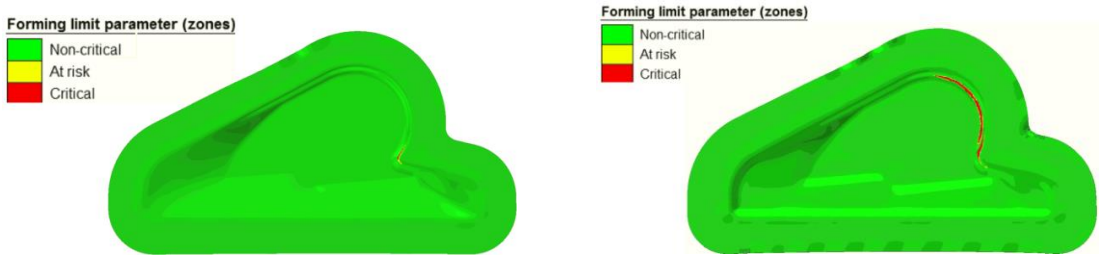

(a) (b)

Figure 6.1 The forming limit parameters of 16 mm corner radius cooling group sheet metal cover (a) and 28 mm radius cooling group sheet metal cover (b)

Despite all these improvements, tearing was still observed in the simulation results. To prevent tears while forming sheet metal cover, a hole was added. The hole location specially selected. The second step of forming is hole drilling for the motor connection part and the first hole's deformed shape will be a waste of sheet metal. Simulation results show as seen in Table 6.2, that radius changes and the added hole are enough not to forming of second designed cooling group sheet metal cover. But the third designed cooling group sheet metal cover is ready to forming with an expanded radius from 16 mm to 28 mm and 70 mm diameter hole. The differences in forming can be seen in Figure 6.2.

Table 6.2 The radius and hole effect on forming

Types of blank design	Press Stoke (mm)	Forming%
Corner radius 16 mm Second Designed Cooling Group With Ø 70 mm	16.5	70.2
Corner radius 28 mm Third Designed Cooling Group With Ø 70 mm	23.5	100

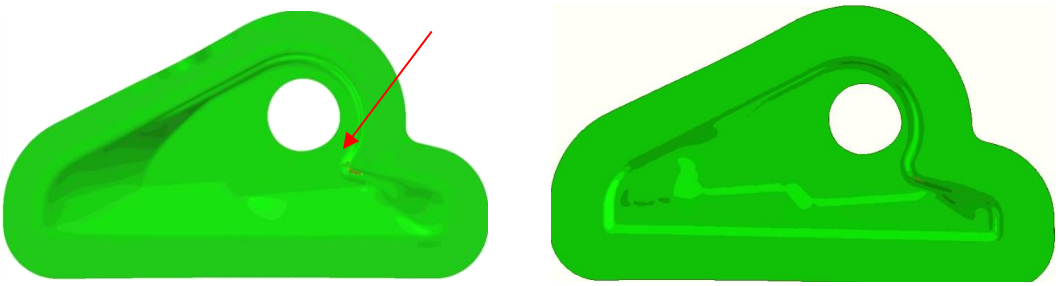

(a) (b)

Figure 6.2 The forming limit parameters of 16 mm corner radius cooling group sheet metal cover with 70 mm hole (a) and 28 mm corner radius cooling group sheet metal cover with 70 mm hole (b)

The hole was positioned close to critical forming areas and its diameter was adjusted so that it did not affect the cutting for the motor connection part. As seen in Figure 6.3 enlarged hole is very close to the motor connection cut-out but does not affect the cutting operations. As a result, the critical stage of forming which is the deep drawing has been successfully completed with radius change and added hole.

Figure 6.3 The location of the enlarged hole and motor connection cut out locations

6.2 Results Obtained From Computational Fluid Dynamics Simulations

CFD simulations performed to find better shape and geometry of sheet metal cover of the cooling group. Simulations show that the first designed sheet metal cover has a good homogeneity at the outlet region but the volumetric flow rate did not enough to cooling the built-in oven.

The reason for the low volumetric flow rate at the first designed cooling group is the geometry of the sheet metal cover. It has been determined that the air from the fan is sucked back because of the geometry design of the sheet metal cover. The geometry of the sheet metal cover did not prevent reverse flow. In this reason volumetric flow decreases. The undesirable air behaviors can be seen in Figure 6.4.

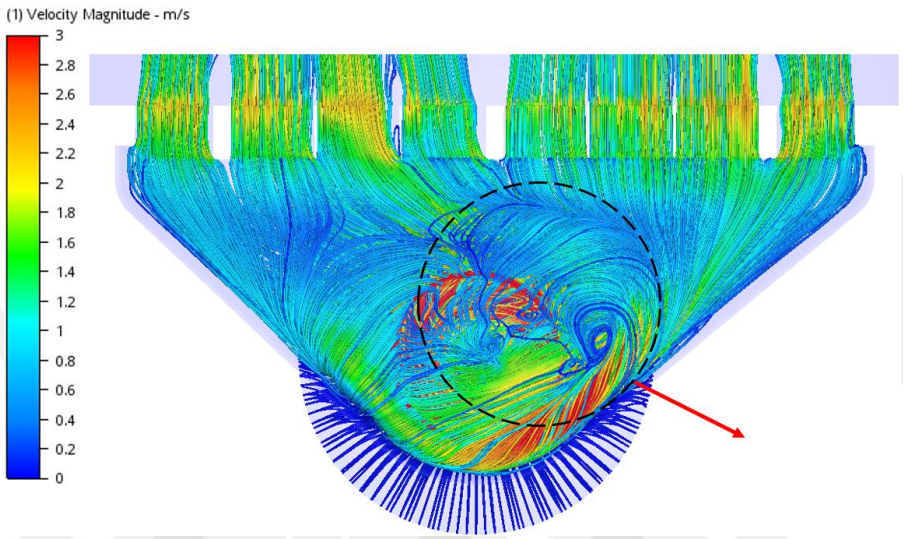

Figure 6.4 The bottom view of the first designed cooling group CFD results

To increase the volumetric flow rate, the design changed to prevent air from the fan is sucked back. To provide an increase volumetric flow rate, the sheet metal cover is revised like a well-known casing which is snail-shaped. Then CFD simulations were performed again and it was observed that the volumetric flow rate increased because of revised sheet metal cover geometry as it seems in Figure 6.5. The geometry change increased the volumetric flow rate from 232.5 L/min to 305.5 L/min which is a 31.4% improvement.

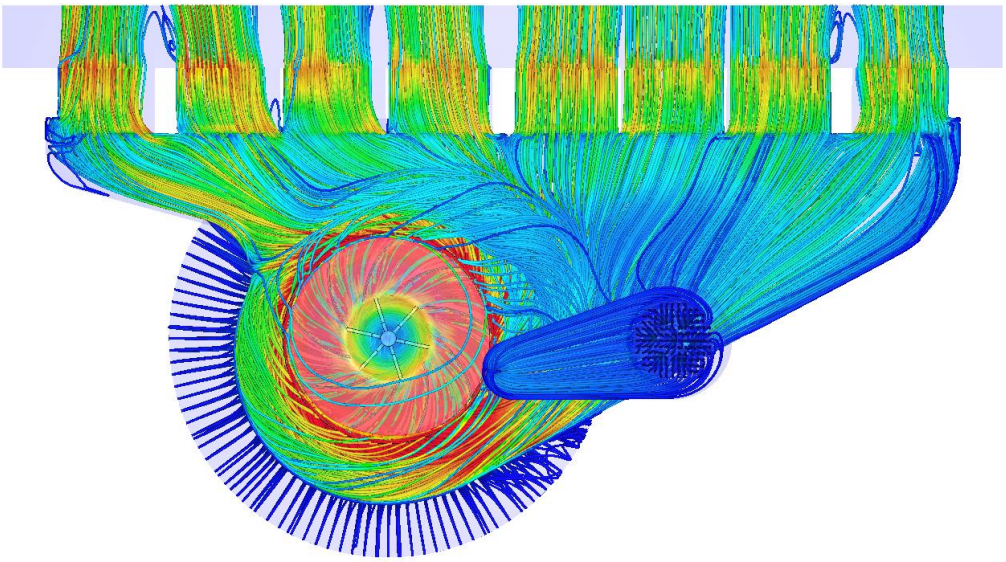

Figure 6.5 The bottom view of the third designed cooling group CFD results

As a result of all changes made by adhering to the design limits, a higher volumetric flow rate and homogeneous air outlet cooling group was designed. Results have been validated and verified.

REFERENCES

[1] M. Bellis, ‘’History of the Oven from Cast Iron to Electric.’’ Internet: https://www.thoughtco.com/history-of-the-oven-from-cast-iron-to-electric-1992212, Apr. 6, 2018 [Aug. 05, 2021]

[2] W. Hadaway, “Electric Heater.’’ U.S. Patent 705668A, June 30, 1900.

[3] Z. Marciniak, J. Duncan, J. Hu, *Mechanics of sheet metal forming*. Woburn, MA: Elsevier, 2002, pp.16, 35,75.

[4] DIN 8586, “Manufacturing processes forming by bending – Classification, subdivision, terms and definitions”, Internet: https://standards.globalspec.com/std/195639/DIN%208586 [02.05.2021].

[5] DIN 8584, “Manufacturing processes forming under combination of tensile and compressive conditions”, Internet: https://infostore.saiglobal.com/en-us/Standards/DIN-8584-1-2003-446074_SAIG_DIN_DIN_1006232/ , [02.04.2021].

[6] D. Banabic, M. Sester, *Sheet metal forming processes: constitutive modelling and numerical simulation*. Heidelberg, BE: Springer, 2012, pp. 304-308.

[7] Gestion de Compras Inc., “Progressive die stamping’’, https://www.gestiondecompras.com/zh/products/sheet-metal/progressive-die-stamping, [May, 5, 2021].

[8] M. A. Dib, N. J. Oliveira, A. E. Marques, M. C. Oliveira, J. V. Fernandes, B. M. Ribeiro, P. A. Prates, “Single and ensemble classifiers for defect prediction in sheet metal forming under variability”, *Neural Computing and Applications*, vol 32, pp. 1-15, Jan. 2019.

[9] W. F. Hosford, R. M. Caddell, *Metal forming mechanics and metallurgy*. USA: Cambridge University Press, 2007, pp.59-66.

[10] C. P. Nikhare, ‘’Experimental and numerical investigation of forming limit differences in biaxial and dome test’’, *Journal of Manufacturing Science and Engineering*, vol. 140, pp. 6-10, Aug. 2018.

[11] Tuzson, J. (2000). *Centrifugal pump design*. Evanston, Illinois: John Wiley & Sons,2000. pp. 133-153.

[12] Y. A. Cengel, J. M. Cimbala, "Chapter 14: Turbomachinery'' in *Fluid Mechanics Fundamental and Applications*. Mc Graw Hill Education, 2014, pp. 806-808.

[13] S. M. Yahya, *Turbines Compressors and Fans (3rd ed.)*. Tata McGraw-Hill Education, 2005, pp. 9-22.

[14] H. P. Bloch, P. E. Claire Soares, *Process plant machinery (2nd ed.)*. Boston: Butterworth-Heinemann, 1998, pp. 524.

[15] "Centrifugal Fans" ebm-papst. Internet: https://www.ebmpapst.com/de/en/products/centrifugal-fans.html [Mar. 02, 2021]

[16] AAON, "Value in the Air: Why Direct Drive Backward Curved Plenum Fans", Internet: https://www.aaon.com/Documents/Technical/ValueInTheAir_110106.pdf, Jan. 16, 2009 [Jan. 12,2021]

[17] R. R. Singh & M. Nataraj, "Design and analysis of pump impeller using SWFS." *World Journal of Modelling and Simulation*, 2014, pp. 152-160.

[18] O. *Reynolds, On the Dynamical Theory of Incompressible Viscous Fluids and the Determination of the Criterion.* The Royal Society of London A.,1895*, vol. 186, pp. 123–164.*

[19] P. Wesseling, *Principles of Computational Fluid Dynamics*. Springer-Verlag, Berlin: Heidelberg, 2001, pp. 531-559.

[20] H. Tennekes; J. L. Lumley, *A first course in turbulence*. Cambridge, Mass: MIT Press, 1992, pp.75,95.

[21] P. Bradshaw, "Turbulent Secondary Flows*". Annual Review of Fluid Mechanics*, vol. 19, pp: 53-74, 1975.

[22] D. C. Wilcox, *Turbulence Modeling for CFD*. Anaheim: DCW Industries, 1998, pp. 174.

[23] B. E. *Launder, D. B. Spalding*, "The numerical computation of turbulent flows". *Computer Methods in Applied Mechanics and Engineering*, 1974, pp. 269–289.

[24] H. K. Versteeg, W. Malalasekera, *An Introduction to Computational Fluid Dynamics: The Finite Volume Method*. London, UK: Pearson, 2007, pp.250-262.

[25] Autodesk CFD, "Support and Learning", Internet: https://knowledge.autodesk.com/support/cfd, Dec. 1, 2020 [Feb.23, 2021]

[26] J. R. Davis, *Tensile testing*. Ohio, U.S: ASM International, 2004, pp. 2.

[27] "BSI Standart Publication / Metallic Materials-Tensile testing / Part 1: Method of test at room temperature''. British, ISO 6892-1:2016, Internet: https://www.iso.org/obp/ui/#iso:std:iso:6892:-1:ed-3:v1:en, Jan. 23.2019, [May,13.2021].

[28] ISO 6892-1, "Metallic Materials-Tensile Testing-Part 1: Method of test at room temperature, Internet: https://www.iso.org/obp/ui/#iso:std:iso:6892:-1:ed-3:v1:en [Jan. 06, 2021].

[29] D. Banabic, H.J. Bunge, K. Pöhlandt, A.E. Tekkaya, *Formability of Metallic Materials*. Heidelberg, Berlin: Springer, 2001, pp. 200-204.

[30] R. Pearce, *Sheet Metal Forming*. New York, NY: IOP Publishing Ltd, New York, 1991, pp. 23.

[31] R. G. Sargent, "Verification and Validation of Simulation Models". *Proceedings of the 2011 Winter Simulation Conference*, 2011, pp.166-183.

[32] E. Yücesan, C. H. Chen, J. L. Snowdon, and J. M. Charnes. ''Model Verification and Validation,'' in *Proceedings of the 2002 Winter Simulation Conference*, 2002, pp.52-58.